

AN ABSTRACT OF THE DISSERTATION OF

Wei Wang for the degree of Doctor of Philosophy in Chemistry presented on August 23, 2013.

Title: Synthesis and Characterization of Aluminum Oxide Based Materials - from Molecule to Device

Abstract approved:

Douglas A. Keszler

A scalable synthesis of the “flat” tridecameric inorganic cluster $[Al_{13}(\mu_3-OH)_6(\mu_2-OH)_{18}(H_2O)_{24}]^{15+}$ has been realized by treating an aqueous aluminum nitrate solution with zinc-metal powder at room temperature. Single crystals and polycrystalline samples are readily obtained in yields exceeding 55% relative to the starting reagent $Al(NO_3)_3$. Products have been characterized by X-ray diffraction and solid-state ^{27}Al MAS and MQMAS NMR. Furthermore, we report a new integrated platform that combines: (i) an atom- & step-economical electrolytic synthesis of Al-containing nanoclusters in water with strict pH control; and (ii) an improved femtosecond stimulated Raman spectroscopic method covering a broad spectral range (350 to 1400 cm^{-1}), aided by ab-initio computations, to elucidate cluster structures and formation mechanisms of the clusters in real time. Using this platform, a new and unique view of *flat* $[Al_{13}(\mu_3-OH)_6(\mu_2-OH)_{18}(H_2O)_{24}](NO_3)_{15}$ cluster formation is observed, in which three distinct stages are identified. The first stage involves the formation of a hypothetical $[Al_7(\mu_3-OH)_6(\mu_2-OH)_6(H_2O)_{12}]^{9+}$ structure as an important intermediate towards the *flat* Al_{13} . Once the scalable synthesis has been developed, aqueous solution precursor made from “flat” Al_{13}

clusters are used for depositing high quality aluminum oxide thin films. Film structure, morphology, composition, and density at different annealing temperature are characterized by X-ray diffraction, AFM, SEM, TEM, FTIR, and X-ray Reflectivity. Optical properties of the films are investigated by spectroscopic ellipsometry. Simple metal-insulator-semiconductor capacitor test structure is used to evaluate the dielectric properties of the aluminum oxide thin films. After annealing at 500 °C, thin film exhibits low leakage current density ($< 10 \text{ nA}\cdot\text{cm}^{-2}$ at $1 \text{ MV}\cdot\text{cm}^{-1}$) and high breakdown field ($> 6 \text{ MV}\cdot\text{cm}^{-1}$). As a gate dielectric layer in thin film transistors with amorphous zinc tin oxide active channel, solution processed aluminum oxide layer exhibit dielectric properties similar to high quality SiO_2 gate dielectrics, i.e. low gate leakage current (nA level from -10 V to 30 V) and small clockwise hysteresis. Finally, thin film dielectric material $\text{Al}(\text{PO}_4)_{0.6}\text{O}_{0.6}\cdot x\text{H}_2\text{O}$, or “AlPO” is examined to explore a low-temperature dehydration alternative for the solution-deposited aluminum-oxide based films. As an amorphous oxide insulator, AlPO has been incorporated into thin-film transistors (TFT) via aqueous processing. It is found that the films must be heated above 600 °C to force dehydration and eliminate the mobile protons that cause unstable device operation. Here, we suggest that this dehydration temperature is largely dictated by rearrangements and densification near the surface of the film, as it is heated. A considerable quantity of water (and associated ions) becomes physically trapped in the bulk of the film. High temperatures are then required to promote diffusion and water loss across this surface “crust”. A hypothesis is that an appropriate very thin layer of a material having a lower dehydration temperature could be used to inhibit the densification and drying of AlPO in the near-surface region, thereby facilitating continuous water loss at relatively low temperature. Therefore, we choose solution-deposited HfO_2 films to alter the AlPO top surface. This material combination effectively decreases the dehydration temperature of AlPO (at about 250 °C), leading to dramatic changes in the dielectric behavior.

©Copyright by Wei Wang

August 23, 2013

All Rights Reserved

Synthesis and Characterization of Aluminum Oxide Based Materials
- from Molecule to Device

by
Wei Wang

A DISSERTATION

submitted to

Oregon State University

in partial fulfillment of
the requirements for the
degree of

Doctor of Philosophy

Presented August 23, 2013
Commencement June 2014

Doctor of Philosophy dissertation of Wei Wang

Presented on August 23, 2013.

APPROVED:

Major Professor, representing Chemistry

Chair of the Department of Chemistry

Dean of the Graduate School

I understand that my dissertation will become part of the permanent collection of Oregon State University libraries. My signature below authorizes release of my dissertation to any reader upon request.

Wei Wang, Author

ACKNOWLEDGEMENTS

First and foremost, I would like to thank my advisor, Prof. Keszler, for his support and guidance during the past five years. I refer his mentoring style as “libertarian paternalism” (a phrase I picked up from <Nudge>). I mean it in every good ways, because he gives me the most freedom to learn and explore things I am interested in while providing information and critical help at the right time to help me move forward and focus on the big picture. I am very grateful for having such a unique advisor.

I would like to also thank my committee members: Prof. Mike Lerner, Prof. MAS Subramanian, Prof. David Cann, and Prof. Roy Haggerty, for their time and effort. The classes I took during my first year from Prof. Lerner, Prof. Subramanian, and Prof. Cann gave me a boost start on my Ph.D program. The knowledge and life-time lessons I learned from them will benefit me for the rest of my life. As the GCR on my committee, Prof. Haggerty asked me to broaden my knowledge about the whole chemistry field rather than just focusing on my own project. I thank him for giving me this advice early in my program.

It has been an interesting and life changing five-year in the Keszler group and I would like to thank all the former and current group members for their generous help and continuous support. They are Dr. Jeremy Anderson, Dr. Kai Jiang, Dr. Stephen Meyers, Dr. Jason Stowers, Dr. Heather Platt, Dr. Chirs Knutson, Dr. Alan Telecky, Dr. Vorrnutch Jieratum (Nutch), Dr. Robert Kokenyesi, Dr. Rose Ruther, Dr. Michelle Dolgos, Ms. Sharon Betterton, Ms. Emmeline Alschul, Ms. Hidekel Ayeza Moreno Luna, Mr. Kris Olsen, Mr. Jae-Seok Heo, Ms. Deok-Hie Park, Mr. Shawn Decker, Ms. Jenn Amardar, and Mr. Vasily Gouliouk.

Among them, Stephen, Jeremy, and Kai gave me enormous amount of help when I first came to the group. Their Ph.D work provides the foundation of my dissertation.

Kai was also “the translator” between Prof. Keszler and me back in 2008. Chris and Alan are definitely who I interacted with the most in the Keszler group. Conversation among the three of us not only leads to new ideas and experiments but also helps me gain more understanding of the American culture. The friendship between us means a lot to me and I am hoping to develop it into a life time experience.

I would like to thank Dr. Robert Rung (“Skip”) and Ms. Cindy Dahl at Oregon Nanoscience and Microtechnologies Institute (ONAMI) for setting up the ONAMI graduate-intern scholarship, makes my ten-month internship with Amorphyx possible.

At Amorphyx, I had the most memorable and enjoyable “roller coaster ride” with my colleagues Bill Cowell, Sean Muir, and John Brewer. I spend most of my workdays with Bill and Sean and I’m constantly amazed by their abilities and enthusiasm on the road of startup. Of course there are up and downs in the process but we are able to go through these moments as a team. Moreover, they are both family guys and awesome dads. I admired them for their ability to balance work and family.

This dissertation would not be possible without the help from all of my collaborators. Most of them are associated with the Center for Sustainable Materials Chemistry, which is currently a phase II Center for Chemical Innovation funded by NSF (Grant number CHE-1102637). I would like to especially thank Dr. Shannon Boettcher for all the friendly and insightful discussions and Dr. I-Ya Chang for providing strong computational support in multiple projects. Also I would like to thank Dr. Bettye Maddux for provide lots of administration support in the center. Among the people who were not associated with the center, I would like to express my gratitude to Dr. Chong Fang and Dr. Weimin Liu in Department of Chemistry at Oregon State University, for lots of late night experiments..

A big part of the results in this dissertation are obtained in the lovely cleanroom in Owen hall and Mr. Chris Tasker and Mr. Rick Presley are the people made cleanroom lovely.

I would like to thank Ms. Margie Haak and Dr. Alan Richardson for their effort in preparing the general chemistry course materials as well as Ms. Kristi Edwards and Mr. Greg Jones for keeping the general chemistry lab well organized. Together they made the teaching assistants' job so much easier. And being a general chemistry TA played an important role in my processing of overcoming the language barrier.

My past few years would have been much less colorful without all of my friends here in Corvallis. Some of them are fellows came here the same year as me. Some of them are my former roommates, neighbors, and their friends. Some of them are my teammates on our sport teams. There are so many of them that I could not mention them one by one. However, I believe if you are one of them and you are reading this, you will know I am talking about you☺. Thank you, my friend!

Finally, I want to express my deepest thankfulness to my mom Xiaolan Pu, my dad Jianzhang Wang, my wife Lujing Li, and my son Ruihong Wang. I couldn't image how my life will be without them. The smile on their face is and will always be the ultimate reward for me.

CONTRIBUTION OF AUTHORS

D.A.K provides significant insights on the experimental design, result discussions, and manuscript writing and editing in all chapters. In chapter 2, all authors contributed to the manuscript writing and editing. K.M.W and S.E.H collected and interpreted the ^{27}Al solid-state NMR data. L.N.Z contributed to the single crystal X-ray diffraction. D.W.J. provided valuable suggestions during the project. In chapter 3, all authors contributed to the manuscript writing and editing. S.W.B. contributed in the development of the electrochemical methods for controlling pH. W-M.L. and C.F. developed the new FSR capabilities and made the associated Raman measurements. C.F. contributed in the analysis of the experimental Raman data. I-Y.C., L.A.W., and P.H-Y.C. performed the computations and peak assignment. L.N.Z contributed to the single crystal X-ray diffraction. In chapter 4, S.T.M contributed in experimental design and manuscript editing. R.E.P and J.F.W fabricated the ZTO thin-film transistor and helped with the data interpretation. In chapter 5, all authors contributed to the manuscript writing and editing. J.T.A and K.J. developed the original concept and did the initial demonstration. T.G., C.X, and E.L.G collected and analyzed the MEIS data.

TABLE OF CONTENTS

	<u>Page</u>
Introduction.....	1
References.....	12
Chapter 2: Synthesis of Hydroxide Cluster $[Al_{13}(\mu_3-OH)_6(\mu-OH)_{18}(H_2O)_{24}]^{15+}$ from Aqueous Solution.....	13
Main Text.....	14
References.....	20
Chapter 3: A New Portrait of Aluminum Speciation in Water.....	22
Introduction.....	23
Methods.....	24
Electrochemical Synthesis.....	24
Femtosecond Stimulated Raman Spectroscopy.....	25
Computations.....	26
Least-Squares Fitting Procedure.....	26
Results and Discussion.....	26
Conclusions.....	35
References.....	36
Chapter 4: Aqueous Solution Processed Aluminum Oxide Thin-film Dielectrics - Reaction Pathway Control from Precursor to Film.....	38
Introduction.....	39
Experimental Methods.....	41
Precursor Synthesis.....	42

TABLE OF CONTENTS (Continued)

	<u>Page</u>
Thin-Film Deposition	42
Chemical Characterization.....	42
Morphology and Density Characterization.....	43
Optical Characterization.....	43
Electrical Device Fabrication and Characterization	44
Results and Discussion.....	44
Summary and Perspective.....	59
Reference.....	60
Chapter 5: Chemically Enhanced Thermal Dehydration of Thin-film Oxides.....	64
Introductory Paragraph.....	65
Main Text.....	65
Methods.....	73
Solution Precursor Synthesis and Thin-film Deposition	73
Metal-insulator-metal (MIM) Capacitor Characterization	73
Thin-film Characterizations.....	74
References.....	75
Conclusion	78
Bibliography.....	82
Appendix A: Supporting Information for Chapter 3	87
Expanded Discussion of the Electrochemical Synthesis Method:.....	87
X-ray Diffraction Analysis of Single Crystals from Cathode Solutions	89

TABLE OF CONTENTS (Continued)

	<u>Page</u>
Newly Improved Femtosecond Stimulated Raman (FSR) Method.....	91
Expanded Discussion of FSR Data Collection and Analysis:.....	94
Computational Methods for FSR Raman Spectral Analysis.....	98
Effect of Water Coordination on Raman Spectra:	117
Full authorship of Gaussian 09.....	119
Reference.....	119
Appendix B.....	121
Reference	1263
Appendix C.....	124
Reference	126
Appendix D: Supporting Information for Chapter 5	127

LIST OF FIGURES

<u>Figure</u>	<u>Page</u>
Figure 1.1. A cross-sectional schematic of a simple bottom gate thin-film transistor.	3
Figure 1.2. Sketches of a flat highway (upper) and an up-and down highway (lower)	4
Figure 1.3. Two glass vials filled to the same level. One contains solid spheres and the other contains fine powder.	7
Figure 1.4. Structure of “flat” Al ₁₃ : (left) top view, (right) side view.	8
Figure 1.5. Cross section TEM images of an aluminum phosphate oxide film at (a) 0 minutes; (b) 30 minutes.	9
Figure 1.6. Coffee spill.	10
Figure 2.1. Structure of “flat” [Al ₁₃ (μ ₃ -OH) ₆ (μ-OH) ₁₈ (H ₂ O) ₂₄] ¹⁵⁺ cluster: (a) perpendicular to the central plane; (b) parallel to the central plane. Al – violet spheres; O – orange spheres; H – white spheres.	15
Figure 2.2. X-ray powder diffraction pattern of the polycrystalline sample and powder simulation pattern from single crystal structure of [Al ₁₃ (μ ₃ -OH) ₆ (μ- OH) ₁₈ (H ₂ O) ₂₄](NO ₃) ₁₅	16
Figure 2.3. ²⁷ Al MQMAS of [Al ₁₃ (μ ₃ -OH) ₆ (μ-OH) ₁₈ (H ₂ O) ₂₄](NO ₃) ₁₅	18
Figure 3.1. (Left) Cell for Al(NO ₃) ₃ (aq) electrolysis; (Top right) balanced electrode reactions under acidic conditions; (Bottom right) cathode solution pH vs. total charge passed through the system; the region of Al nanocluster formation is highlighted.	27
Figure 3.2. Differential FSR spectra of the cathode solution as pH increases from 1.90 to 3.18. The vertical double-headed arrow indicates a stimulated Raman gain of 0.04%. The FSR spectrum of the precursor solution (pH=1.9) is scaled by a factor of 0.05. The nascent vibrational peaks are marked by dashed lines.	30
Figure 3.3. Differential FSR spectra (pH = 3.18) with contributions from (a) each cluster and (b) each hydroxyl ligand, and LSFC Raman spectrum of (c) <i>flat</i> Al ₁₃ (orange), (d) Al ₇₊₁ (green), and (e) Al ₇ (violet).	31

LIST OF FIGURES (Continued)

<u>Figure</u>	<u>Page</u>
Figure 3.4. Differential FSR signal intensity vs. pH for 1.0-M Al(NO ₃) ₃ (aq) solution in reaction. Peak assignments for the Al clusters with reference to Figure 3.3 are 937 (μ ₃ -OH), 1151 (μ ₂ -OH _{core}), and 1275 cm ⁻¹ (μ ₂ , μ ₃ -OH _{shell}). The 525 cm ⁻¹ signal corresponds to Al-O vibrations in Al(H ₂ O) ₆ ³⁺ , and the signals at 718 and 1048 cm ⁻¹ are associated with NO ₃ ⁻	34
Figure 4.1. XRD pattern of aluminum oxide thin film annealed at selected temperatures.....	46
Figure 4.2. SAED of aluminum oxide thin films annealed at selected temperatures: (a) 300 °C, (b) 500 °C and (c) 800 °C.....	46
Figure 4.3. FTIR spectra of aluminum oxide films annealed at selected temperatures.....	47
Figure 4.4. Aluminum oxide thin films annealed at selected temperatures: SEM (a) non-annealed, (b) 500 °C, and (c) 800 °C; AFM (d) 500 °C and (e) 800 °C.....	48
Figure 4.5. (a) STEM and (b) HRTEM cross section images of an aluminum oxide thin film annealed at 500 °C.....	49
Figure 4.6. Refractive index vs. wavelength for solution deposited Al ₂ O ₃ films annealed at different temperatures.....	50
Figure 4.7. Experimental and modeled XRR spectra for a 20.4 nm film on p-Si, annealed at 500 °C.	51
Figure 4.8. Temperature dependence of density and surface roughness examined via XRR.....	51
Figure 4.9. XRR spectra of un-annealed aluminum oxide films made from precursors with different metal concentration.....	53
Figure 4.10. Thickness per spin coating cycle vs. precursor concentration, measured by X-ray reflectivity (XRR) and spectroscopic ellipsometry (SE). Red curve shows the parabolic fitting based on XRR data.	55
Figure 4.11. Representative current-voltage curves for films annealed at different temperatures.....	57

LIST OF FIGURES (Continued)

<u>Figure</u>	<u>Page</u>
Figure 4.12. I_D - V_{GS} ($V_{DS} = 1$ V) and I_G - V_{GS} curves for TFTs with a sputtered ZTO channel layer and (a) an Al_2O_3 gate dielectric and (b) a SiO_2 gate dielectric.....	59
Figure 5.1 (a) A typically C-V measurement setup for an MIM capacitor; (b) One sweep cycle of MIM capacitors with an AlPO insulator (black) and a HfO ₂ -AlPO insulator (orange). Both insulating oxide layers were annealed at 350 °C for one hour.	68
Figure 5.2 (a) High resolution TEM image of the HfO ₂ -AlPO interface region in HfO ₂ -AlPO stack after annealed at 350 °C for one hour; (b) Z-contrast STEM image showing the interface region; (c) ChemiSTEM Hf elemental mapping at the same position of image (b).	68
Figure 5.3 (a) Typical MEIS geometry (b) MEIS spectra of HfO ₂ thin film on silicon and HfO ₂ -AlPO stack on silicon substrate.....	70
Figure 5.4 (a) typically HFS geometry; (b) hydrogen atomic percentages in AlPO layer annealed at 350 °C and 600 °C for one hour without HfO ₂ (black), and annealed at 350 °C for one hour with HfO ₂ (orange).....	71
Figure A.1. ²⁷ Al solution NMR spectra of cathode solution (pH = 3.20) using 1.0 M Al(NO ₃) ₃ (aq.) solution as reference.	89
Figure A.2. Schematic of the newly improved non-resonant FSR spectroscopy. The output laser beam from a Coherent fs regenerative amplifier is split to generate two ultrafast laser pulses for ground state FSR spectra: Raman pump beam at 800 nm (~3.5 ps, 6 mW) and Raman probe beam with the wavelength range of 805–1000 nm (~30 fs, 100 nW). The Al electrolysis apparatus for precise pH control to study the aqueous Al cluster speciation is described in the text. BS: beamsplitter, G: reflective ruled diffraction grating (1200 grooves/mm, blazed at 750 nm), CL: cylindrical lens, UM: pick-up mirror, VNDF: variable neutral density filter, L: bi-convex lens (f = 10 or 5 cm), SA: sapphire plate, BBO: 0.1-mm-thick β-barium borate crystal (type I, θ=27.8°), LPF: long-wavelength pass filter, PR1: fused silica prism pair, P: polarizer, λ/2 WP: half-wavelength waveplate at 800 nm, and CFWM: cascaded four-wave-mixing spatially-separated self-compressed sideband signal used as the new Raman probe beam to stimulate the Stokes Raman signal collected in this experiment.....	92

LIST OF FIGURES (Continued)

<u>Figure</u>	<u>Page</u>
Figure A.3. An independently collected dataset is shown in red in comparison to the data from the main text (in black), exhibiting the same trend within experimental uncertainty in signal evolution discussed therein.	97
Figure A.4. The geometries of clusters whose LSFC Raman spectra were computed and used as reference for assignment of experimental spectra.	99
Figure A.5. The experimental differential FSR spectrum (pH = 3.18) and the LSFC Raman spectrum, composing 402 Raman vibrational modes, generated from the computed Raman vibrational frequencies and intensities of <i>flat</i> Al ₁₃ (192 vibrational modes), Al ₇₊₁ (114 vibrational modes) and Al ₇ (96 vibrational modes). In addition, the Raman contributions of each hydroxyl ligands in each polycation are also shown. The RMSD between the LSFC Raman and differential FSR spectrum (positive peaks) spectra are 4.5% for 350~1305 cm ⁻¹ and 2.8% for 907~1300 cm ⁻¹ . In the LSFC Raman spectrum, a universal scaling factor (0.9700) is used to modulate the frequencies of all the species and three intensity scaling factors are used for <i>flat</i> Al ₁₃ (0.066459), Al ₇₊₁ (0.022514) and Al ₇ (0.057475), respectively. The normalized factor for the experimental differential FSR spectrum is 0.000235.	105
Figure A.6. The experimental differential FSR spectrum (pH = 3.18) and the LSFC Raman spectrum, composing 288 Raman vibrational modes, generated from the computed Raman vibrational frequencies and intensities of <i>flat</i> Al ₁₃ (192 vibrational modes) and Al ₇ (96 vibrational modes). In addition, the Raman contributions of each hydroxyl ligands in each polycation are also shown. The RMSD between the LSFC Raman and differential FSR spectrum (positive peaks) spectra are 4.9% for 350~1305 cm ⁻¹ and 2.9% for 907~1300 cm ⁻¹ . In the LSFC Raman spectrum, a universal scaling factor (0.9700) is used to modulate the frequencies of all the species and two intensity scaling factors are used for <i>flat</i> Al ₁₃ (0.054674) and Al ₇ (0.081381), respectively. The normalized factor for the experimental differential FSR spectrum is 0.000235.	106

LIST OF FIGURES (Continued)

<u>Figure</u>	<u>Page</u>
Figure A.7. The experimental differential FSR spectrum (pH = 3.18) and the LSFC Raman spectrum, composing 306 Raman vibrational modes, generated from the computed Raman vibrational frequencies and intensities of <i>flat</i> Al ₁₃ (192 vibrational modes) and Al ₇₊₁ (114 vibrational modes). In addition, the Raman contributions of each hydroxyl ligands in each polycation are also shown. The RMSD between the LSFC Raman and differential FSR spectrum (positive peaks) spectra are 4.9% for 350~1305 cm ⁻¹ and 4.2% for 907~1300 cm ⁻¹ . In the LSFC Raman spectrum, a universal scaling factor (0.9702) is used to modulate the frequencies of all the species and two intensity scaling factors are used for <i>flat</i> Al ₁₃ (0.074789) and Al ₇₊₁ (0.072037), respectively. The normalized factor for the experimental differential FSR spectrum is 0.000235.....	107
Figure A.8. The experimental differential FSR spectrum (pH = 3.18) and the LSFC Raman spectrum, composing 210 Raman vibrational modes, generated from the computed Raman vibrational frequencies and intensities of Al ₇₊₁ (114 vibrational modes) and Al ₇ (96 vibrational modes). In addition, the Raman contributions of each hydroxyl ligands in the polycation are also shown. The RMSD between the LSFC Raman and differential FSR spectrum (positive peaks) spectra are 5.7% for 350~1305 cm ⁻¹ and 5.2% for 907~1300 cm ⁻¹ . In the LSFC Raman spectrum, a universal scaling factor (0.9719) is used to modulate the frequencies of all the species and two intensity scaling factors are used for Al ₇₊₁ (0.047637) and Al ₇ (0.128482), respectively. The normalized factor for the experimental differential FSR spectrum is 0.000235.....	108
Figure A.9. The experimental differential FSR spectrum (pH = 3.18) and the LSFC Raman spectrum generated from the computed Raman vibrational frequencies and intensities of <i>flat</i> Al ₁₃ (192 Raman vibrational modes). In addition, the Raman contributions of each hydroxyl ligands in the polycation are also shown. The RMSD between the LSFC Raman and differential FSR spectrum (positive peaks) spectra are 7.3% for 350~1305 cm ⁻¹ and 6.6% for 907~1300 cm ⁻¹ . In the LSFC Raman spectrum, two universal scaling factors are used to modulate the computed Raman frequencies (0.9555) and intensities (0.059155) of <i>flat</i> Al ₁₃ . The normalized factor for the experimental differential FSR spectrum is 0.000235.....	109

LIST OF FIGURES (Continued)

<u>Figure</u>	<u>Page</u>
Figure A.10. The experimental differential FSR spectrum (pH = 3.18) and the LSFC Raman spectrum generated from the computed Raman vibrational frequencies and intensities of Al_{7+1} (114 Raman vibrational modes). In addition, the Raman contributions of each hydroxyl ligands in the polycation are also shown. The RMSD between the LSFC Raman and differential FSR spectrum (positive peaks) spectra are 6.3% for 350~1305 cm^{-1} and 6.6% for 907~1300 cm^{-1} . In the LSFC Raman spectrum, two universal scaling factors are used to modulate the computed Raman frequencies (0.9783) and intensities (0.108066) of Al_{7+1} . The normalized factor for the experimental differential FSR spectrum is 0.000235. ..	110
Figure A.11. The experimental differential FSR spectrum (pH = 3.18) and the LSFC Raman spectrum generated from the computed Raman vibrational frequencies and intensities of Al_7 (96 Raman vibrational modes). In addition, the Raman contributions of each hydroxyl ligands in the polycation are also shown. The RMSD between the LSFC Raman and differential FSR spectrum (positive peaks) spectra are 7.9% for 350~1305 cm^{-1} and 6.2% for 907~1300 cm^{-1} . In the LSFC Raman spectrum, two universal scaling factors are used to modulate the computed Raman frequencies (0.9697) and intensities (0.137532) of Al_7 . The normalized factor for the experimental differential FSR spectrum is 0.000235. ..	111
Figure A.12. The experimental differential FSR spectrum (pH = 3.18) and the LSFC Raman spectrum generated from the computed Raman vibrational frequencies and intensities of Al_8 (67 Raman vibrational modes). In addition, the Raman contributions of each hydroxyl ligands in the polycation are also shown. The RMSD between the LSFC Raman and differential FSR spectrum (positive peaks) spectra are 6.8% for 350~1305 cm^{-1} and 7.1% for 907~1300 cm^{-1} . In the LSFC Raman spectrum, two universal scaling factors are used to modulate the computed Raman frequencies (0.9538) and intensities (0.095485) of Al_8 . The normalized factor for the experimental differential FSR spectrum is 0.000235. ..	112
Figure A.13. The experimental differential FSR spectrum (pH = 3.18) and the LSFC Raman spectrum generated from the computed Raman vibrational frequencies and intensities of Al_6^c (73 Raman vibrational modes). In addition, the Raman contributions of each hydroxyl ligands in the polycation are also shown. The RMSD between the LSFC Raman and differential FSR spectrum (positive peaks) spectra are 8.0% for 350~1305 cm^{-1} and 7.9% for 907~1300 cm^{-1} . In the LSFC Raman spectrum, two universal scaling factors are used to modulate the computed Raman frequencies (0.9809) and intensities (0.072053) of Al_6^c . The normalized factor for the experimental differential FSR spectrum is 0.000235. ..	113

LIST OF FIGURES (Continued)

<u>Figure</u>	<u>Page</u>
<p>Figure A.14. The experimental differential FSR spectrum (pH = 3.18) and the LSFC Raman spectrum generated from the computed Raman vibrational frequencies and intensities of Al₂ (17 Raman vibrational modes). The RMSD between the LSFC Raman and differential FSR spectrum (positive peaks) spectra are 9.7% for 350~1305 cm⁻¹ and 8.8% for 907~1300 cm⁻¹. In the LSFC Raman spectrum, two universal scaling factors are used to modulate the computed Raman frequencies (1.0347) and intensities (0.115939) of Al₂. The normalized factor for the experimental differential FSR spectrum is 0.000235.</p>	114
<p>Figure A.15. The experimental differential FSR spectrum (pH = 3.18) and the LSFC Raman spectrum generated from the computed Raman vibrational frequencies and intensities of Al₁ (9 Raman vibrational modes). The RMSD between the LSFC Raman and differential FSR spectrum (positive peaks) spectra are 14.4% for 350~1305 cm⁻¹ and 16.3% for 907~1300 cm⁻¹. In the LSFC Raman spectrum, two universal scaling factors are used to modulate the computed Raman frequencies (1.0325) and intensities (0.086834) of Al₁. The normalized factor for the experimental differential FSR spectrum is 0.000235.</p>	115
<p>Figure A.16. The experimental differential FSR spectrum (pH = 3.18) and the LSFC Raman spectrum generated from the computed Raman vibrational frequencies and intensities of Al₁ (9 Raman vibrational modes). The RMSD between the LSFC Raman and differential FSR spectrum (negative peaks) spectra are 18.9% for 350~1107 cm⁻¹ and 0.4% for 350~820 cm⁻¹. This figure together with Fig. S15 show that Al₁ is not an emerging species but a consuming species in the electrolysis process. In the LSFC Raman spectrum, two universal scaling factors are used to modulate the computed Raman frequencies (1.0539) and intensities (-0.009743) of Al₁. The normalized factor for the experimental differential FSR spectrum is 0.031701.</p>	116

LIST OF FIGURES (Continued)

<u>Figure</u>	<u>Page</u>
<p>Figure A.17. The FSR spectrum (pH = 1.90) with (a) the computed LSFC Raman spectra, (b) The zooming in of the light yellow region in (a), and (c) the raw computed Raman spectra. The frequency scaling factors for LSFC Raman Spectra of Al_1 & NO_3^- and $[\text{Al}_1 \cdot 12\text{H}_2\text{O}]^{3+}$ & NO_3^- are 1.055 and 1.0, respectively. The same frequency scaling factors are used for the computed Raman spectra of Al_1 (1.055) and $[\text{Al}_1 \cdot 12\text{H}_2\text{O}]^{3+}$ (1.0) in (c). The RMSD for the LSFC Raman spectra generated from the computed spectra of Al_1 & NO_3^- and $[\text{Al}_1 \cdot 12\text{H}_2\text{O}]^{3+}$ & NO_3^- are 0.0017% and 0.0014%, respectively. The RMSD is computed by excluding the large nitrate peak at $1000\text{-}1150 \text{ cm}^{-1}$.....</p>	118
<p>Figure B.1. Frost diagrams for Zn, Al, H, and N at pH = 0</p>	121
<p>Figure D.1. C-V measurement for AlPO layer with different treatments, indicating the chemically enhanced dehydration effect by adding HfO_2 layer occurs after 5 minutes anneal at $350 \text{ }^\circ\text{C}$. The C-V curve for a bare AlPO layer annealed at $500 \text{ }^\circ\text{C}$ for one hour is shown for comparison.....</p>	127
<p>Figure D.2. High resolution TEM image of the cross section of an AlPO-HfO_2 stack annealed at $350 \text{ }^\circ\text{C}$ for 5 minutes.</p>	127
<p>Figure D.3. X-ray reflectivity (XRR) spectrum of a $\sim 30 \text{ nm}$ AlPO layer on silicon wafer after one hour anneal $350 \text{ }^\circ\text{C}$. The calculated spectrum was generated by assuming a homogeneous AlPO layer. Although the critical angle and the amplitude of Kiessig fringes are consistent between the experimental and calculated spectra, the overall fit is not good. This indicates a possible missing component in the sample.</p>	128
<p>Figure D.4. The same experimental XRR spectrum in Figure D.3 with a different calculated spectrum. Here, the calculated spectrum was generated by assuming a thin but highly dense AlPO surface layer. By adding the surface “crust”, the over fitting improves significantly from Figure D.3.....</p>	129

LIST OF TABLES

<u>Table</u>	<u>Page</u>
Table 4.1. Thin film thickness at different annealing temperatures as determined via spectroscopic ellipsometry.	55
Table 4.2. Dielectric characteristics of aluminum oxide thin films annealed at different temperatures. An identical measurement of a MIS capacitor with 100 nm thermally grown SiO ₂ dielectric layer was included as reference.	57
Table A.1. Unit cell parameters of crystals obtained from cathode solutions with different pH values.....	90
Table A.2. The coefficients of the component Gaussian functions of the LSFC-Raman.....	100
Table A.2. The coefficients of all the component Gaussian functions of the LSFC-Raman (continued).....	101
Table A.2. The coefficients of all the component Gaussian functions of the LSFC-Raman (continued).....	102
Table A.2. The coefficients of all the component Gaussian functions of the LSFC-Raman (continued).....	103
Table A.2. The coefficients of all the component Gaussian functions of the LSFC-Raman (continued).....	104
Table D.1. Thickness data (from spectroscopic ellipsometry) of AlPO and HfO ₂ layer in both individual layer and the AlPO-HfO ₂ stack after one hour anneal at 350 °C. This shows the HfO ₂ does not necessarily facilitate the densification of AlPO layer at low temperature even as it promotes the dehydration of AlPO.	128

Introduction

Let's start with something in our daily lives. You are standing in your friend's family kitchen. On the counter rests a baking plate, glassware, a small balance, a mixer, and a spray bottle. The oven has been pre-heated. What would you picture your friend's family is about to do? The answer will most likely be baking bread or a cake. During this family activity, kids are running around, laughing and shouting. Wheat flour, milk, and other ingredients are constantly spilled over the counter or on the floor. The couple casually wipes off the spill while interacting with the kids. Nobody even bothers to put on an apron. The place might not be very organized, but everyone seems so happy and relaxed.

Now, again, imagine yourself standing outside of a very clean laboratory (called a cleanroom). A harsh red-sign labeling "restricted area" appears at the entrance while a bright yellow-sign showing "hazardous materials" sits next to it. One can only enter with an authorized keycard or the correct password. Looking through the big window, the space is filled with shiny and probably expensive equipment: sphere chambers, blinking green lights, and red emergency stop buttons. Everyone working on the other side is dressed in a full-body suit, covering from head to toe with only a small opening for their eyes to see through. You try to read their personalities from their eyes, just like peering through the veil of an Arabian woman. These people are all moving slowly and carefully (even robotically sometimes) around the instruments, following every step of a standard operating procedure.

This is not a scene from the "Resident Evil". In fact, there are a few semiconductor fabrication plants with cleanrooms like this in Oregon, US, primarily owned by the electronics industry. They are the birth place of the technologies driving your favorite electronics, which could be a large area flat panel display, a 10-inch tablet, or a 4-inch smart phone. As you might suspect, a

facility like this takes billions of dollars to set up and posts large annual costs on just regular operation and maintenance. Many protocols need to be developed and followed during instrument operation and while dealing with hazardous chemicals. It is common for us to complain about the high cost of newly released consumer electronics, but we ignore the multi-billion capital investments necessary for manufacturing.

What if we can make these electronics, or at least part of them, with the kitchen gear in your friend's kitchen? Well, it may sound like a day dream. Certainly, there will be many challenges. But just like all "epidemics", it may start from a small step. *This is why my dissertation is dedicated to the pursuit of this dream by presenting some initial efforts made by a chemist.*

To do this, we need to first identify the component in a flat panel display that can be used as the test vehicle for our approach. Knowing requirements for material property, we can then choose the proper material and design the chemical synthetic pathway. By carefully control the reaction pathway, our goal is to simplify the material synthetic process while the end product still exhibits properties suitable for electronic use.

To start, Thin Film Transistor (TFT) is what got our attention. It is a critical electronic device used by the display industry as the dimmer switch for the pixels in the display. Fig. 1 shows the structure of a staggered bottom gate TFT (the simplest structure). A TFT utilizes three different types of materials, including conductor, semiconductor, and dielectrics. Their differences originate from their responses to added electrical field. A conductor contains free charge carriers, e.g., negatively charged electrons, that move under an external field and generate electric current. In an insulator, on the other hand, charge carriers are bonded tightly and cannot move freely under an external field. However, they can be shifted to some extent, which then generates an internal field to counter-balance the external field. A semiconductor is a material that acts like dielectric materials under

no or low external field. Once the field strength reaches a certain level, some carriers are loosened from the solid network and the material starts to act like a conductor. In a TFT, the source, drain, and gate contacts are conductors; the active channel layer is a semiconductor; and the gate dielectric layer is an insulating during device measurement, the source electrode is usually grounded. The drain and gate electrodes can be set to different potentials, which create the drain voltage (V_{DS}) and gate voltage (V_{GS}) relative to the source electrode. V_{DS} is generally set to a constant. Before applying V_{GS} , the channel layer is insulating and there is no current flowing from source to drain (device off-state). After applying V_{GS} , the gate dielectric layer generates an internal field, which, upon V_{GS} reaching the turn-on voltage, enables conduction in the channel layer near the dielectric-semiconductor interface. It makes this interface the most delicate part of the device.

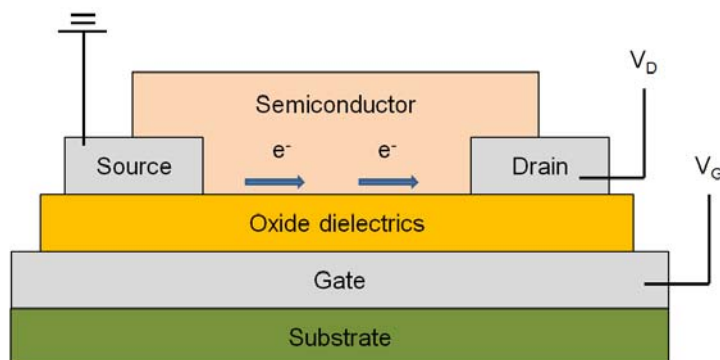


Figure 1.1. A cross-sectional schematic of a simple bottom gate thin-film transistor.

A smooth dielectric-semiconductor interface enables optimum TFT. Since electrons are moving fast at the dielectric-semiconductor interface during TFT operation, they can be imagined (at least to some extent) as fast moving cars on a highway. Fig. 2 shows what the car (electron) sees on a flat highway (smooth interface) and an up-and-down highway (rough interface). The car can run at a higher speed on a flat highway and similarly the electron can move faster at a smooth interface, which means the device will have a higher mobility and exhibits a faster switching speed. Driving on a flat highway, a car can achieve higher gas

mileage due to smaller change in speed. Similarly, the energy to move the electrons (TFT power consumption) can also be lowered by a smooth interface. Most importantly, the car driving on the flat highway will suffer from less vibration (up and down movements). It is similar for the electrons in an operating TFT, where the smooth interface ultimately can lead to an improvement on the device stability.

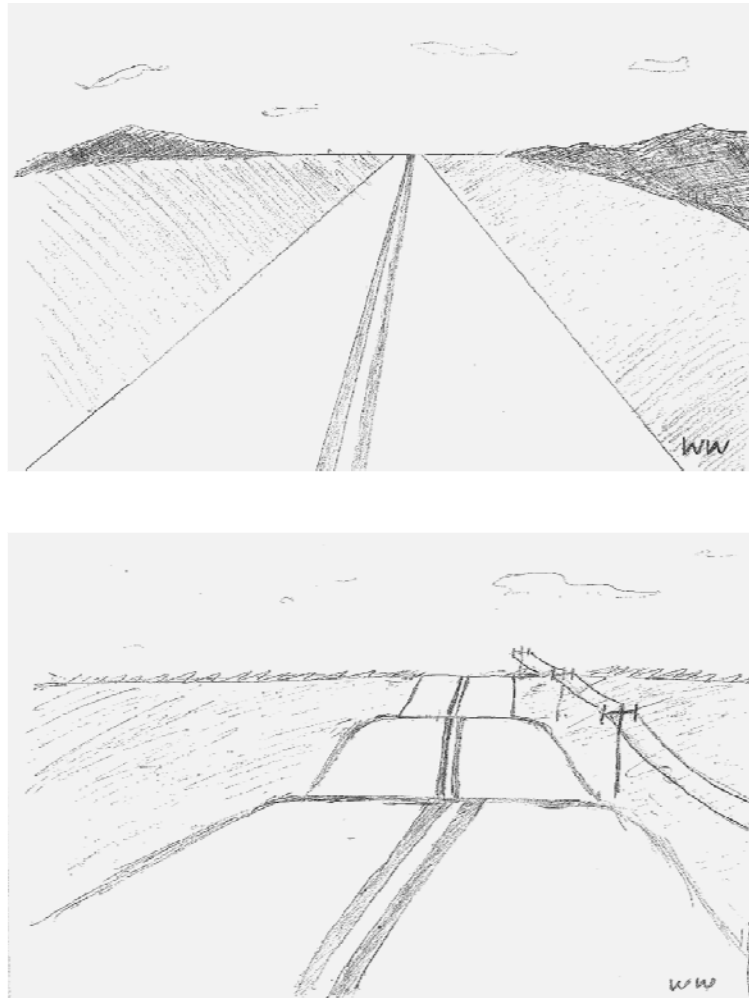


Figure 1.2. Sketches of a flat highway (upper) and an up-and down highway (lower)

In reality, the interface roughness is mainly introduced by the surface roughness of the dielectric layer. Thus, the deposition of a smooth, dense, and defect free dielectric layer is critical during TFT fabrication. The most commonly used

dielectric layer is silicon dioxide (SiO_2), which can be grown thermally on silicon wafers at about 1100 °C under water vapor. This process has been used in the electronic industry for decades. The thermally grown SiO_2 is an ideal insulator material that exhibits characteristics that are difficult to surpass by other dielectric materials, e.g., good interface with silicon, low defect density, and high breakdown field strength. And this is essentially why the current CMOS industry is based on silicon technology. However, thermal oxidation of silicon wafer is the only way to obtain such high quality SiO_2 dielectrics. SiO_2 cannot be deposited onto a non-silicon substrate with the same properties. Therefore, for transparent devices on glass or flexible electronics on polymer substrates, other dielectric materials need to be developed. Several dielectric materials have been investigated as candidates, for example, HfO_2 , Al_2O_3 , and Ta_2O_5 .¹ Most of these materials were investigated via vacuum based deposition techniques, which happen in a space containing very little gas except the product related species. This ensures the deposition of pristine, homogeneous thin films exhibiting desired morphology. Here, we will focus on aluminum oxide.

The most intensively study vacuum deposition method for high quality Al_2O_3 thin film is “atomic layer deposition” (ALD). During a typical ALD process, two reagent gases are introduced into the chamber in a sequential manner. Reaction only occurs between the surface adsorbed reagents (ideally only “one atomic layer”), which ultimately leads to high quality oxide films. As one could imagine, thousands of pumping and purging cycles need to be executed for deposition of even a very thin aluminum oxide film (it might take an ALD instrument up to two hours to deposit a thickness of 100-nm); in addition, most of the starting materials end up on the chamber wall or in the waste collector. Moreover, the size of the chamber limits the size of the substrate and the instrumental investment increases exponentially with the increasing chamber size, eventually reflected in the high cost of large area electronics manufacturing.

A potential cost-saving alternative for large area electronics is to adopt a solution-deposition route for the materials. The concept of solution processed thin-film-deposition has been brought out and researched intensively in the past two decades. Various methods and advantages have been reviewed.^{2,3} Some of its advantages (from a production point of view) over conventional vacuum deposition methods can be simply summarized as below:

1. Eliminate the capital intensive vacuum deposition tools.
2. Improve material efficiency (most materials end up on the chamber wall during vacuum deposition)
3. Reduce energy consumption (no high energy plasma needed)
4. High deposition throughput over large area without chamber size confinement

For aluminum-oxide thin films, traditional solution deposition method is usually referred as the “sol-gel” method, which typically involves the synthesis of a sol precursor containing hydroxide nano-particles, e.g., through dispersing colloidal particles or metal-organic compound hydrolysis. However, thin films deposited from sol-gel method are usually porous and exhibit rough surfaces (up to a few nanometers in root-mean-square roughness).⁴⁻⁶ The rough surface and its porous nature originate from the building units, i.e., the particles presented in the precursor sol. They are tens of nanometers in size. A straight forward analogy is shown in Fig. 3. When the small vial is packed with solid spheres, lots of voids can be found in between the spheres and the top surface appears very uneven. When fine powder is used to fill the same vial instead of spheres, voids in the bottle are significantly decreased and the surface appears to be much smoother. Therefore, looking for a smaller building unit rather than nano-particles should intrinsically improve the aluminum oxide thin-film properties.



Figure 1.3. Two glass vials filled to the same level. One contains solid spheres and the other contains fine powder.

In the search of a desired building unit, we found an interesting aluminum hydroxide cluster material – the “flat” Al_{13} cluster, shown in Fig 4. The diameter of this cluster is about 1 nm, which seems like a desirable building unit for the aluminum oxide layers. However, there is very little work done previously even on the synthesis of this cluster, not to mention using it as a precursor to make aluminum oxide thin films. Prior studies about the synthesis of this cluster are all reported in small scale with long reaction time and low yield.^{7,8} It is necessary to first develop an alternative synthetic method to produce this compound in gram scale so we can use it to make solution precursors. The question comes: how to do it?

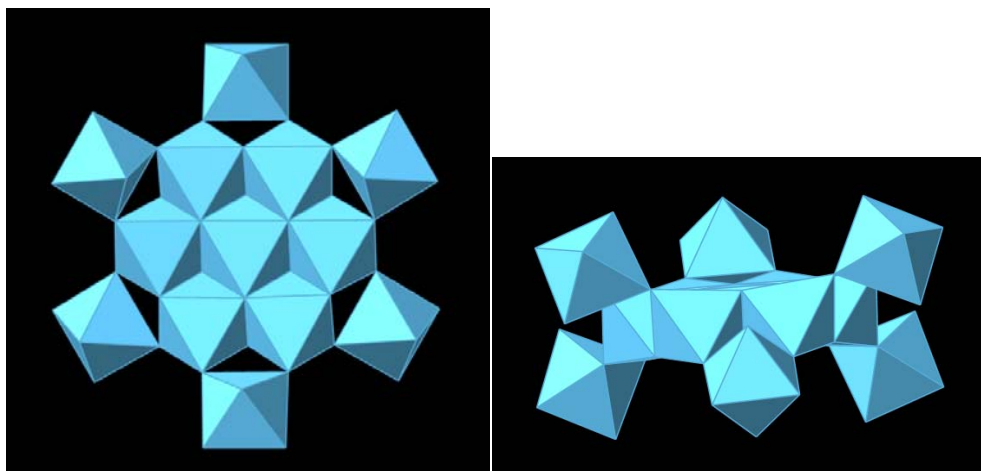


Figure 1.4. Structure of “flat” Al_{13} : (left) top view, (right) side view.

Once we’ve got enough “flat” Al_{13} clusters in a synthetic compound and it can produce the solution precursor for thin-film deposition, the question still remains unanswered regarding its behavior during solution-solid conversion. Can this solution-precursor overcome problems faced by the sol-gel method?

Meanwhile, one of the difficulties researchers meet when using solution-processed thin films as dielectric layers is the residual solvent, which is water in our case. In oxide films, water can also exist as hydroxides, which can require significant energy input and high temperatures to eliminate. A low-temperature dehydration route would promote the real-world application of solution processed thin film deposition.

During a TEM study of a hydrated solution-deposited thin film (aluminum oxide with 10% phosphate), I discovered that the film dehydrated under the exposure with the electron beam. In Fig. 5(a), the “water regions” are shown as the area with lighter contrast at the beginning of the experiment. As the experiment proceeds, the “water regions” migrate and aggregate, shown in Fig. 5(b). It appears that the water might move quite easily in the bulk. Therefore, I became very interested into what

really limits the dehydration property of a solid material. Is it the bulk property or the material's surface? A daily life example might shed light on the answer.

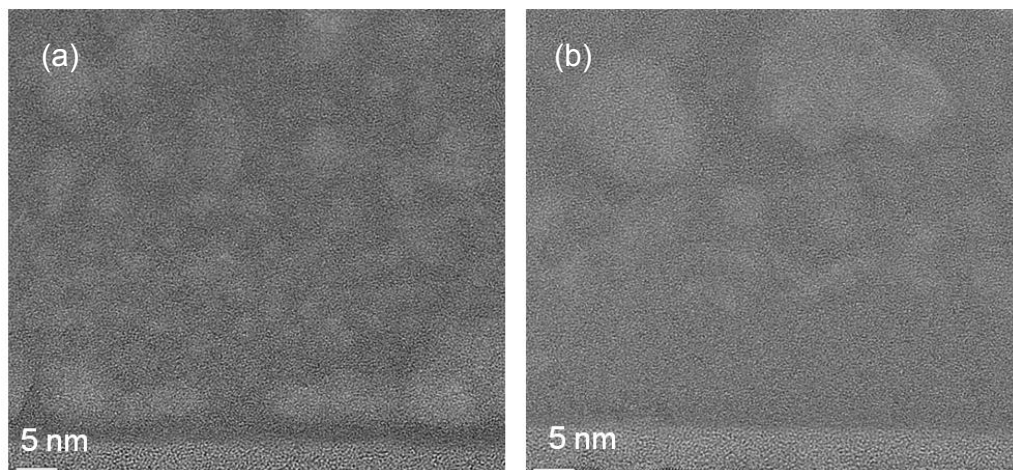


Figure 1.5. Cross section TEM images of an aluminum phosphate oxide film at (a) 0 minutes; (b) 30 minutes.

I've run into situations like Figure 1.6 before, and the first thing that comes to my mind is the need for a paper towel or a sponge to soak up the spilled area. Yes, a "surface layer" helps to get the water out from the carpet. This is straightforward on the carpet. However, when it comes to oxide, what can we do to promote its dehydration so the water will leave the material at lower temperature?



Figure 1.6. Coffee spill....

In this dissertation, we will explain our approaches to solve all these problems by carefully *Designing and Controlling the Reaction Pathway*. Here is how this dissertation will attempt to answer these questions:

In Chapter 2, an alternative method for adjusting aqueous solution pH, rather than the conventional base titration, is developed. By adjusting the method of introducing pH change in aqueous aluminum solutions, the condensation pathway of aluminum aqueous species can be controlled, which leads to the unique “flat” Al_{13} structure. The method demonstrates the gram-scale pure inorganic synthesis of the “flat” Al_{13} compound.

In Chapter 3, the aqueous aluminum condensation pathway designed in Chapter 2 is further exploited to create a reagent-less electrolytic synthesis of “flat” Al_{13} cluster. The electrolytic synthesis also enables the precise solution pH control, which allows the speciation study of aluminum aqueous solution via Femtosecond Stimulated Raman Spectroscopy (FSRS). The formation process and possible intermediate species during the formation of “flat” Al_{13} clusters are discussed on the basis of the spectroscopic results.

In Chapter 4, aluminum oxide thin films are deposited from a solution precursor made from the “flat” Al_{13} compound via a simple spin-coating method. By changing the precursor design, we can control the reaction path during solid conversion, which leads to high-quality thin films. The thin films were characterized by various techniques. Metal-insulator-semiconductor capacitor and TFT devices were made with solution-processed aluminum oxide layer as the dielectric layer. Electrical properties of these two types of devices were characterized.

Finally, in Chapter 5, a chemical-dehydration enhancement method was developed to effectively reduce the dehydration temperature of an aluminum oxide based dielectric material – aluminum phosphate oxide (AlPO). The dehydration path of AlPO was simply modified by depositing a thin surface layer. By applying this surface layer to the AlPO surface, the dehydration temperature was decreased by as much as 250 °C. The interface region between the surface layer and the AlPO layer was characterized. Its dehydration behavior was studied both chemically and electrically to demonstrate the enhancement effect on the dehydration property due to the surface modification.

Hopefully, I have you sufficiently interested, so you keep turning another few pages to learn about my research findings.

Let the chemistry begin.

References

- 1 Wilk, G. D., Wallace, R. M. & Anthony, J. M. High-k gate dielectrics: Current status and materials properties considerations. *Journal of Applied Physics* **89**, 5243-5275 (2001).
- 2 Hibberd, C. J. *et al.* Non-vacuum methods for formation of Cu(In,Ga)(Se,S)₂ thin film photovoltaic absorbers. *Prog. Photovoltaics* **18**, 434-452, doi:10.1002/pip.914 (2010).
- 3 Pasquarelli, R. M., Ginley, D. S. & O'Hayre, R. Solution processing of transparent conductors: from flask to film. *Chem. Soc. Rev.* **40**, 5406-5441, doi:10.1039/c1cs15065k (2011).
- 4 Zhang, W., Liu, W. & Xue, Q. Characterization and tribological investigation of Al₂O₃ and modified Al₂O₃ sol-gel films. *Materials Research Bulletin* **36**, 1903-1914 (2001).
- 5 Yamaguchi, N., Tadanaga, K., Matsuda, A., Minami, T. & Tatsumisago, M. Antireflective properties of flowerlike alumina thin films on soda-lime silica glass substrates prepared by the sol-gel method with hot water treatment. *Thin Solid Films* **515**, 3914-3917, doi:10.1016/j.tsf.2006.11.009 (2007).
- 6 Kumar, L., Saha, D., Khan, S. A., Sengupta, K. & Islam, T. A Medium-Range Hygrometer Using Nano-Porous Thin Film of gamma-Al₂O₃ With Electronics Phase Detection. *IEEE Sens. J.* **12**, 1625-1632, doi:10.1109/jsen.2011.2172979 (2012).
- 7 Seichter, W., Mogel, H. J., Brand, P. & Salah, D. Crystal structure and formation of the aluminium hydroxide chloride [Al₁₃(OH)₂₄(H₂O)₂₄]Cl₁₅ center dot 13H₂O. *Eur. J. Inorg. Chem.*, 795-797 (1998).
- 8 Gatlin, J. T., Mensinger, Z. L., Zakharov, L. N., MacInnes, D. & Johnson, D. W. Facile Synthesis of the Tridecameric Al₁₃ Nanocluster Al₁₃(μ₃-OH)₆(μ₂-OH)₁₈(H₂O)₂₄(NO₃)₁₅. *Inorg. Chem.* **47**, 1267-1269 (2008).

**Chapter 2: Synthesis of Hydroxide Cluster $[\text{Al}_{13}(\mu_3\text{-OH})_6(\mu\text{-OH})_{18}(\text{H}_2\text{O})_{24}]^{15+}$
from Aqueous Solution**

Wei Wang, Katherine M. Wentz, Sophia E. Hayes, Darren W. Johnson, and

Douglas A. Keszler

Main Text

Aluminum is the third most abundant element in the terrestrial environment, occurring in a wide variety of rocks and minerals. In water, the Al^{3+} aqua ion hydrolyzes to produce a variety of molecular species and hydroxide phases. These phases are key elements in our understanding of aluminum in natural water systems, and they are the basis for several applications and commercial products.¹

Although various types of inorganic polynuclear aluminum hydroxide nanoclusters have been proposed to exist in water, only a few examples have been isolated.^{1,2} The known structure types are generally grouped into two distinct classes. The first class comprises structures similar to the ϵ -isomer of the Baker-Figgis Keggin ion, which contains a tetrahedral AlO_4 core surrounded by distorted AlO_6 octahedra sharing edges. This class includes the ions $[\text{Al}_{12}(\text{AlO}_4)(\text{OH})_{24}(\text{H}_2\text{O})_{12}]^{7+}$ and $[\text{Al}_{30}\text{O}_8(\text{OH})_{56}(\text{H}_2\text{O})_{24}]^{18+}$.³⁻⁶ The second class is characterized by the condensation of distorted octahedral AlO_6 units alone, comprising the ions $[\text{Al}_2(\mu\text{-OH})_2(\text{H}_2\text{O})_8]^{4+}$, $[\text{Al}_8(\mu_3\text{-OH})_2(\mu\text{-OH})_{12}(\text{H}_2\text{O})_{18}]^{10+}$, and $[\text{Al}_{13}(\mu_3\text{-OH})_6(\mu\text{-OH})_{18}(\text{H}_2\text{O})_{24}]^{15+}$.⁷⁻¹⁰ As an example of the latter category, the structure of the “flat” Al_{13} cluster $[\text{Al}_{13}(\mu_3\text{-OH})_6(\mu\text{-OH})_{18}(\text{H}_2\text{O})_{24}]^{15+}$ is built around an AlO_6 core that is circumscribed by six additional AlO_6 units through $\mu_3\text{-OH}$ bridges, establishing a coplanar configuration (Figure 2.1). Six additional AlO_6 octahedra are alternately appended above and below the primary plane by sharing O vertexes (Figure 2.1b).

Among the reported aluminum hydroxide clusters, this “flat” Al_{13} has long been an enigma. It is generally not observed in speciation studies, and reported synthetic procedures of inorganic salts suffer from very long reaction times and poor yields.^{1,9} In 2008, however, Gatlin and co-workers¹⁰ demonstrated a facile synthesis of the “flat” Al_{13} cluster from methanol solution. In their work, a methanol solution containing dissolved $\text{Al}(\text{NO}_3)_3$ was treated with an organic nitroso-containing compound, and following evaporation of methanol the cluster was synthesized in yields up to 47% relative to $\text{Al}(\text{NO}_3)_3$. Unfortunately, the use of

highly toxic nitroso-containing compounds hinders the large-scale production of the cluster. Herein, we introduce a green, scalable method for producing the nitrate salt $[\text{Al}_{13}(\mu_3\text{-OH})_6(\mu\text{-OH})_{18}(\text{H}_2\text{O})_{24}](\text{NO}_3)_{15}$ from an aqueous solution.

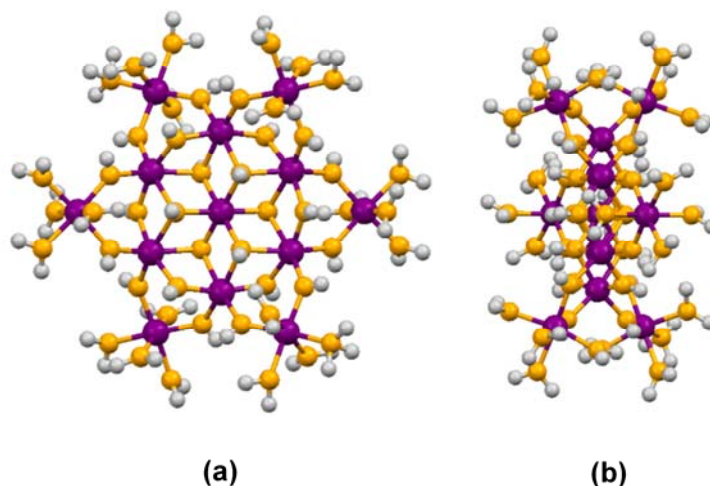


Figure 2.1. Structure of “flat” $[\text{Al}_{13}(\mu_3\text{-OH})_6(\mu\text{-OH})_{18}(\text{H}_2\text{O})_{24}]^{15+}$ cluster: (a) perpendicular to the central plane; (b) parallel to the central plane. Al – violet spheres; O – orange spheres; H – white spheres.

The desired hydroxo Al_{13} cluster should readily form on increasing the pH of a simple aqueous solution of $\text{Al}(\text{NO}_3)_3(\text{aq})$. The synthetic challenge is preventing the formation of the tetrahedral species $\text{Al}(\text{OH})_4^-$, which can lead to nucleation of Keggin-type structures. Solution-speciation and synthetic studies in aqueous solutions have predominately been conducted via titration of an acidic $\text{Al}(\text{NO}_3)_3$ solution with base. Such a procedure, however, favors the formation of tetrahedral species such as $\text{Al}(\text{OH})_4^-$. We have adopted an alternative approach, wherein an active metal, Zn, is used to controllably reduce the acidic nitrate solution. In this way a gradual increase in pH is achieved commensurate with the controlled dissolution of Zn. Nucleation of tetrahedral species is prevented, offering a direct route to the “flat” Al_{13} cluster.

The initial solution was prepared by dissolving 30.01g $\text{Al}(\text{NO}_3)_3 \cdot 9\text{H}_2\text{O}$ (BAKER ANALYZED Reagent, ACS Grade) in Millipore H_2O ($\rho = 18.2 \text{ M}\Omega \cdot \text{cm}$) to make

a 50-mL solution. 2.82 g of zinc metal powder (Alfa Aesar, -140+325 mesh, 99.9% (metals basis)) was then added to this clear solution. The molar ratio between zinc and aluminum was 1:2. The reaction mixture was stirred overnight to ensure that the zinc powder completely dissolved. The clear solution was then filtered into a dish and placed in a fume hood for evaporation of the water. As the solution became concentrated, numerous colorless crystals began to grow, reaching sizes of several mm. Higher yields could likely be realized by increasing the Zn:Al ratio in the reactant mixture. At a ratio of 1:1, however, the mixture transforms into a transparent gel before all of the zinc powder dissolves. Characterization of product phases resulting from the use of high Zn loadings is ongoing.

A crystal was physically isolated from the batch and analyzed by single crystal X-ray diffraction methods (Bruker Apex CCD diffractometer, Mo K α radiation, $\lambda = 0.07073 \text{ \AA}$, $T = 173 \text{ K}$).¹¹ The unit-cell parameters and space group are consistent with those previously reported for $[\text{Al}_{13}(\mu_3\text{-OH})_6(\mu\text{-OH})_{18}(\text{H}_2\text{O})_{24}](\text{NO}_3)_{15}$.¹⁰

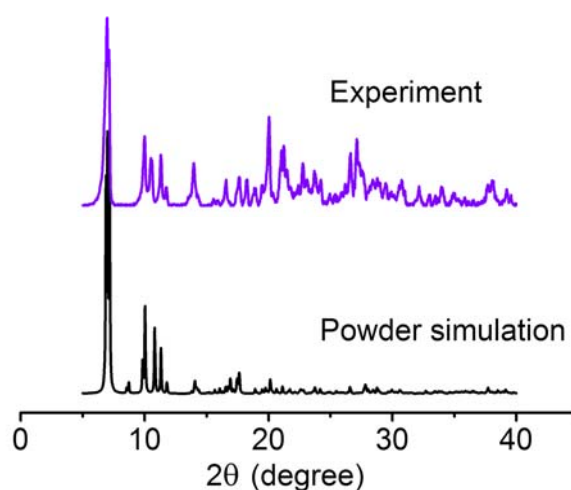


Figure 2.2. X-ray powder diffraction pattern of the polycrystalline sample and powder simulation pattern from single crystal structure of $[\text{Al}_{13}(\mu_3\text{-OH})_6(\mu\text{-OH})_{18}(\text{H}_2\text{O})_{24}](\text{NO}_3)_{15}$

Forced evaporation of the water resulted in a polycrystalline precipitate containing a mixture of the Al nanocluster salt, $\text{Zn}(\text{NO}_3)_2$, and unreacted $\text{Al}(\text{NO}_3)_3$. We have found that $\text{Zn}(\text{NO}_3)_2$ and $\text{Al}(\text{NO}_3)_3$ can be selectively removed by washing the product with isopropanol. The resulting powder was analyzed via powder X-ray diffraction (Rigaku Ultima-IV, Cu $K\alpha$ radiation, step size = 0.02° (2θ)). As seen in Figure 2.2, the experimental diffraction pattern agrees well with that calculated from the reported single-crystal data of $[\text{Al}_{13}(\mu_3\text{-OH})_6(\mu\text{-OH})_{18}(\text{H}_2\text{O})_{24}](\text{NO}_3)_{15}$, confirming synthesis of the desired compound. The yield was calculated to be 55.2% ($\sim 7.2\text{g}$ per batch) on the basis of $\text{Al}(\text{NO}_3)_3$.

The product has also been analyzed with ^{27}Al magic-angle spinning (MAS) solid-state NMR spectroscopy (data not shown). The measurements were conducted in a 2.5-mm HX MAS NMR probe on a 400 MHz NMR Varian Inova spectrometer. Experiments were performed at MAS rotational frequencies of 10 kHz with a ^{27}Al observe frequency of 104.166 MHz. Typical $\pi/2$ pulses were 1.8 μs with recycle delays of 2 s. The ^{27}Al MAS spectrum reveals a set of overlapping quadrupolar-broadened resonances that arise presumably from the three types of six-coordinate Al sites in the cluster (Figure 1). Importantly, we observe no clear indication of a four-coordinate Al species (based on the absence of high-frequency ^{27}Al chemical shifts).¹² To more closely analyze the Al sites, we have performed a multiple-quantum magic-angle spinning (MQMAS) experiment; MQMAS is frequently applied to half-integer quadrupolar spins ($I = 3/2, 5/2, 7/2 \dots$) to resolve resonances that overlap in traditional MAS NMR because of the quadrupolar broadening of the central transition.^{13,14} In the 2D spectrum, the frequency is determined by the isotropic shift along one axis and by the isotropic part of the quadrupole interaction along the other. Thus, narrower lines result from each chemical species, allowing for separation of overlapping, crowded resonances. The results of this experiment are illustrated in Figure 2.3. The spectrum reveals the presence of three distinct Al sites in the powder with different quadrupolar broadening arising from variation in the electric field gradient surrounding each site, which is consistent with the

schematic of different Al centers in the Al_{13} cluster. Additional computational modeling will be required to make assignments of the resonances to specific sites in the cluster.

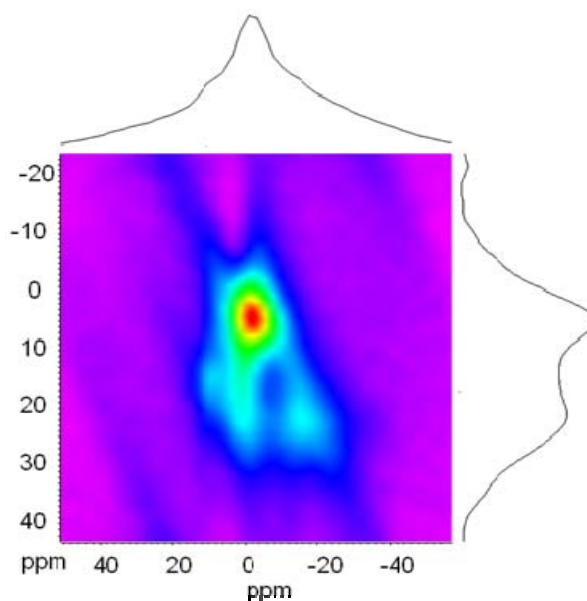


Figure 2.3. ^{27}Al MQMAS of $[\text{Al}_{13}(\mu_3\text{-OH})_6(\mu\text{-OH})_{18}(\text{H}_2\text{O})_{24}](\text{NO}_3)_{15}$.

Previous efforts to examine speciation and preparation of hydroxide clusters in aqueous Al^{3+} solutions have mainly relied on titrating a solution containing aluminum with controlled amounts of base.^{3,4,15,16} This base addition generally leads to immediate precipitation that dissipates on stirring, or the solution is heated to 80-90°C to limit the precipitation. It is well known that the tetrahedral species $\text{Al}(\text{OH})_4^-$ forms at pH as low as 7, becoming the dominant species at high pH¹⁷. Base titration will produce a locally high-pH environment and gradient near the entering droplet, which inevitably forces the formation of $\text{Al}(\text{OH})_4^-$. Once this tetrahedral unit forms, it will quickly condense with six-coordinate Al^{3+} aqua ions existing across the pH gradient to establish the core of a Keggin structure. Heating also favors Keggin formation through forced hydrolysis of the $\text{Al}(\text{OH})_4^-$ unit. A similar mechanism has been proposed on the basis of an ^{27}Al NMR analysis of an aluminum chloride solution titrated with sodium carbonate.¹⁸

In our work, the zinc powder serves as a reducing agent, slowly consuming nitric acid generated from aluminum hydrolysis, which results in a gradual increase in pH of the system. In the absence of a severe pH gradient toward basic conditions, the Al^{3+} ions retain a six-coordinate environment associated with acidic conditions. The rising pH then forces condensation of these species to form the “flat” Al_{13} cluster. We have found that the technique can be extended by using aluminum metal in place of zinc metal, but here the native oxide coating of the aluminum metal produces a by-product that is difficult to remove from the product. In a similar way, the slow dissolution of $\text{Al}(\text{OH})_3(\text{s})$ in $\text{Al}(\text{NO}_3)_3(\text{aq})$ can be used to gradually raise the pH and selectively precipitate the Al cluster. We note that related methods have been used to prepare sulfate salts of the clusters $[\text{Al}_2(\mu\text{-OH})_2(\text{H}_2\text{O})_8]^{4+}$ and $[\text{Al}_8(\mu_3\text{-OH})_2(\mu\text{-OH})_{12}(\text{H}_2\text{O})_{18}]^{10+}$ by reacting excess aluminum-metal powder with sulfuric acid.^{7,8}

With this strategy, we have been able to readily scale the production of $[\text{Al}_{13}(\mu_3\text{-OH})_6(\mu\text{-OH})_{18}(\text{H}_2\text{O})_{24}](\text{NO}_3)_{15}$ to large quantities. Such quantities have proven useful for examining the material as the precursor to solution-processed Al_2O_3 and related thin films for electronics. We will describe findings from these studies in forthcoming contributions.

The synthesis also provides new insight into the speciation of Al^{3+} in aqueous systems. Throughout the long history of aluminum chemistry, Keggin ions have become known as dominating species in weakly acidic aqueous environments. Our results indicate that this state of affairs may largely be a result of the method – solution-based titration – that is used to control pH and force condensation. We have provided a reaction pathway that leads to an “uncommon” product, ostensibly under the same pH conditions leading to formation of the Keggin ion. Hence, care should be taken in interpreting speciation studies conducted via a standard titration, especially where the coordination environment of a metal ion changes as a function of pH. In such systems, titration can be an especially *unnatural* way to establish the metal-ion chemistry of a *natural* water system.

References:

- (1) Casey, W. H. *Chemical Reviews* **2006**, *106*, 1-16.
- (2) Casey, W. H.; Phillips, B. L.; Furrer, G. In *Nanoparticles and the Environment*; Mineralogical Soc America: Washington, 2001; Vol. 44, p 167-190.
- (3) Johansson, G. *Acta Chem. Scand.* **1960**, *14*, 771- 773.
- (4) Johansson, G.; Lundgren, G.; Sillen, L. G.; Soderquist, R. *Acta Chem. Scand.* **1960**, *14*, 769- 771.
- (5) Allouche, L.; Gerardin, C.; Loiseau, T.; Ferey, G.; Taulelle, F. *Angewandte Chemie-International Edition* **2000**, *39*, 511-+.
- (6) Rowsell, J.; Nazar, L. F. *Journal of the American Chemical Society* **2000**, *122*, 3777-3778.
- (7) Johansson, G. *Acta Chemica Scandinavica* **1962**, *16*, 403-420.
- (8) Casey, W. H.; Olmstead, M. M.; Phillips, B. L.; Phillips, L. *Inorganic Chemistry* **2005**, *44*, 4888-4890.
- (9) Seichter, W.; Mogel, H. J.; Brand, P.; Salah, D. *European Journal of Inorganic Chemistry* **1998**, 795-797.
- (10) Gatlin, J. T.; Mensinger, Z. L.; Zakharov, L. N.; MacInnes, D.; Johnson, D. W. *Inorg. Chem.* **2008**, *47*, 1267-1269.
- (11) Crystal diffraction data: triclinic, space group $P\bar{1}$, $a = 12.877(4)\text{\AA}$, $b = 13.122(6)\text{\AA}$, $c = 13.361(10)\text{\AA}$, $\alpha = 79.86(4)^\circ$, $\beta = 73.46(3)^\circ$, $\gamma = 88.80(4)^\circ$, $V=2128(2)\text{\AA}^3$
- (12) Fitzgerald, J. J.; Kohl, S. D.; Piedra, G.; Dec, S. F.; Maciel, G. E. *Chemistry of Materials* **1994**, *6*, 1915-1917.
- (13) Frydman, L.; Harwood, J. S. *Journal of the American Chemical Society* **1995**, *117*, 5367-5368.
- (14) Massiot, D.; Touzo, B.; Trumeau, D.; Coutures, J. P.; Virlet, J.; Florian, P.; Grandinetti, P. J. *Solid State Nuclear Magnetic Resonance* **1996**, *6*, 73-83.

- (15) Gorz, H.; Schonherr, S.; Pertlik, F. *Monatshefte Fur Chemie* **1991**, *122*, 759-764.
- (16) Schonherr, S.; Gorz, H. *Zeitschrift Fur Anorganische Und Allgemeine Chemie* **1983**, *503*, 37-42.
- (17) Baes, C. F.; Mesmer, R. E. *The Hydrolysis of Cations*, 1976.
- (18) Akitt, J. W.; Farthing, A. *Journal of the Chemical Society-Dalton Transactions* **1981**, 1617-1623.

Chapter 3: A New Portrait of Aluminum Speciation in Water

Wei Wang, Weimin Liu, I-Ya Chang, Lindsay A. Wills, Lev N. Zakharov, Paul Ha-
Yeon Cheong, Shannon W. Boettcher, Chong Fang, Douglas A. Keszler¹

To be submitted to PNAS

Introduction

Aluminum (Al) is the most abundant metallic element in the Earth's crust. It plays significant roles in soil chemistry and plant growth.^{1,2} Our lives are influenced every day by its use in the electronics industry,³⁻⁵ in cooking and eating utensils, in food packaging, and as a structural material in construction, automotive, and aircraft industries. Millions of tons of Al compounds are used worldwide each year for water treatment; it is found in all drinking water.⁶

The nature of Al in water systems governs mineral migration, soil chemistry, and bioavailability,⁷ while also prescribing its role in life processes. Despite more than a century of study,^{8,9} many details of aqueous Al chemistry remain unresolved. Studies are made difficult by the variety and complexity of the species found in water, which encompass monomeric, oligomeric and polymeric hydroxides,¹⁰⁻¹⁶ colloidal solutions and gels, and precipitates. For example, while the *flat* cluster $[\text{Al}_{13}(\mu_3\text{-OH})_6(\mu_2\text{-OH})_{18}(\text{H}_2\text{O})_{24}]^{15+}$ does not appear in common predominance diagrams,^{17,18} it can now easily be synthesized in large quantities.¹⁹⁻²¹ In the laboratory, targeted species are generally prepared by adjusting pH via conventional titration or electrochemistry,^{22,23} they are then characterized by selected analytical techniques. For Al, the method and rate of changing pH may have significant effects with respect to species formation. Its slow water exchange rate (1 s^{-1}), evolution of coordination number from six to four at $\text{pH} < 7$, and cation involvement with base titration all need to be considered in designing experiments. In addition to these issues, limited spectroscopic signatures have historically hindered detailed structural characterization. While several techniques are available for determining size, shape, and metal nuclearity of Al and other metal clusters in solution, few methods have yet to be demonstrated for the direct *in-situ* determination and assignment of the actual molecular-level structure of an identified species.

Here, we report a new combined experimental and computational platform for studying nanocluster species in water and elucidating their formation and chemical

structure. An electrolysis method is developed to avoid steep pH gradients and precisely control pH, thereby offering improved regulation of species formation. With this method, we also demonstrate atom economy in synthesis, as only a single reagent is required to produce a desired product. Species in solution are analyzed in real time by a newly improved femtosecond stimulated Raman (FSR) technique to detect weak signals associated with structure-defining vibrational modes. The resulting pH-dependent Raman spectra are interpreted by using quantum-mechanically computed vibrational modes to assign specific molecular structures. Through this integrated approach, we have discovered a speciation behavior for Al in water that has not previously been observed.

Methods

Electrochemical Synthesis.

The 1.0 M $\text{Al}(\text{NO}_3)_3$ (aq) starting solution was made with $\text{Al}(\text{NO}_3)_3 \cdot 9\text{H}_2\text{O}$ (Baker Analyzed Reagent, ACS Grade) and ultrapure water ($\rho = 18.2 \text{ M}\Omega \cdot \text{cm}$). Constant current bulk electrolysis was carried out using an EG&G 263A potentiostat in 2-electrode mode with the reference electrode input lead connected to the counter electrode. A custom-built two-compartment cell, comprising a 15 ml cathode, a 50 ml anode, and a standard medium porosity glass frit (Chemglass) to separate the two compartments was used. The solution volumes in the cathode and anode were 10 mL and 30 mL, respectively. Pt wire coils were used for both electrodes. To minimize local pH gradients in the cathode compartment where the cluster is synthesized, the cathode solution was stirred rapidly during electrolysis and a large-surface-area (23 cm^2) Pt wire coil was used as the working electrode. The current was set to 75 mA during the experiment, which required ca. 4 V across the working and counter electrode due to the kinetic overpotentials associated with the hydrogen and oxygen evolution reactions as well as the series resistance of the two-compartment cell. The charge Q was determined by $Q = I \cdot t$. No significant temperature changes were observed during the prolonged electrolysis reaction,

consistent with the low power dissipation ($75 \text{ mA} \times \sim 4 \text{ V} = 0.3 \text{ W}$). The pH of the cathode compartment solution was monitored insitu using an ion-sensitive-field-effect-transistor pH probe. Upon reaching the desired pH, the cathode solution was directed into a flow cell for the in situ femtosecond Raman spectroscopic measurements.

Femtosecond Stimulated Raman Spectroscopy.

The femtosecond stimulated Raman (FSR) spectroscopic setup consists of a mode-locked Ti:sapphire oscillator (Mantis-5) and regenerative amplifier (Legend Elite-USP-1K-HE, Coherent), which provides 35 fs, 800 nm pulses with ~ 4.1 mJ/pulse energy at 1 kHz repetition rate. The fundamental beam of ~ 1.6 mJ/pulse energy is dispersed by a reflective grating (1200 grooves/mm, 750 nm blaze), and passed through a 90- μm -width slit to generate the Raman pump of $\sim 10 \text{ cm}^{-1}$ bandwidth and ~ 3.5 ps pulse duration. The Raman probe represents a new advancement of conventional methods, which originates from cascaded four-wave-mixing (CFWM) sideband signals generated by crossing two laser pulses (the 800 nm beam, ~ 35 fs, $3 \mu\text{J/pulse}$; and the IR component of the super-continuum white light generated in a 2-mm-thick sapphire plate followed by prism compression, ~ 45 fs, 100 nJ/pulse) in a 0.1-mm-thick BBO crystal (Type-I, $\theta=27.8^\circ$). The incident beam diameters on the crystal are $\sim 0.2 \text{ mm}$ and the crossing angle is $\sim 6^\circ$. One of the CFWM signals with $\sim 900 \text{ nm}$ center wavelength is selected as the Raman probe, corresponding to the Stokes frequency range from $100\text{--}3000 \text{ cm}^{-1}$ and pulse duration of ~ 30 fs. Raman pump and probe beams are then focused onto the 1-mm-pathlength sample flow cell by an off-axis parabola. Only the transmitted probe beam carrying the stimulated Raman signal goes into the spectrograph to be dispersed by a 600 grooves/mm grating (1000 nm blaze) and imaged onto a CCD camera (PIXIS 100F, Princeton Instruments), which consists of 1340×100 pixel array and is synchronized with the laser repetition. Each sample spectrum is averaged from 180,000 Raman spectra within ~ 6 min, and the 1.0-M $\text{Al}(\text{NO}_3)_3$ precursor solution spectrum is collected in exactly the same manner right before

each pH-specific sample solution measurement as the standard for NO₃⁻ mode intensity normalization and generation of the differential FSR spectra. Both the spectral dips and peaks in the differential spectra are multi-gaussian least-squares fitted across the wide spectral range, and the integrated peak areas are plotted versus pH to capture the evolution of the signal intensity during electrolysis.

Computations.

The geometries and spectra of the aluminum clusters of interest (Figure A.4) were computed by using HF/6-31G(d,p) with IEFPCM-UFF continuum solvation model for water.²⁷⁻³⁰

Least-Squares Fitting Procedure.

i) Each computed Raman vibrational mode was mathematically described with a Gaussian function using the computed Raman vibrational frequency and intensity. A frequency parameter (F) was used to modulate the frequencies of all species, amplitude parameters (A_i) for the amplitude of each species, and width parameters (W_{ij}) for the width of each Gaussian. The sum of all Gaussian curves constitutes the LSFC-Raman spectrum. ii) The parameters (F , A_i , and W_{ij}) were then iterated to minimize the root-mean-square deviation (RSMD) between the trial LSFC-Raman and the experimental spectrum. The vibrational modes of all eliminated peaks were checked and verified manually for chemical relevance. iii) The individual Gaussians in the final LSFC-Raman spectra can then be identified according to the functional groups.

Results and Discussion

We examine species formation by smoothly increasing the pH of a 1.0-M Al(NO₃)₃ (*aq*) solution. The predominant Al species in this solution is known to be the simple monomeric hexaaqua ion Al(H₂O)₆³⁺ (*aq*).²⁴ As the pH of the solution increases, condensation of the monomeric ion occurs, leading to the formation of polynuclear Al hydroxide nanoclusters. To prevent the steep pH gradients

commonly associated with base titrations, the pH change is achieved by proton reduction in a two-compartment electrochemical cell (Figure 3.1). The primary reactions contributing to the pH change are the proton reduction and water oxidation half reactions.

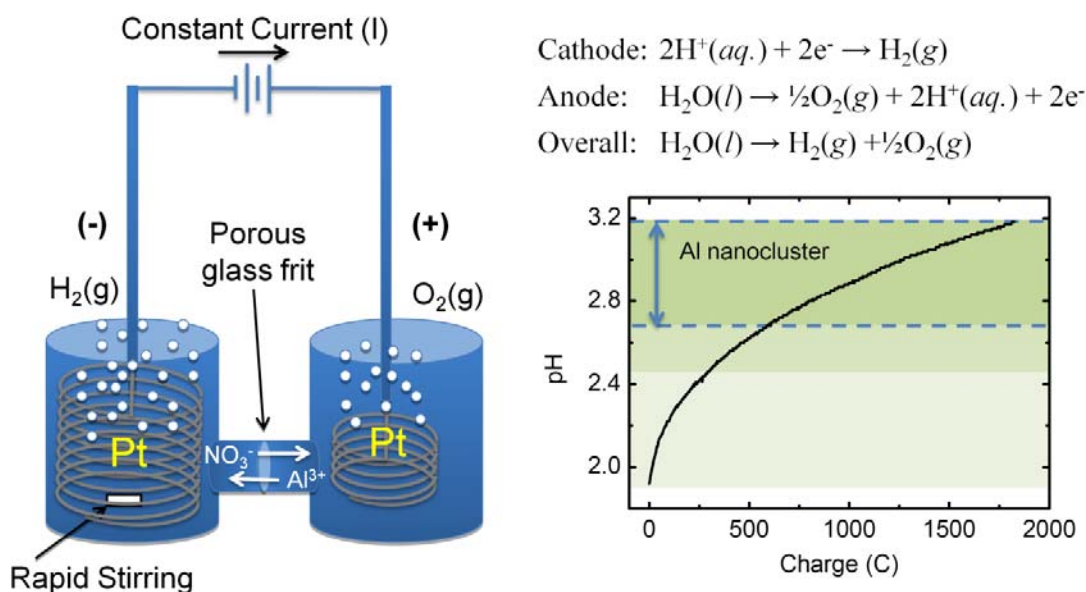


Figure 3.1. (Left) Cell for $\text{Al}(\text{NO}_3)_3(\text{aq})$ electrolysis; (Top right) balanced electrode reactions under acidic conditions; (Bottom right) cathode solution pH vs. total charge passed through the system; the region of Al nanocluster formation is highlighted.

In the cathode compartment, protons are reduced to hydrogen gas, increasing the pH. In the anode compartment, water oxidation results in a decrease in pH. The reaction rate is controlled by adjusting the current through the cell. A porous glass frit eliminates convective mixing between the two compartments. Because the NO_3^- and $\text{Al}(\text{H}_2\text{O})_6^{3+}$ are present in large concentrations, i.e., ~ 3.0 and 1.0 M, respectively, relative to H^+ in the pH range explored, the bulk of the charge-balancing ionic current across the frit is carried by NO_3^- migration into the anode compartment and $\text{Al}(\text{H}_2\text{O})_6^{3+}$ migration into the cathode compartment. The pH of the cathode compartment is plotted against total charge passed in Figure 3.1. In

this study, we primarily focus on the highlighted range of pH = 2.70 - 3.18, as it covers the initial formation of Al hydroxide nanoclusters.

The Keggin Al₁₃ hydroxide nanocluster is the most commonly observed polynuclear species in pH-based speciation studies.^{22,23} The Keggin structure is characterized by a core, tetrahedral AlO₄ unit surrounded by twelve AlO₆ octahedra. A solution ²⁷Al NMR spectrum (Figure A.1) of the final cathode solution (pH = 3.18) indicates only a minor presence of Al atoms in a tetrahedral site associated with the Keggin Al₁₃ structure. Consistent with this observation, we find that all crystals obtained from cathode solutions in the pH range 2.60 - 3.10 exhibit unit-cell parameters (Table A.1) equivalent to that of the *flat* Al₁₃ cluster [Al₁₃(μ₃-OH)₆(μ₂-OH)₁₈(H₂O)₂₄]¹⁵⁺. This cluster contains only distorted octahedral AlO₆ groups, lacking the tetrahedral AlO₄ core of the Keggin cluster. The ease of isolating the *flat* cluster also points to the efficacy of the electrolysis method for synthesis.

To monitor the formation of the *flat* Al₁₃ cluster as a function of pH, the cathode solution was studied *in situ* by nonresonant (800 nm) FSR spectroscopy with a newly developed Raman probe pulse. The probe pulse is selected from one of the cascaded four-wave-mixing signals generated by crossing two femtosecond near-IR laser pulses, providing good spatial separation between self-compressed multicolor sideband signals²⁵ and the fundamental beams for broad spectral coverage (Figure A.2). This setup enables the measurement of stimulated Raman signals to frequencies as low as 350 cm⁻¹, significantly extending established low-frequency detection limits, ca. 600 - 800 cm⁻¹, of conventional probe-light generation in FSR spectroscopy. To capture subtle spectral changes and correct for the effects of laser fluctuations, the spectrum of a control 1.0-M Al(NO₃)₃ (*aq*) solution was acquired before measuring each pH-specific sample.

The resulting differential FSR spectra, i.e., the differences between sample and control measurements, across the pH range 1.9 - 3.18 are shown in Figure 3.2. In these spectra, negative peaks represent species being consumed, while positive

peaks represent new species emerging at the cathode. Three pronounced negative peaks appear at 525 (Al–O stretching of $[\text{Al}(\text{H}_2\text{O})_6]^{3+}$), 718, and 1048 cm^{-1} (NO_3^- vibrations).²⁴ Positive signals, associated with polynuclear Al clusters, are centered at 386, 585, 675, 777, 937, 1151, and 1275 cm^{-1} . While the peaks are relatively weak, their signal-to-noise ratios are statistically significant (see discussion in Appendix A). The peak located near 1006 cm^{-1} can be resolved by peak fitting with multiple Gaussians. Because it partially overlaps with the intense negative peak at 1048 cm^{-1} , there is considerable uncertainty in assigning a precise position in the differential spectrum; hence, it has not been used in the ensuing analyses.

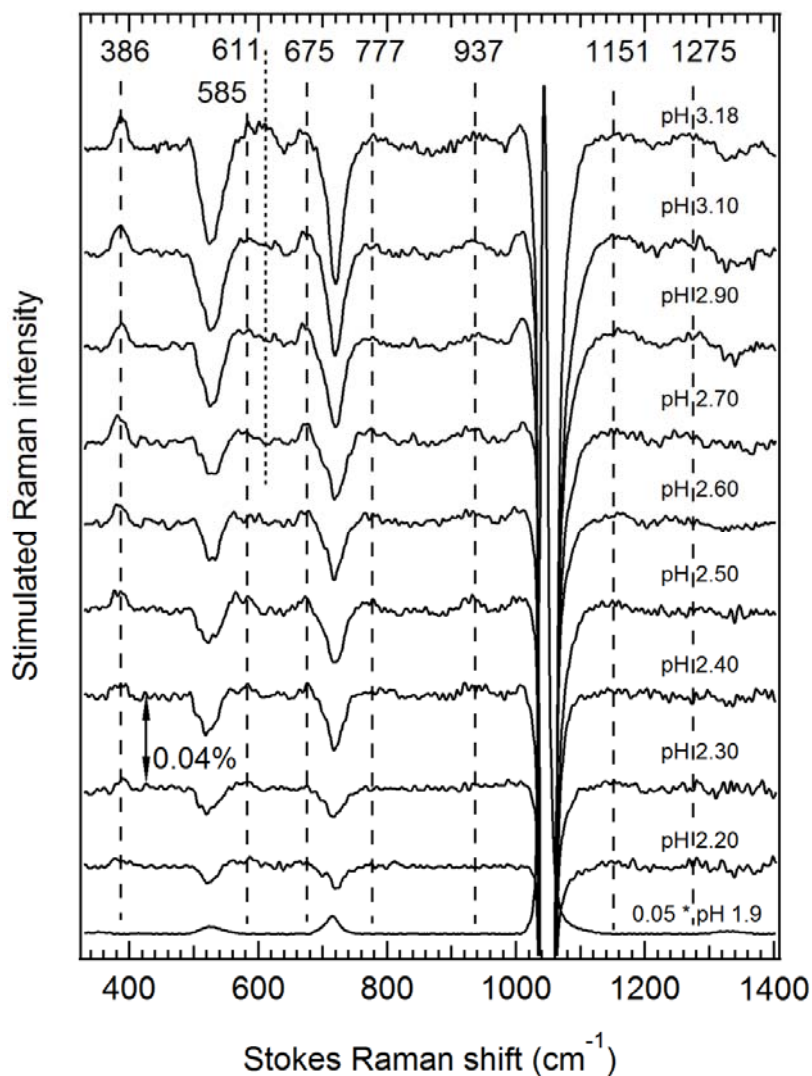


Figure 3.2. Differential FSR spectra of the cathode solution as pH increases from 1.90 to 3.18. The vertical double-headed arrow indicates a stimulated Raman gain of 0.04%. The FSR spectrum of the precursor solution (pH=1.9) is scaled by a factor of 0.05. The nascent vibrational peaks are marked by dashed lines.

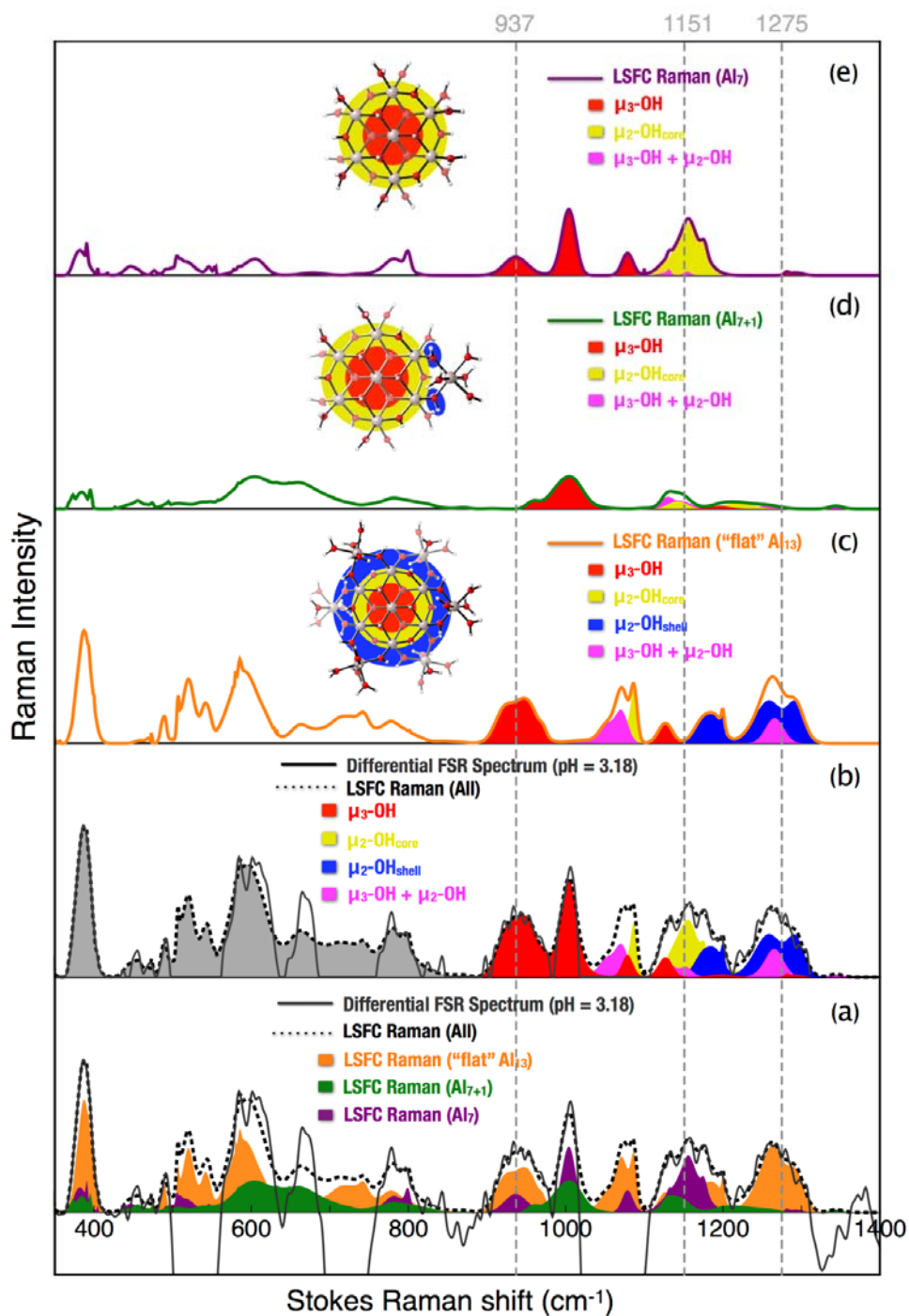


Figure 3.3. Differential FSR spectra (pH = 3.18) with contributions from (a) each cluster and (b) each hydroxyl ligand, and LSFC Raman spectrum of (c) *flat* Al₁₃ (orange), (d) Al₇₊₁ (green), and (e) Al₇ (violet).

To identify the individual Raman vibrational modes that constitute each of the peaks in the differential FSR Raman spectrum, Least-Squares Fitted Computed (LSFC) Raman spectra were created from quantum mechanically computed Raman frequencies and intensities of model cluster species.²⁶ Results for pH = 3.18 are summarized in Figure 3.3. The region 900 - 1300 cm⁻¹ exhibits resolved hydroxo-group vibrations that collectively define fingerprints for the clusters. We classify these vibrations into three types: μ_3 -OH, μ_2 -OH_{core}, and μ_2 -OH_{shell}, where the subscripts of μ denote the number of Al atoms bound to each -OH group. The Al₇ cluster [Al₇(μ_3 -OH)₆(μ_2 -OH)₆(H₂O)₁₂]⁹⁺, representing the planar core of the *flat* Al₁₃ cluster, contains a central Al atom that is bridged to six next nearest-neighbor Al atoms by μ_3 -OH groups, *cf.*, red circle in Figure 3.3e. These groups give rise to signals near 937 and 1006 cm⁻¹. The outer six Al atoms are also connected to each other by μ_2 -OH_{core} bridges, *cf.*, yellow circle in Figure 3.3e, producing bands near 1075 and 1151 cm⁻¹. The *flat* Al₁₃ clusters exhibit the Al₇ core with six additional Al atoms appended via μ_2 -OH_{shell} linkages. These groups, *cf.*, blue circle in Figure 3.3c, produce signals near 1190 and 1275 cm⁻¹. Mixed bands, comprising both μ_3 - and μ_2 -OH vibrations, are also observed for the Al₁₃ cluster near 1075 and 1270 cm⁻¹. The structural form of these hydroxo groups is replicated in the Al₇₊₁ cluster (Figure 3.3d), where one additional Al atom is appended to the Al₇ core.

Deconvolution of the total LSFC spectrum (Figure 3.3a) reveals that the solution contains the *flat* Al₁₃ cluster as well as the Al₇ species, *cf.*, Figure 3.3a, c, & e. The peaks near 1000 and 1151 cm⁻¹ provide strong evidence for the existence of Al₇; the 1151 cm⁻¹ peak is uniquely associated with the μ_2 -OH_{core} in Al₇, *cf.*, Figure 3.3e. In addition, the Al₇₊₁ species [Al₈(μ_3 -OH)₆(μ_2 -OH)₈(H₂O)₁₄]¹⁰⁺ can be added to the spectrum without negatively affecting the fit, suggesting its likely existence in the solution. The total computed spectrum, incorporating the three clusters, correlates well to the differential FSR spectrum over the entire energy range 350 - 1300 cm⁻¹ (Figure 3.3a & b). Computations reveal that Al-O vibrations dominate in the 350 -

900 cm^{-1} region. The rise in the positive signal at 386 cm^{-1} is a strong and unique indication of cluster formation with increasing pH.

To examine the formation of the cluster species, the integrated areas of the 525, 718, and 1048 cm^{-1} negative peaks and the 937, 1151 and 1275 cm^{-1} positive peaks in Figure 3.2 have been normalized and plotted against solution pH (Figure 3.4). Three distinct reaction stages are evident. In Stage I (pH = 2.20-2.45), both NO_3^- and $[\text{Al}(\text{H}_2\text{O})_6]^{3+}$ decrease in the cathode solution. The decrease of $[\text{Al}(\text{H}_2\text{O})_6]^{3+}$ is directly correlated to the formation of Al clusters (increasing 937 and 1151 cm^{-1} signals) and the concomitant decrease of the NO_3^- concentration (718 and 1048 cm^{-1}); NO_3^- migrates from the cathode to the anode compartment to maintain charge balance. As noted above, the 1151 cm^{-1} peak is uniquely associated with the $\mu_2\text{-OH}_{\text{core}}$ in Al_7 . Because no significant intensity is detected in the spectral region around 1275 cm^{-1} corresponding to the $\mu_2\text{-OH}_{\text{shell}}$ of *flat* Al_{13} , we associate this initial reaction stage with the *formation* of the Al_7 core structure.

In Stage II (pH = 2.45-2.70), the Al_7 cluster continues to dominate, but the appearance and growth of the 1275 cm^{-1} signal uniquely indicates the formation of the Al_{13} cluster. There is little change in the NO_3^- and $[\text{Al}(\text{H}_2\text{O})_6]^{3+}$ concentrations across this region, indicating a predominance of hydrolysis and condensation of Al species in response to the pH change. The continuously rising 1151 cm^{-1} signal in concert with the 1275 cm^{-1} peak is an indication that Al_7 and Al_{13} concentrations are increasing. Intermediate species such as Al_{7+n} may also be forming, but assignments here are less certain. Moreover, the Al_{7+n} structure may well be only one of a set of sequential species Al_{7+n} ($n = 1-5$) contributing to initial formation of *flat* Al_{13} .

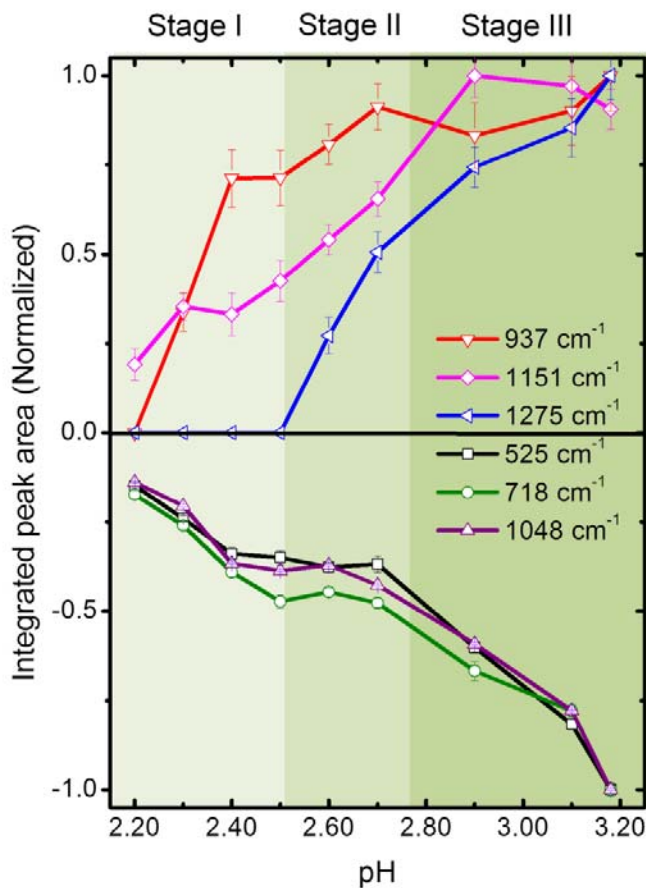


Figure 3.4. Differential FSR signal intensity vs. pH for 1.0-M $\text{Al}(\text{NO}_3)_3$ (*aq*) solution in reaction. Peak assignments for the Al clusters with reference to Figure 3.3 are 937 ($\mu_3\text{-OH}$), 1151 ($\mu_2\text{-OH}_{\text{core}}$), and 1275 cm^{-1} ($\mu_2, \mu_3\text{-OH}_{\text{shell}}$). The 525 cm^{-1} signal corresponds to Al-O vibrations in $\text{Al}(\text{H}_2\text{O})_6^{3+}$, and the signals at 718 and 1048 cm^{-1} are associated with NO_3^- .

In Stage III (pH = 2.70 - 3.18), the increasing 1275 cm^{-1} signal is consistent with a continuing shift of equilibria favoring *flat* Al_{13} . Because the 937 and 1151 cm^{-1} signals are associated with both Al_7 and Al_{13} , no significant changes are expected as the equilibrium shifts, hence the plateau in these signals. This stage also covers the pH range where crystals of *flat* Al_{13} nitrate can most readily be harvested from the cathode solution. Both the NO_3^- and $[\text{Al}(\text{H}_2\text{O})_6]^{3+}$ signals significantly decrease,

representing nitrate migration from the cathode compartment and a building of higher order Al clusters between Al₇ and Al₁₃.

Conclusions

A novel electrolysis approach for precise pH control, a newly improved FSR method for extending detection capabilities to the low-frequency domain, and advanced computational methods have been combined to uniquely map the formation of the *flat* Al₁₃ cluster at low pH. Together, the techniques provide a new and powerful toolset for study of aqueous metal speciation. Insofar as we know, the approach provides for the first time a means to establish both chemical identity and detailed molecular structure for a metal species in water. The techniques have revealed a unique snapshot of aqueous Al chemistry that extends previous studies and highly cited Al predominance diagrams.^{20,21} The single-reagent electrochemical technique for smoothly varying pH eliminates the sharp gradients that may lead to nucleation of the tetrahedral AlO₄ species at low apparent pH values, while also enabling the isolation and crystallization of *flat* Al₁₃ in a clean and efficient way. We identify a new three-stage formation pathway to the *flat* Al₁₃ cluster via an Al₇ intermediate. Because these Al clusters are quite soluble in water, they are new precursors for preparation of Al₂O₃ coatings, films, and nanoparticles of interest for electronics, catalysis, and corrosion prevention. The proposed condensation pathway, involving only octahedrally coordinated Al, is also consistent with the existence and structures of the common minerals gibbsite and boehmite, which contain Al only in distorted octahedral coordination environments.

The discoveries provide new insights concerning the nature of the equilibria and intermediates contributing to the complex condensation and speciation chemistries of Al, while raising new questions about behavior outside the narrow pH range studied here. The methods open a new chapter in the study of an important element, and they provide a unique and general approach for establishing the molecular structures of species in other aqueous metal systems.

References

1. Bohn, H.; McNeal, B.; O'Connor, G. *Soil Chemistry*, 3rd edition; John Wiley & Sons: New York, 2001.
2. Delhaize, E.; Ryan, P. R.; *Plant Physiol.* **1995**, *107*, 315.
3. Robertson, J. *Rep. Prog. Phys.* **2006**, *69*, 327.
4. Hoex, B. *et al. Appl. Phys. Lett.* **2007**, *91*, 112107.
5. Schmidt, J. *et al. Prog. Photovoltaics* **2008**, *16*, 461.
6. *Guidelines for Drinking Water Quality*, 4th edition; World Health Organization: Geneva, 2011.
7. Gensemer, R. W.; Playle, R. C. *Crit. Rev. Environ. Sci. Technol.* **1999**, *29*, 315.
8. Kablukov, I.; Sachanov, A. *Z. Physik. Chem.* **1910**, *69*, 419.
9. Heyrovsky, III, J. *J. Chem. Soc.* **1920**, *117*, 11.
10. Johansson, G. *Acta Chem. Scand.* **1962**, *16*, 403.
11. Casey, W. H.; Olmstead, M. M.; Phillips, B. L. *Inorg. Chem.* **2005**, *44*, 4888.
12. Johansson, G.; Lundgren, G.; Sillen, L. G.; Soderquist, R. *Acta Chem. Scand.* **1960**, *14*, 769.
13. Allouche, L.; Gerardin, C.; Loiseau, T.; Ferey, G.; Taulelle, F. *Angew. Chem. Int. Ed.* **2000**, *39*, 511.
14. Rowsell, J.; Nazar, L. F. *J. Amer. Chem. Soc.* **2000**, *122*, 3777.
15. Casey, W. H. *Chem. Rev.* **2006**, *106*, 1.
16. Casey, W. H.; Phillips, B. L.; Furrer, G. *Rev. Mineral. Geochem.* **2001**, *44*, 167.
17. Baes, C. F.; Mesmer, R. E. *The Hydrolysis of Cations*; Krieger Pub. Co., 1986.

18. Schweitzer, G. K.; Pesterfield, L. L. *The Aqueous Chemistry of the Elements*; Oxford University Press: USA, 2010.
19. Wang, W.; Wentz, K. M.; Hayes, S. E.; Johnson, D. W.; Keszler, D. A. *Inorg. Chem.* **2011**, *50*, 4683.
20. Gatlin, J. T.; Mensinger, Z. L.; Zakharov, L. N.; MacInnes, D.; Johnson, D. W. *Inorg. Chem.* **2008**, *47*, 1267.
21. Seichter, W.; Mogel, H. J.; Brand, P.; Salah, D. *Eur. J. Inorg. Chem.* **1988**, *6*, 795.
22. Hu, C. Z.; Liu, H. J.; Qu, J. H. *Colloid Surface A* **2005**, *260*, 109.
23. Akitt, J. W.; Farthing, A. *J. Chem. Soc. Dalton*, **1981**, 1615.
24. Rudolph, W. W.; Mason, R.; Pye, C. C. *Phys. Chem. Chem. Phys.* **2000**, *2*, 5030.
25. Liu, W. M.; Zhu, L. D.; Fang, C. *Opt. Lett.* **2012**, *37*, 3783.
26. Wang, W.; Chang, I.-Y.; Zakharov, L.; Cheong, P. H.-Y.; Keszler, D. A. *Inorg. Chem.* **2013**, *52*, 1807.
27. Roothaan, C. C. J. *Rev. Mod. Phys.* **1951**, *23*, 69.
28. Francl, M. M.; Pietro, W. J.; Hehre, W. J.; Binkley, J. S.; De-Frees, D. J.; Pople, J. A.; Gordon, M. S. *J. Chem. Phys.* **1982**, *77*, 3654.
29. Tomasi, J.; Mennucci, B.; Cammi, R. *Chem. Rev.* **2005**, *105*, 2999.
30. *Gaussian 09*, Revision B.01, Frisch, M. J. *et al.* Gaussian, Inc., Wallingford, CT, 2009.

Chapter 4: Aqueous Solution Processed Aluminum Oxide Thin-film

Dielectrics - Reaction Pathway Control from Precursor to Film

Wei Wang, Stephen T. Meyers, Rick E. Presley, John F. Wager, and Douglas
A. Keszler

To be submitted to Chemistry of Materials

Introduction

Aluminum oxide is a multi functional material, well known for its physical and chemical stability, hardness, abrasion resistance, and insulating electrical properties. It is widely used in tool coatings, optics, cutting operations, catalyst supports, and microelectronic devices.¹⁻¹² More recently, it has been investigated as a backside passivation layer for crystalline silicon solar cells because of its high built-in negative charge.¹³⁻¹⁵ In certain scenarios, aluminum oxide is also an attractive insulator for study as a gate dielectric in thin-film transistors (TFTs) and a tunneling barrier in MIM diodes. Its medium dielectric constant (~9) and wide band gap (~6.6 eV) support relatively high capacitance and low leakage current density in devices. These intrinsic properties, however, are not generally limiting factors in dielectric performance. Rather performance strongly depends on other extrinsic film properties, such as film density, defectivity, smoothness, and uniformity, i.e., long-standing challenges in thin film fabrication.

Various vacuum based techniques, such as metal-organic chemical-vapor deposition (MOCVD),¹⁶ evaporation (reactive or electron-beam),^{10,17} magnetron sputtering,^{7,18-20} and pulsed-laser deposition (PLD)^{21,22} have been used in pursuit of high-quality aluminum oxide thin films. Even with these highly advanced vacuum methods, reasonable dielectric properties were rarely observed in the resulting aluminum oxide thin films.

Atomic layer deposition (ALD), a self-limiting thin film deposition technique, has been widely used for deposition of very high quality thin films.^{23,24} Indeed, aluminum oxide is often considered to be a model ALD system because of its demonstrated film qualities.²⁵⁻²⁹ Lim and coworkers,²⁵ for example, reported a breakdown field of 4 MV/cm for conventional ALD Al₂O₃ thin film and near 9 MV·cm⁻¹ for a N₂ plasma assisted process. The leakage current densities of these films at 1-2 MV·cm⁻¹ were on the order of 1 -10 nA·cm⁻², which indicates suitability for use in a variety of devices. Low material-use efficiency and

problematic scalability to large substrate sizes, however, present challenges for all vacuum-based deposition techniques, while ALD additionally suffers from low deposition rates.

To overcome these disadvantages, solution-based thin-film deposition has been heavily investigated for more than a decade. In the case of Al_2O_3 , the majority of research has been directed to metal-organic sol-gel chemistry. Spin coating,^{30,31} dip coating,^{32,33} and spray pyrolysis^{9,34-36} are common methods of depositing and converting a precursor solution into a solid thin film. Although some aluminum oxide layers exhibit promising properties,^{34,36} they cannot fulfill the technical requirements necessary for an effective dielectric layer. Conventional metal-organic sol-gel chemistry often involves bulky organic ligands. Ideally, the bulky ligands would provide effective control of the hydrolysis and condensation of aluminum species, as water is slowly introduced to the system. Practically, it is extremely difficult to introduce at the necessary rate; therefore condensation occurs rapidly, which inevitably leads to the formation of aluminum hydroxide nanoparticles. These nanoparticles are then dispersed and stabilized by the bulky ligands. As a result, high temperatures are generally required to expel the organic ligands and sinter the nanoparticles. Unsurprisingly the resultant thin films are normally porous and quite inhomogeneous.

Thus, ***Reaction Pathway Control*** is essential for producing high-quality thin films via solution processing. In our previous contributions, we have described unique approaches for depositing high-quality oxide thin films from aqueous solution precursors, cf., $\text{HfO}_{2-x}(\text{SO}_4)_x$ (HafSOx),³⁷ $\text{Al}_2\text{O}_{3-3x}(\text{PO}_4)_{2x}$ (AlPO),³⁸ ZnO ,³⁹ TiO_2 ,⁴⁰ and HfO_2 .⁴¹ By controlling the hydrolysis and condensation of metal cations in aqueous solution, formation of large colloid particles can be avoided and thus the addition of organic stabilizing ligands and organic solvent is no longer necessary. Aqueous solutions containing nanometer-size molecular species enable the realization of continuously dense, defect-free, and atomically smooth oxide layers. These films exhibit properties comparable to thin films fabricated by

advance vacuum techniques. In this work, we apply these principles to the design of solution precursor for the deposition of high-quality Al_2O_3 films.

Aluminum exhibits a rich aqueous chemistry, especially in weakly acidic to neutral environments, where the transition from aluminum-aquo to aluminum-hydroxo/hydroxide species occurs. Various cluster structures have been proposed to exist in this pH range, and some of their structures have been established by X-ray crystallography.⁴²⁻⁴⁷ Among them, two tridecameric species are particularly interesting because of their high degree of condensation and ready synthesis. The first one is the well-known ϵ -isomer of the Baker-Figgis Keggin ion, which is characterized by a tetrahedral AlO_4 core connecting four edge-sharing distorted AlO_6 octahedra trimers via oxo bridges. The second structure is often referred to as the “flat” Al_{13} cluster. It is built on an AlO_6 center surrounded by six AlO_6 units via μ_3 -OH bridges, forming an Al_7 planar core. Six additional AlO_6 units share corners with the peripheral AlO_6 octahedra of the Al_7 core, positioning above and beneath the planar core. The Keggin Al_{13} structure is often produced by base titration of solutions containing simple aluminum salts. The isolated crystals commonly contain alkali-metal cations and anion (sulfate), both of which are difficult to remove and impart a general insolubility to the material. On the other hand, the “flat” Al_{13} can readily be isolated as pure inorganic nitrate salt that is highly soluble in polar solvents. It also readily decomposes to the oxide at relatively low temperature. Moreover, its low anion-to-metal ratio ($\text{NO}_3/\text{Al} = 15:13$) and absence of other cations leads to a low ionic strength in aqueous solution. These characteristics all make the “flat” Al_{13} nitrate salt an attractive precursor for solution deposition of aluminum oxide thin films.

In a previous contribution, we reported a simple, scalable method of synthesizing “flat” Al_{13} nitrate salts from aqueous solutions.⁴⁸ In this contribution, we examine the use of this cluster compound as an aqueous solution precursor for the deposition of high quality aluminum oxide thin films.

Experimental Methods

Precursor Synthesis

The synthesis of $[\text{Al}_{13}(\mu_3\text{-OH})_6(\mu\text{-OH})_{18}(\text{H}_2\text{O})_{24}](\text{NO}_3)_{15}\cdot n\text{H}_2\text{O}$ (“flat” Al_{13}) polycrystalline powder followed our previous work.⁴⁸ The hydration number n is determined based on the mass of Al_2O_3 produced from calcining 1 g of the powder at 800 °C for 10 h. Powders were dissolved in Millipore water ($\rho = 18.2 \text{ M}\Omega\cdot\text{cm}$) with a small amount of $\text{Al}(\text{NO}_3)_3\cdot 9\text{H}_2\text{O}$ (BAKER ANALYZED Reagent, ACS Grade) to obtain a solution precursor with an aluminum concentration from 0.1 M to 1.2 M and NO_3^-/Al ratio of 1.5:1.

Thin Film Deposition

All substrates were cleaned with a thorough Millipore water rinse followed by a low energy O_2 -plasma ash to create a clean and hydrophilic surface. Films were deposited via spin-coating at 3000 rpm for 30 s followed immediately by curing on a hot plate at 230 °C for 1 min. This step was repeated until the desired thickness was obtained. Unless otherwise specified, a solution precursor containing 0.6 M $\text{Al}^{3+}(\text{aq.})$ was used. Films were annealed in air at 250–800°C for 30–60 min to promote additional dehydration and densification. Short annealing periods (30 minutes) were used to minimize the growth interfacial SiO_2 for thin films deposited on p-type silicon, when the annealing temperature exceeded 500°C.

Chemical Characterization

Substrates comprising of a 200–nm SiO_2 top layer on an intrinsic silicon wafer were used for thin film X-ray diffraction (XRD), Fourier transform infrared (FTIR) and electron-probe microanalysis (EPMA) measurements. The XRD data were collected on a Rigaku RAPID diffractometer equipped with $\text{Cu K}\alpha$ radiation. FTIR spectra were obtained on a Nicolet 5PC spectrometer by using a bare SiO_2/Si substrate as reference; the data were obtained by averaging 1024 scans from 400 to 4500 cm^{-1} . EPMA data were collect by using a Cameca SX-50 with wavelength dispersive spectrometers and gas-flow proportional detectors with P-10 gas. Electrons were accelerated at 10, 15, and 20 kV to generate $\text{K}\alpha$ radiation from O, Si,

Al, and Zn during the measurement. MgO, SiO₂, Al₂O₃, and ZnO were used as standards, and a background correction was applied as described in detail by Donovan and Tingle.⁴⁹ Elemental compositions were then obtained by K α intensity simulation using StrataGEM thin-film composition analysis software.

Morphology and Density Characterization

Morphology and density were characterized for films deposited on boron-doped silicon (p-Si). Contact-mode atomic force microscopy (AFM) images were taken on a Digital Instruments Nanoscope III Multimode atomic force microscope with a Veeco NP-20 silicon nitride tip. A second order flatten was applied to the Z-height images to compensate for the non-linear movement of the piezoelectric motor. Scanning electron microscopy (SEM) images were collected on a ZEISS Ultra-55 microscope with 5-kV electrons; a gold layer was thermally evaporated onto the thin film surface to reduce sample charging during imaging. Scanning transmission electron microscopy (STEM), transmission electron microscopy (TEM) images, and selected area electron diffraction (SAED) images were obtained with an FEI Titan 80-300 transmission electron microscope. Samples were prepared for these imaging studies by using a FEI Helios Dual-Beam FIB. A platinum layer was deposited during the preparation to protect the thin films from electron-beam damage, and a carbon layer was thermally evaporated onto films before the deposition of Pt layer to provide contrast between layers. X-ray reflectivity (XRR) data were collected over the 2θ range 0.5 to 5.0° with a step size of 0.02° and a scan speed of 0.1°/min on a Rigaku Ultima-IV equipped with Cu K α radiation (40 kV, 40 mA). The X-ray beam is 1 mm in height and 10 mm in width. The data were modeled by Globalfit software to extract the mass density, thickness, and roughness of the aluminum oxide film.

Optical Characterization

Spectroscopic ellipsometry (SE) was adopted to measure the optical properties of the films deposited on p-Si. Spectra in the range of 300-1000 nm were collected at

three incident angles 65°, 70°, and 75°, with an HS-190 spectroscopic ellipsometer (J. A. Woolam Co., Inc.). A bare p-Si substrate, treated under the same experimental conditions as each measured sample, was used as a reference. Both the amplitude change (Ψ) and the phase change (Δ) were recorded and analyzed by using the VASE software package. A Cauchy model was used to fit the spectra to obtain the thickness and refractive index, and the difference of Ψ , Δ values between simulation and measurement is expressed by the mean square error (MSE).

Electrical Device Fabrication and Characterization

Metal-insulator-semiconductor test structures were fabricated by spin coating 100-150 nm aluminum oxide thin films onto heavily doped p-Si substrates ($\rho = 0.01 \Omega\cdot\text{cm}$). The circular Al top contact (~ 200 nm thick, 0.011 cm^2 in area) were thermally evaporated via shadow mask. A Hewlett-Packard 4192A impedance analyzer was used to measure the relative dielectric constant and loss tangent of each test device. Breakdown field strength and the leakage current density of the layer were evaluated using a Hewlett-Packard 4140B picoammeter. Bottom-gate thin-film transistors, which consist of 50 nm rf-sputtered zinc tin oxide (ZTO, Zn : Sn = 2:1) channel layer and 120 nm solution deposited Al_2O_3 dielectric layer, were fabricated on heavily doped p-Si substrates, which also acts as the TFT gate. A shadow mask was used to define the ZTO channel width (W) at $500 \mu\text{m}$. The ZTO layer and the Al_2O_3 layer were both annealed at 500°C for 1 h after the deposition. Approximately 200 nm of Al was thermally evaporated via a shadow mask, thereby defining the TFT channel length (L) at $100 \mu\text{m}$. Control devices with 100 nm thermally-grown SiO_2 gate dielectric layer were fabricated by using the same experimental protocol. All TFTs were characterized in the dark by using a Hewlett-Packard 4156C semiconductor parameter analyzer.

Results and Discussion

The solution-precursor synthesis is discussed in detail in Appendix B. For aluminum oxide thin film deposition, the reaction pathway is also carefully

controlled. “Flat” Al_{13} clusters served as the molecular species in the solution precursor with nitrate to metal ratio of 1.5:1, which is lower than the value of aluminum nitrate (3:1). Nitrate anions decompose relatively easily during mild heating of the liquid film, which leads to thermohydrolysis and homogeneous condensation of Al_{13} units and nearly uniform formation of aluminum oxide-hydroxide thin films. This approach for forming a thin film from an inorganic solution precursor is called “prompt inorganic condensation” (PIC). The PIC approach is described in Appendix C. After the PIC process, an additional anneal can fully dehydrate the film to aluminum oxide and promote densification the thin films to aluminum oxide.

Figure 4.1 shows thin-film XRD patterns of samples annealed from 300 to 800 °C for 1 h. For comparison, a simulated powder XRD pattern for gamma- Al_2O_3 is also shown.⁵⁰ Thin films annealed at temperatures lower than 700 °C exhibit amorphous morphologies with no discernable diffraction peaks. When the annealing temperature reaches 800 °C, two very weak diffraction peaks are evident, corresponding to $\gamma\text{-Al}_2\text{O}_3$. The broad and weak diffraction peaks indicate only small crystalline domains exist in the film. SAED patterns (Figure 4.2) of films annealed at 300 °C and 500 °C consist only of diffuse rings, revealing no long range order. For a sample annealed at 800 °C, the SAED pattern exhibits a strong diffraction pattern consistent with $\gamma\text{-Al}_2\text{O}_3$ (Figure 4.2(c)). The XRD and SAED measurements provide a common picture of the amorphous and crystalline nature of the films as a function of temperature. These results are distinct from those films produced by conventional sol-gel methods, where films typically crystallize below temperatures 400 or 450 °C,^{30,51} even without extended annealing.⁵² This behavior is also different from the crystallization of bulk $\text{Al}(\text{OH})_3$ and AlOOH , which converts into aluminum oxide phase at temperatures below 500 °C.⁵³ The unique crystallization behavior can be directly related to the differences in the starting materials (nitrate) and sample conditions, eg. water content, as described by Wefers and Misra.⁵³ According to Pacewska,⁵⁴ the decomposition product of aluminum

nitrate hydrate after heating at 550 °C for 1 h is X-ray amorphous aluminum oxide. The presences of nitrate ions in the precursor might help interrupt the atom rearrangement during low temperature solid-state conversion and therefore require higher temperature for crystallization. The residual Zn in thin films produced from these precursors was measured by EPMA (not shown here) to be less than 1.5 % relative to Al.

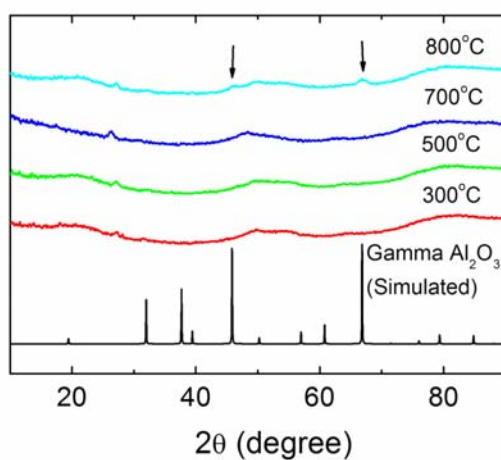


Figure 4.1. XRD pattern of aluminum oxide thin film annealed at selected temperatures.

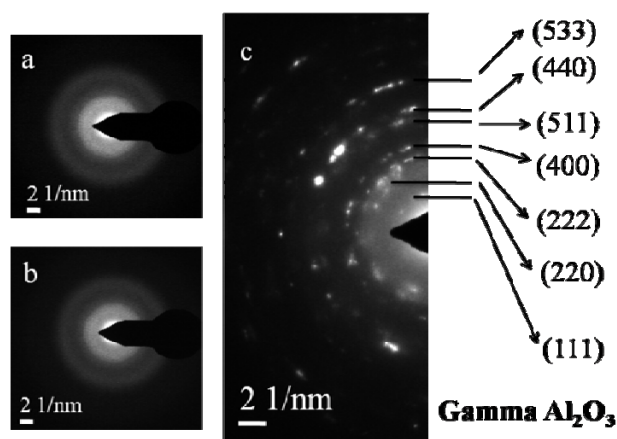


Figure 4.2. SAED of aluminum oxide thin films annealed at selected temperatures: (a) 300 °C, (b) 500 °C and (c) 800 °C.

As shown in Figure 4.3, the most evident change in the FTIR spectra is the decreasing peak intensity around 3500 cm^{-1} , which is attributed to O-H stretching vibrations associated with residual water and hydroxide in the films. The intensity drops dramatically between $250\text{ }^{\circ}\text{C}$ to $350\text{ }^{\circ}\text{C}$, revealing primary dehydration occurs at relatively low temperatures. This interpretation is also supported by the decreasing intensity of O-H bending vibration near 1500 cm^{-1} . When the annealing temperature reaches $500\text{ }^{\circ}\text{C}$, the above mentioned O-H vibration modes cannot be resolved. Features below 900 cm^{-1} are commonly attributed to superposition of various Al-O stretching vibrations.^{9,30}

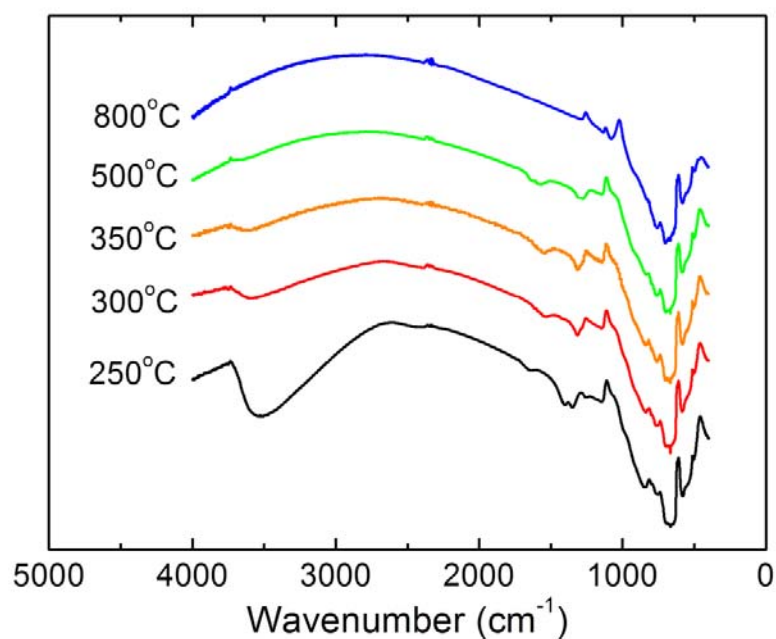


Figure 4.3. FTIR spectra of aluminum oxide films annealed at selected temperatures.

Cross-sectional SEM images of aluminum oxide thin films annealed at different temperatures are shown in Figure 4.4 (a), (b), and (c). No clear features can be resolved in the as-deposited film (Figure 4.4(a)) cured on a hot plate at $230\text{ }^{\circ}\text{C}$ for 1 min, suggesting morphological homogeneity. The amorphous nature indicates it may be considered an “inorganic polymer” resulting from cross linking of

aluminum aquo/hydroxo species upon dehydration and the loss of nitrate during the hot plate curing. According to the FTIR data, thin films without any post deposition annealing maintain a significant degree of hydration. After annealing at 500 °C (Figure 4.4(b)), film thickness decreases because of the dehydration and densification. It is noteworthy that even with the significant volume change (20% - 30%), an apparently dense and pore-free aluminum oxide thin film can still be obtained. Despite its amorphous nature, small aggregates can be resolved, which can potentially serve as centers for additional domain growth. After annealing at 800 °C, domains of γ -Al₂O₃ are observed in the film via XRD pattern, likewise small grains, i.e. 20-30 nm in diameter, can be observed in the cross-section image (Figure 4.4(c)). However, no obvious defects or voids are generated after film crystallization.

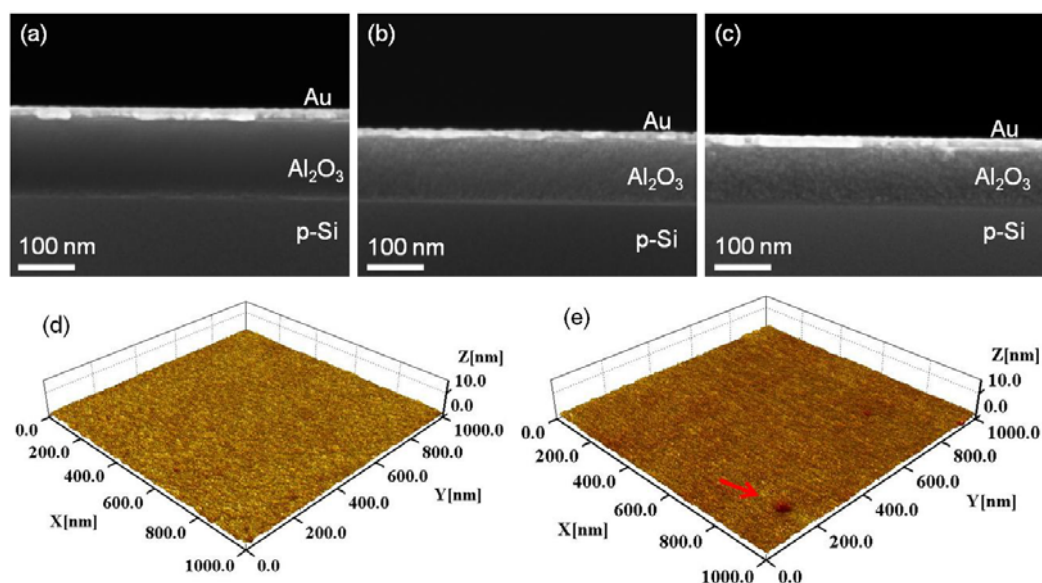


Figure 4.4. Aluminum oxide thin films annealed at selected temperatures: SEM (a) non-annealed, (b) 500 °C, and (c) 800 °C; AFM (d) 500 °C and (e) 800 °C.

Contact-mode AFM images of the films are shown in Figures 4.4(d) and (e). All of the films exhibit near atomically smooth surfaces. Films annealed at 500 °C have an RMS roughness of 0.2 nm, which corresponds to in the instrument noise level. RMS roughness of samples annealed at 800 °C was also measured to be about 0.2

nm, although some pits on the surface can be resolved (red arrow), which may associate with either local domain formation or the grain boundary on the sample surface.

STEM and HRTEM cross section images were also used to further characterize film morphology (Figure 4.5). As indicated by the images, dense, defect free and smooth aluminum oxide thin films were produced at 500 °C. The electrode diffraction pattern shows the amorphous nature of the film after a 500 °C anneal.

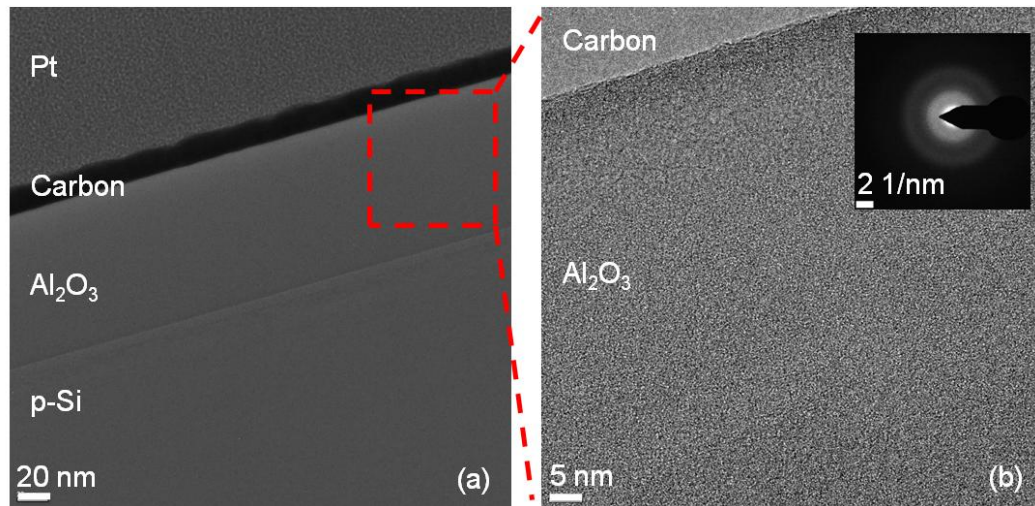


Figure 4.5. (a) STEM and (b) HRTEM cross section images of an aluminum oxide thin film annealed at 500 °C.

Optical characterization of 120-150 nm thick films was done by using spectroscopic ellipsometry (SE). Since aluminum oxide has a relatively wide band gap and is transparent throughout the measurement range, it is sufficient to model the spectra (not shown here) on the basis of the Cauchy equation with two variables A and B, according to Eq. 4.1.

$$n(\lambda) = A + \frac{B}{\lambda^2} \quad (\text{Eq. 4.1})$$

Each spectrum was successfully modeled with MSE values < 10. Dispersion curves for samples annealed at different temperature were generated from the fitting (Figure 4.6). Depending on the annealing temperature, the refractive indices vary

from 1.51 to 1.57 (at 632 nm. These values are in the range of values reported for aluminum oxide thin films prepared by conventional techniques: $n = 1.49 - 1.71$.⁵⁵ It is important to note that the refractive index reaches its highest value after annealing at 250 °C; the index then decreases rapidly to the lowest value following anneals at 300 °C to 350 °C. This behavior is explained by the loss of water, since most dehydration occurs in this temperature window. Above 350 °C, the refractive index increases as the material becomes dense.

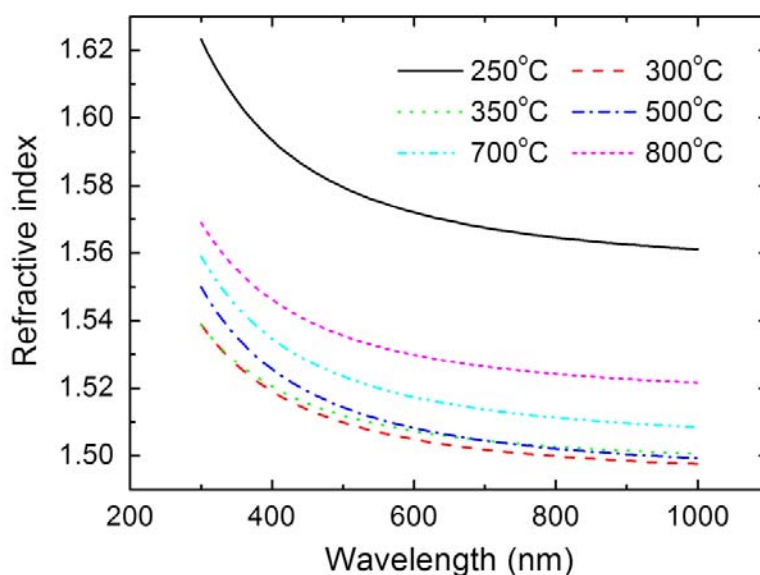


Figure 4.6. Refractive index vs. wavelength for solution deposited Al_2O_3 films annealed at different temperatures.

XRR spectra were collected and modeled to obtain the thickness, density, surface roughness. Reflectivity data for an aluminum oxide film on p-Si, annealed at 500 °C, is shown with the calculated spectrum based on the calculated model in Figure 4.7. The Kiessig fringes were found to extend to 2θ higher than 5° , which is an indication of a very smooth sample surface. Modeling the data in Figure 4.7 using Globalfit software yields a thickness of 20.4 nm, mass density of 2.56 g/cm^3 , and surface roughness of 0.272 nm. The generated density and roughness data of films annealed at different temperatures are summarized in Figure 4.8. Surface

roughness values of the measured films were 0.25 to 0.31 nm across the whole temperature range, in good agreement with the values measured by contact mode AFM.

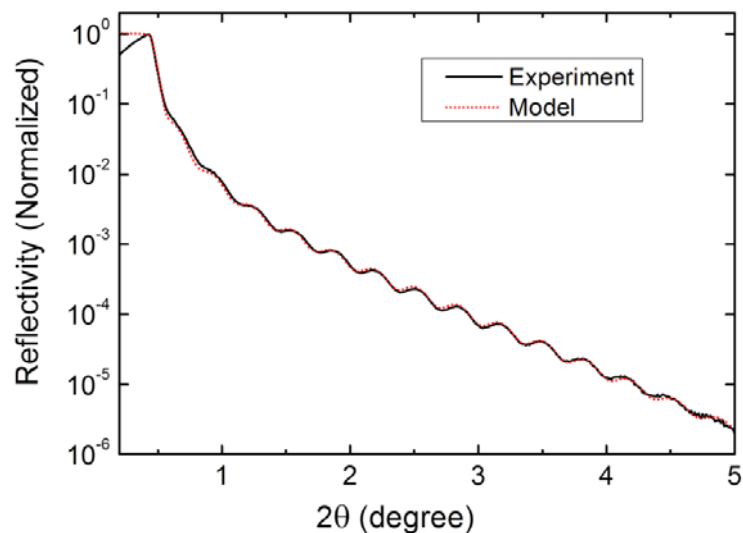


Figure 4.7. Experimental and modeled XRR spectra for a 20.4 nm film on p-Si, annealed at 500 °C.

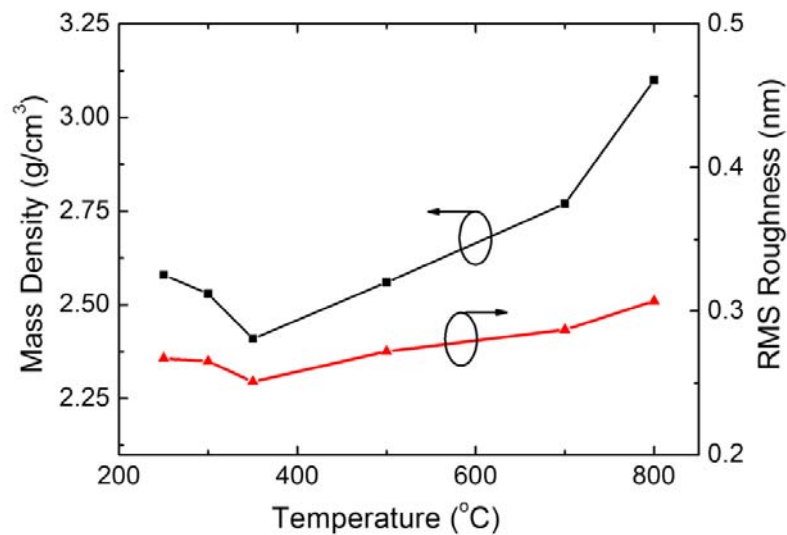


Figure 4.8. Temperature dependence of density and surface roughness examined via XRR

Since XRR spectra provide average information over several mm^2 of surface, the results reveal that the films surfaces are uniform across the substrate and are atomically smooth over a large temperature window. On the other hand, the mass density starts at 2.67 g/cm^3 for sample annealed at $250 \text{ }^\circ\text{C}$ and decreases to 2.51 g/cm^3 after the $350 \text{ }^\circ\text{C}$ anneal. This decrease in density can be attributed to the dehydration process occurring at this temperature range, since the temperature is too low to promote densification, voids will replace water after the dehydration, leading to the density decrease. The mass density increases with increasing annealing temperature because of the densification of the films, reaching 3.10 g/cm^3 after the $800 \text{ }^\circ\text{C}$ anneal. These observations are consistent with FTIR spectra and the dispersion curves generated from SE measurements. Compared to the mass density of aluminum oxide thin films deposited by other methods, these values are typically higher than sol-gel Al_2O_3 thin films at all annealing temperatures⁵⁶ but lower than ALD Al_2O_3 deposited at 300°C ($2.8\text{--}3.0 \text{ g/cm}^3$). The higher density of ALD Al_2O_3 is probably due to facile diffusion of decomposed species through the thin layers deposited during each cycle ($\sim 0.10\text{--}0.20 \text{ nm/cycle}$). The ease of diffusion of water and decomposition products during each cycle directly results in lower temperature dehydration and densification.

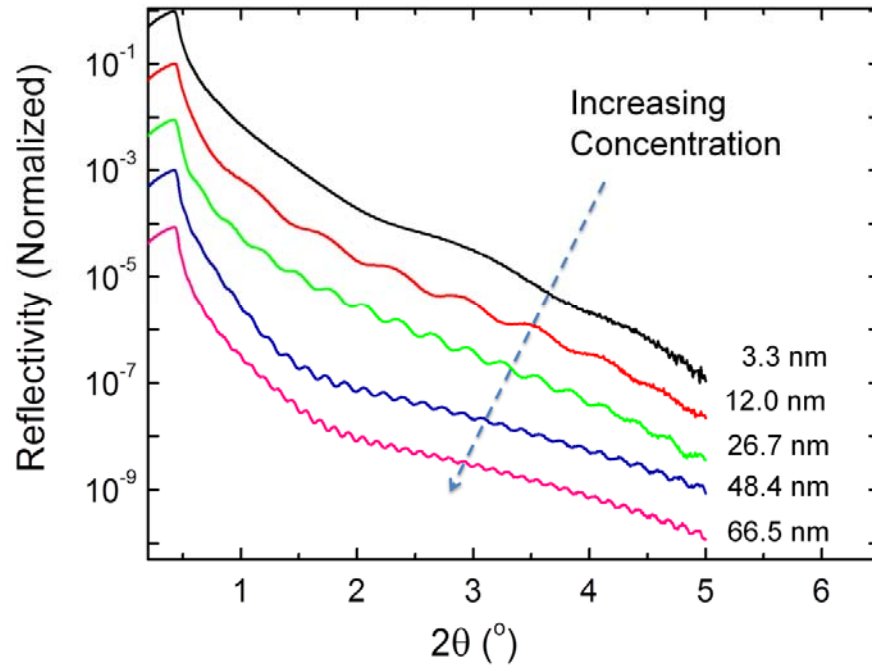


Figure 4.9. XRR spectra of un-annealed aluminum oxide films made from precursors with different metal concentration.

To realize thickness control during film deposition, both XRR and SE were used to measure the thickness of each film produced by spin coating cycle from varying precursor concentrations. XRR data of films, deposited by one spin coating cycle with solution precursors having different metal concentrations, are shown in Figure 4.9. Film thickness varies from 3.3 nm/coat (0.1 M precursor) to 68.5 nm/coat (1.2 M precursor). Although the thickness per coat is changing, thin film surfaces maintain smooth based on the extended Kisseig fringes. As demonstrated in Figure 4.10, measured data from XRR and SE are in good agreement. The plot of thickness per coat versus concentration can be fitted using a parabolic relation, which results in the following equation:

$$t = (16.27 \text{ nm} \cdot \text{L}^2 / \text{mol}^2) \cdot M^2 + (36.67 \text{ nm} \cdot \text{L} / \text{mol}) \cdot M \quad (\text{Eq. 4.2})$$

(at a relative humidity of 43-44% and environmental temperature of 18.1-18.9 °C)

Here t is the thickness (nm) and M is the molarity of the precursor solution (mol/L). The R^2 value for the fit is 0.998. As reported by Meyerhofer⁵⁷ in his study of photo resist spin coating, the mathematical relation between the thickness and initial precursor concentration can be complicated, mainly involving the viscosity change due to the solvent evaporation during the deposition process. Taking into account the dependence of water evaporation on humidity and temperature of the fabrication environment, the real relation between t and M could be more complex. During deposition of the films used in the thickness measurement shown in Figure 4.9 and 4.10, the relative humidity and environmental temperature were measured to be 43-44% and 18.1-18.9 °C, respectively. Although more systematic studies are still required, it is reasonable to believe that the thickness of the thin film can be controlled precisely in a controlled environment (eg. a clean room with humidity and temperature control). Final thicknesses of thin films after annealing were also summarized in Table 4.1. The thickness of thin film decreases about 20% after a 350 °C anneal, which is attributed to primary dehydration. Further decrease in film thickness (8-10%) after higher temperature annealing is attributed to densification, as suggested by the increasing mass density measured via XRR. With these data, the thickness of dielectric layers in MIS capacitors and TFTs can be determined for evaluation of electrical properties.

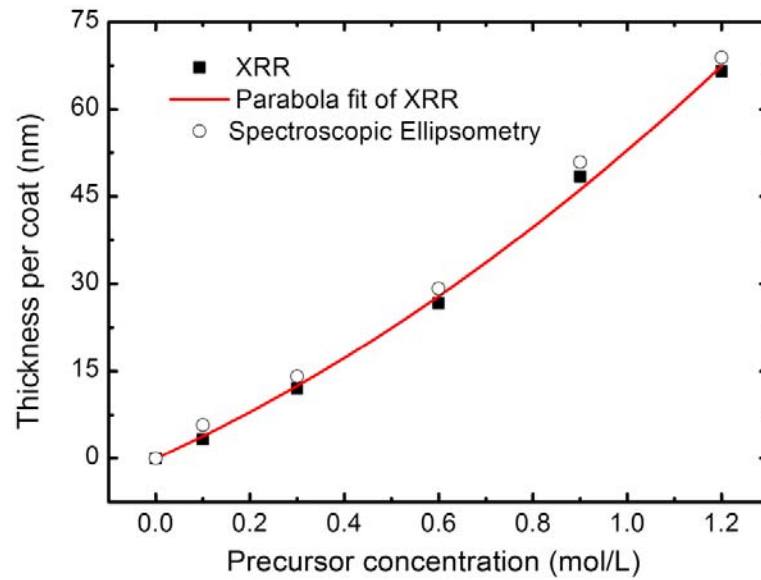


Figure 4.10. Thickness per spin coating cycle vs. precursor concentration, measured by X-ray reflectivity (XRR) and spectroscopic ellipsometry (SE). Red curve shows the parabolic fitting based on XRR data.

Table 4.1. Thin film thickness at different annealing temperatures as determined via spectroscopic ellipsometry.

Sample condition	Thickness (nm)	Thickness percentage (%)
no anneal	28.2	100.0
250 °C	26.0	92.1
300 °C	24.5	86.9
350 °C	22.7	80.5
500 °C	20.4	72.3
700 °C	19.7	69.8
800 °C	19.6	69.5

MIS capacitor test structures were fabricated containing 150 nm (initial thickness without anneal) aluminum oxide films annealed at selected temperatures. Small-signal capacitance and conductance measurements were made to determine the loss

tangent and dielectric constant in a frequency range from 10^2 to 10^6 Hz. Results are summarized in Table 4.2. Since the substrate is p-Si, the dielectric constants were corrected by removing the parallel capacitance associated with the SiO_2 generated (thickness measured by SE) after annealing at different temperature. The relative dielectric constants (ϵ_r) range from 5.6 to 7.2. The loss tangent is 2.4% for thin films annealed at 300 °C and 0.5% or lower after annealing at higher temperatures. For the sample annealed at 300 °C, the 2.4% loss tangent is presumably associated with residual water in the film, which also results in the slightly higher dielectric constant (6.0) because of the presence of polarizable hydroxo groups. The small loss tangent of films annealed at 500 °C or higher is also a good indication of the complete dehydration of the material. Current-voltage measurements were performed on the same device to evaluate the dielectric performance of the layer. A “current-limited” breakdown is defined when the leakage current density exceeds $10^{-5} \text{ A cm}^{-2}$; in these cases, catastrophic breakdown is not observed. The results are shown in Table 4.2 and Figure 4.11. All films exhibit average breakdown fields $> 4 \text{ MV}\cdot\text{cm}^{-1}$ and leakage current densities $< 10 \text{ nA}\cdot\text{cm}^{-2}$ at $1 \text{ MV}\cdot\text{cm}^{-1}$. As seen in Figure 4.11, the leakage current density is higher in 300 °C annealed samples, which behave similar to a resistor and thus catastrophic breakdown was not observed. After a 500 °C anneal, however the aluminum oxide thin films exhibit classic dielectric behavior with catastrophic breakdown. The average breakdown field reaches $5 \text{ MV}\cdot\text{cm}^{-1}$, and leakage current densities are lower than $1 \text{ nA}\cdot\text{cm}^{-2}$, which demonstrate the ability to approach the characteristics of SiO_2 (usually thermally grown at 1000°C). The solution-deposited aluminum oxide films provide similar performance at much lower processing temperate.

Table 4.2. Dielectric characteristics of aluminum oxide thin films annealed at different temperatures. An identical measurement of a MIS capacitor with 100 nm thermally grown SiO₂ dielectric layer was included as reference.

Sample condition	Dielectric Constant* @ 1kHz	Loss Tangent @ 1kHz (%)	Average Breakdown Field (MV·cm ⁻¹)	Current Density @ 1 MV/cm (nA·cm ⁻²)
300°C 1 hour	6.01	2.40	4.39	7.73
500°C 1 hour	5.68	0.51	5.10	0.94
700°C 0.5 hour	7.17	0.33	6.02	0.40
100 nm SiO ₂	3.90	0.02	8.88	0.16

* The thickness of SiO₂ were measured to be 5.5, 6.0, and 8.0 nm for 300 °C, 500 °C, and 700 °C samples, respectively.

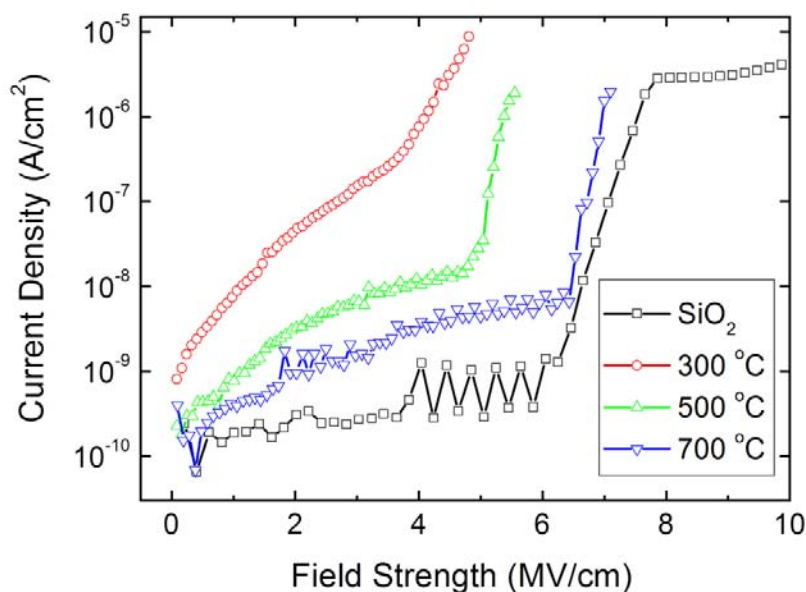


Figure 4.11. Representative current-voltage curves for films annealed at different temperatures.

Thin-film transistors were fabricated with solution-processed Al₂O₃ gate dielectrics and sputtered amorphous oxide semiconductor zinc tin oxide (ZTO, Zn :

Sn = 2:1) channel layers (~ 50 nm). TFT performance is evaluated by the turn-on voltage (V_{on}), drain current on/off ratio ($I_{on/off}$), incremental channel mobility (μ_{inc}), and subthreshold slope (S), all of which can be affected by the quality of the gate dielectric. Moreover, for evaluating a gate dielectric layer, additional attention should be paid to hysteresis in the transfer curve and the gate current (I_G), since they are likewise directly related to the gate dielectric quality.

The transfer curves and gate-current characteristics of TFTs fabricated with solution-processed Al_2O_3 and thermally grown SiO_2 are shown in Figure 4.12(a) and 4.12(b), respectively. Both devices turn on sharply near +3V and exhibit an $I_{on/off}$ value of about 10^7 . For TFTs containing Al_2O_3 dielectrics, the peak incremental channel mobility (at $V_{GS} = 30V$) is ~ 21 $cm^2/V \cdot s$, while the subthreshold swing is calculated to be 0.35 $V \cdot dec^{-1}$. These values are comparable to the control device fabricated on high quality SiO_2 dielectric layer. More importantly, I_G of the Al_2O_3 TFT remains below 1 nA even when the channel current reaches mA levels; this behavior mimics that observed with the SiO_2 dielectric layer. There is clockwise hysteresis in the Al_2O_3 TFT, slightly higher than the SiO_2 TFT. Clockwise hysteresis in TFT operation is commonly attributed to electron trapping defects located at the semiconductor-dielectric. Here, the behavior may be explained by the surface damage caused by the impinging species during the ZTO sputtering deposition process, which occurs with both dielectrics.

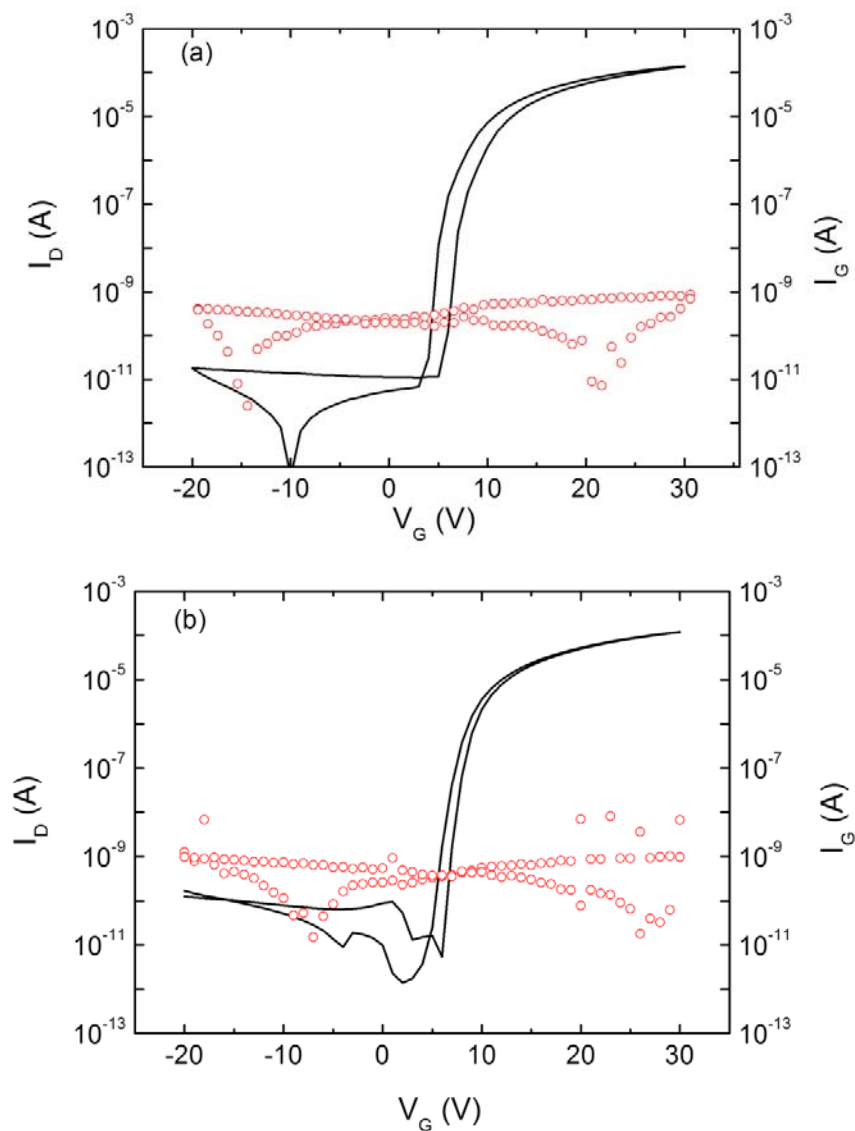


Figure 4.12. I_D - V_{GS} ($V_{DS} = 1$ V) and I_G - V_{GS} curves for TFTs with a sputtered ZTO channel layer and (a) an Al_2O_3 gate dielectric and (b) a SiO_2 gate dielectric.

Summary and Perspective

An aqueous solution precursor was developed by using a unique molecular aluminum aquo/hydroxo structure, i.e., the “flat” Al_{13} cluster. The reaction pathway was carefully controlled from the cluster synthesis to the thin-film deposition, which results in a largely defect free and atomically smooth amorphous aluminum

oxide films. The aluminum oxide thin films exhibit dielectric properties suitable for gate dielectrics in thin-film transistors.

Reference

- (1) Alvarez, N. T.; Hamilton, C. E.; Pint, C. L.; Orbaek, A.; Yao, J.; Frosinini, A. L.; Barron, A. R.; Tour, J. M.; Hauge, R. H. *Acs Appl. Mater. & Interfaces* **2010**, *2*, 1851.
- (2) Bartzsch, H.; Gloss, D.; Bocher, B.; Frach, P.; Goedicke, K. *Surf. Coat. Technol.* **2003**, *174*, 774.
- (3) Bobzin, K.; Bagcivan, N.; Immich, P.; Ewering, M. *Adv. Eng. Mater.* **2009**, *11*, 590.
- (4) Frach, P.; Bartzsch, H.; Gloss, D.; Fahland, M.; Handel, F. *Surf. Coat. Technol.* **2008**, *202*, 5680.
- (5) Fricke, S.; Friedberger, A.; Schmid, U. *Surf. Coat. Technol.* **2009**, *203*, 2830.
- (6) Li, Q.; Yu, Y. H.; Bhatia, C. S.; Marks, L. D.; Lee, S. C.; Chung, Y. W. *J. Vac. Sci. Technol. A* **2000**, *18*, 2333.
- (7) Segda, B. G.; Jacquet, M.; Besse, J. P. *Vacuum* **2001**, *62*, 27.
- (8) Segda, B. G.; Jacquet, M.; Caopera, C.; Baud, G.; Besse, J. P. *Nucl. Instrum. Methods Phys. Res. Sect. B-Beam Interact. Mater. Atoms* **2000**, *170*, 105.
- (9) Shamala, K. S.; Murthy, L. C. S.; Rao, K. N. *Mater. Sci. Eng. B-Solid State Mater. Adv. Technol.* **2004**, *106*, 269.
- (10) Shih, W. C.; Wang, T. L.; Hsu, L. L. *Thin Solid Films* **2010**, *518*, 7143.
- (11) van Hemmen, J. L.; Heil, S. B. S.; Klootwijk, J. H.; Roozeboom, F.; Hodson, C. J.; van de Sanden, M. C. M.; Kessels, W. M. M. *J. Electrochem. Soc.* **2007**, *154*, G165.
- (12) Wang, J. L.; Yu, Y. H.; Lee, S. C.; Chung, Y. W. *Surf. Coat. Technol.* **2001**, *146*, 189.

- (13) Hoex, B.; Schmidt, J.; Bock, R.; Altermatt, P. P.; van de Sanden, M. C. M.; Kessels, W. M. M. *Appl. Phys. Lett.* **2007**, *91*.
- (14) Hoex, B.; Schmidt, J.; Pohl, P.; van de Sanden, M. C. M.; Kessels, W. M. M. *J. Appl. Phys.* **2008**, *104*.
- (15) Schmidt, J.; Merkle, A.; Brendel, R.; Hoex, B.; van de Sanden, M. C. M.; Kessels, W. M. M. *Prog. Photovoltaics* **2008**, *16*, 461.
- (16) Duan, X. F.; Tran, N. H.; Roberts, N. K.; Lamb, R. N. *Thin Solid Films* **2009**, *517*, 6726.
- (17) Kobayashi, T.; Itoh, Y.; Nakano, Y.; Hirai, E.; Hashimoto, R.; Kamikawa, S. *J. Vac. Sci. Technol. A* **2006**, *24*, 939.
- (18) Kelly, P. J.; Arnell, R. D. *J. Vac. Sci. Technol. A-Vac. Surf. Films* **1999**, *17*, 945.
- (19) Udomkana, N.; Limusuwan, P. *Int. J. Mod. Phys. B* **2008**, *22*, 4217.
- (20) Voigt, M.; Sokolowski, M. *Mater. Sci. Eng. B-Solid State Mater. Adv. Technol.* **2004**, *109*, 99.
- (21) Cibert, C.; Hidalgo, H.; Champeaux, C.; Tristant, P.; Tixier, C.; Desmaison, J.; Catherinot, A. *Thin Solid Films* **2008**, *516*, 1290.
- (22) Di Fonzo, F.; Tonini, D.; Bassi, A. L.; Casari, C. S.; Beghi, M. G.; Bottani, C. E.; Gastaldi, D.; Vena, P.; Contro, R. *Appl. Phys. A-Mater. Sci. Process.* **2008**, *93*, 765.
- (23) Kim, H.; Lee, H. B. R.; Maeng, W. J. *Thin Solid Films* **2009**, *517*, 2563.
- (24) Leskela, M.; Ritala, M. *Thin Solid Films* **2002**, *409*, 138.
- (25) Lim, J. W.; Yun, S. J. *Electrochem. Solid State Lett.* **2004**, *7*, F45.
- (26) George, S. M. *Chemical Reviews* **2010**, *110*, 111.
- (27) Ghiraldelli, E.; Pelosi, C.; Gombia, E.; Frigeri, C.; Vanzetti, L.; Abdullayeva, S. *Jpn. J. Appl. Phys.* **2008**, *47*, 8174.
- (28) Zhang, X.-H.; Domercq, B.; Wang, X.; Yoo, S.; Kondo, T.; Wang, Z. L.; Kippelen, B. *Org. Electron.* **2007**, *8*, 718.

- (29) Groner, M. D.; Elam, J. W.; Fabreguette, F. H.; George, S. M. *Thin Solid Films* **2002**, *413*, 186.
- (30) Ozer, N.; Cronin, J. P.; Yao, Y. J.; Tomsia, A. P. *Sol. Energy Mater. Sol. Cells* **1999**, *59*, 355.
- (31) Vitanov, P.; Harizanova, A.; Ivanova, T.; Dimitrova, T. *Thin Solid Films* **2009**, *517*, 6327.
- (32) Zhang, W.; Liu, W.; Xue, Q. *Materials Research Bulletin* **2001**, *36*, 1903.
- (33) Vanbesien, K.; Visschere, P. D.; Smet, P. F.; Poelman, D. *Thin Solid Films* **2006**, *514*, 323.
- (34) Aguilar-Frutis, M.; Garcia, M.; Falcony, C.; Plesch, G.; Jimenez-Sandoval, S. *Thin Solid Films* **2001**, *389*, 200.
- (35) Carmona-Tellez, S.; Guzman-Mendoza, J.; Aguilar-Frutis, M.; Alarcon-Flores, G.; Garcia-Hipolito, M.; Canseco, M. A.; Falcony, C. *J. Appl. Phys.* **2008**, *103*, 034105.
- (36) Aguilar-Frutis, M.; Garcia, M.; Falcony, C. *Appl. Phys. Lett.* **1998**, *72*, 1700.
- (37) Anderson, J. T.; Munsee, C. L.; Hung, C. M.; Phung, T. M.; Herman, G. S.; Johnson, D. C.; Wager, J. F.; Keszler, D. A. *Adv. Funct. Mater.* **2007**, *17*, 2117.
- (38) Meyers, S. T.; Anderson, J. T.; Hong, D.; Hung, C. M.; Wager, J. F.; Keszler, D. A. *Chem. Mater.* **2007**, *19*, 4023.
- (39) Meyers, S. T.; Anderson, J. T.; Hung, C. M.; Thompson, J.; Wager, J. F.; Keszler, D. A. *J Am. Chem. Soc.* **2008**, *130*, 17603.
- (40) Jiang, K.; Zakutayev, A.; Stowers, J.; Anderson, M. D.; Tate, J.; McIntyre, D. H.; Johnson, D. C.; Keszler, D. A. *Solid State Sci.* **2009**, *11*, 1692.
- (41) Jiang, K.; Anderson, J. T.; Hoshino, K.; Li, D.; Wager, J. F.; Keszler, D. A. *Chem. Mat.* **2010**, *23*, 945.
- (42) Johansson, G. *Acta Chem. Scan.* **1962**, *16*, 403.

- (43) Casey, W. H.; Olmstead, M. M.; Phillips, B. L.; Phillips, L. *Inorg. Chem.* **2005**, *44*, 4888.
- (44) Johansson, G. *Acta Chem. Scand.* **1960**, *14*, 771.
- (45) Johansson, G.; Lundgren, G.; Sillen, L. G.; Soderquist, R. *Acta Chem. Scand.* **1960**, *14*, 769.
- (46) Seichter, W.; Mogel, H. J.; Brand, P.; Salah, D. *Eur. J. Inorg. Chem.* **1998**, 795.
- (47) Gatlin, J. T.; Mensinger, Z. L.; Zakharov, L. N.; MacInnes, D.; Johnson, D. W. *Inorg. Chem.* **2008**, *47*, 1267.
- (48) Wang, W.; Wentz, K. M.; Hayes, S. E.; Johnson, D. W.; Keszler, D. A. *Inorg. Chem.* **2011**, *50*, 4683.
- (49) Donovan, J. J.; Tingle, T. N. *Microscopy Microanalysis* **1996**, *2*, 1.
- (50) Zhou, R. S.; Snyder, R. L. *Acta Crystallogr. Sect. B-Struct. Commun.* **1991**, *47*, 617.
- (51) Phani, A. R.; Santucci, S. *J. Non-Cryst. Solids* **2006**, *352*, 4093.
- (52) RIAZ, S.; SHAMAILA, S.; KHAN, B.; NASEEM, S. *Surf. Rev. Lett.* **2008**, *15*, 681.
- (53) Wefers, K.; Chanakya, M. *Oxides and Hydroxides of Aluminum*, 1987.
- (54) Pacewska, B.; Keshr, M. *Thermochim. Acta* **2002**, *385*, 73.
- (55) Pulker, H. K. *Coatings on Glass*; Elsevier: Amsterdam, 1984.
- (56) Gutmann, E.; Meyer, D. C.; Levin, A. A.; Paufler, P. *Appl. Phys. A: Mater. Sci. Proc.* **2005**, *81*, 249.
- (57) Meyerhofer, D. *J. Appl. Phys.* **1978**, *49*, 3993.

Chapter 5: Chemically Enhanced Thermal Dehydration of Thin-film Oxides

Jeremy T. Anderson, Wei Wang, Kai Jiang, Torgny Gustafsson, Can Xu, Eric L.
Gafunkel, and Douglas A. Keszler

To be submitted to Nature Materials

Introductory Paragraph

Dehydration of oxides is essential to many materials functionalities, such as catalytic support, optical coatings, and semiconducting/dielectric thin films. The hydration level profoundly influences most properties as consequences of specific surface, bulk, and interface rearrangement. As thin films, oxides are especially sensitive to water, so films deposited from solutions typically require intensive post-deposition treatments. High temperature anneals are frequently incompatible with material integrations, whereas mild temperatures leave extensive hydrogen (collectively as water and hydroxide) in the film, affecting electronic and optical properties. To overcome this thermal dilemma, we here demonstrate a specific material pairing strategy through the enhanced thermal dehydration of aluminum oxide phosphate (AlPO) thin films by application of a thin HfO₂ layer. The addition of HfO₂ effectively decreases the thermal dehydration requirement of AlPO by about 250° C.

Main Text

Oxide thin films, whether vapor- or solution-deposited, often contain hydrogen in the form of hydroxide or water. Incidental hydrogen is known to compromise thin film electronic devices. In dielectrics, this hydration can give rise to defect trap states and mobile charge, lower breakdown field strength, and more, all of which create device instabilities and poor performance.¹⁻³ Relatively limited information suggesting chemical routes to the dehydration and transformation of inorganic hydroxides/hydrates to oxides is available; the most common methods for eliminating hydrogen/water from thin-film oxides are heating by optical, microwave, or conventional thermal methods.

Meanwhile, dehydration and water migration in oxides have long been significant research topics in the geological and geochemistry communities, as water plays a crucial role in a variety of geological phenomena.⁴⁻⁶ Mineral dehydration has been studied by both experimental and computational methods.^{5,7,8} Small-particle

powder, associated with higher surface area, exhibits faster dehydration than large-particle powder of the same material.⁹ It is generally opined that *bulk* diffusion processes of hydrogen (either via -OH or H₂O) control the dehydration times across a very substantial temperature range.^{10,11} While this explanation correlates small-particles with shorter diffusion length, one could likewise correlate with a higher ratio of near surface atoms – that undergo local rearrangements. For many materials, diffusion of hydrogen *through this surface* may be the rate limiting process for dehydration.

In this contribution, we study dehydration in a new way by examining the properties of a thin-film dielectric material Al(PO₄)_{0.6}O_{0.6}(H₂O)_y, or “AlPO”. As an amorphous oxide insulator, AlPO has been incorporated into a number of high-performance thin-film transistors (TFT) via aqueous processing.^{12,13} We have found that the films must be heated above 600 °C to force dehydration and eliminate the mobile protons that cause unstable TFT operation. Here, we suggest that this dehydration temperature is largely dictated by rearrangements and densification near the surface of the film as it is heated. A considerable quantity of water (and associated ions) becomes physically trapped in the bulk of the film. High temperatures are then required to promote diffusion and water loss across this surface “crust”. We hypothesize that an appropriate very thin layer of a material having a lower dehydration temperature could be used to inhibit the densification and drying of AlPO in the near-surface region, thereby facilitating continuous water loss at relatively low temperature. For the top thin layer, we have chosen solution-deposited HfO₂ films.¹⁴ In the following we demonstrate that this material combination effectively decreases the dehydration temperature of AlPO, manifesting dramatically in the dielectric behavior.

A simple C–V measurement of a metal-insulator-metal (MIM) capacitor can reveal both the capacitance (C_i) and the mobile charge level in the insulating oxide layer (Figure 5.1(a)). The mobile charges in the oxide move in response to the

external field. Charge diffusion contributes to the capacitance, and produces hysteresis on the C-V curve. Using pre-DC-bias capacitance (C_0) as reference, the relative capacitance change is plotted against the applied field in Figure 5.1(b). For films previously heated for one hour at 350 °C, the device with a simple AlPO insulator (about 200 nm) exhibits a 22,000 ppm capacitance increase at ± 1.5 MV/cm applied DC field. The hysteresis of the C-V curve is pronounced (with the zero-bias capacitance increasing approximately 7,000 ppm after the measurement). This large device instability indicates the presence of sluggish mobile charges in the AlPO layer, most likely the result of residual protons (including hydroxide)¹². However, if annealed under the same conditions but with a HfO₂ thin film (about 20 nm) deposited on the AlPO, MIM devices show about 5,000 ppm of capacitance increase at ± 1.5 MV/cm and almost no hysteresis (<200 ppm change in zero-bias capacitance). Our interpretation of this surprisingly positive result is that the HfO₂ layer enables the removal of mobile protons from the oxide layer (under the same annealing conditions) without forming a diffusion blocking layer in the AlPO. Moreover, shown in Figure D.1, the dehydration enhancement of the HfO₂ layer occurs with just a 5-minute anneal at 350 °C; a similar (but less electrically ideal) dehydration can only be achieved by annealing the AlPO layer to greater than 500 °C for one hour.

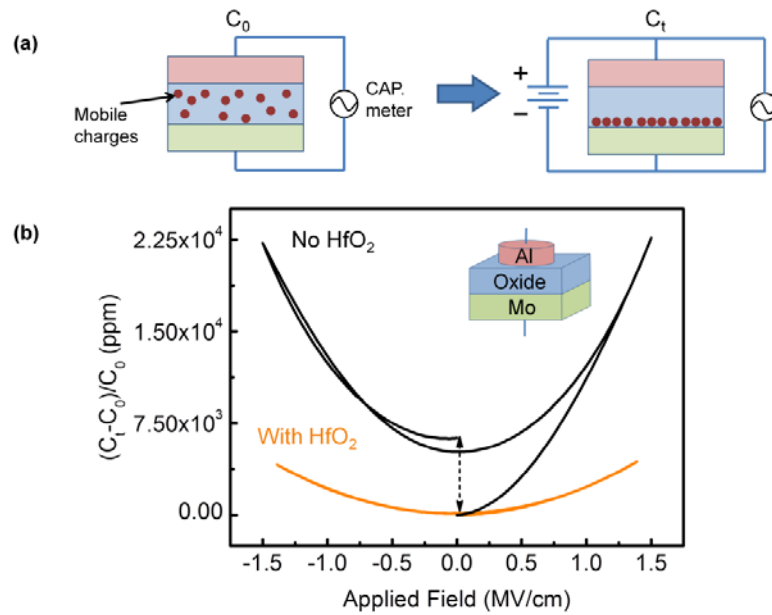


Figure 5.1 (a) A typically C–V measurement setup for an MIM capacitor; (b) One sweep cycle of MIM capacitors with an AlPO insulator (black) and a HfO₂-AlPO insulator (orange). Both insulating oxide layers were annealed at 350 °C for one hour.

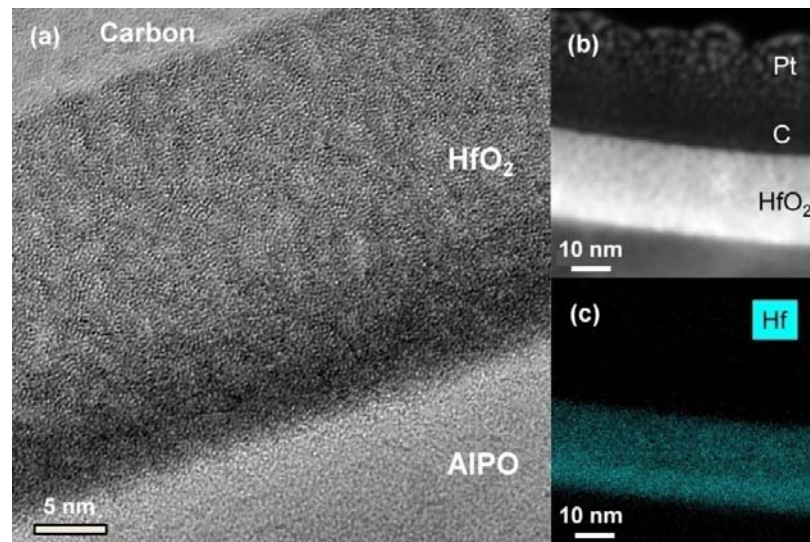


Figure 5.2 (a) High resolution TEM image of the HfO₂-AlPO interface region in HfO₂-AlPO stack after annealed at 350 °C for one hour; (b) Z-contrast STEM image showing the interface region; (c) ChemiSTEM Hf elemental mapping at the same position of image (b).

To reveal film structure, the HRTEM image of the HfO₂-AlPO interface after a one-hour anneal at 350 °C is shown in Figure 5.2(a). In the HRTEM images, such as in Figure 5.2(a), areas with higher density appear to be darker than lower density regions (for amorphous materials). After anneal, the stack exhibits different density regions in the first 15 nm of HfO₂ near the HfO₂-AlPO interface. Starting from the high density region (the darker interface layer in Figure 5.2(a)), the HfO₂ layer gradually transitions into a more porous and less dense upper portion. Low density pockets (pores) are homogeneously distributed throughout the rest of the upper HfO₂ layer. A similar conclusion can be obtained by examining Figure 5.2(b) – the STEM of the HfO₂-AlPO interface. In contrast to the HRTEM image, areas with higher atomic number Z (usually higher density) are brighter in the STEM image. The high density HfO₂ interface layer and its porous upper region become more clearly resolved in Figure 5.2(b). Figure 5.2(c) shows the Hf elemental distribution across the interface region, confirming the dark interface layer as a concentration of Hf atoms. The same HfO₂ structure can be observed after a 5-minute anneal at 350 °C, shown in Figure D.2.

We have also employed medium energy ion scattering (MEIS) to examine the films. MEIS, a high resolution variant of Rutherford backscattering spectroscopy (Figure 5.3(a)), is very useful for ultrathin film compositional depth profiling.¹⁵ In this study, MEIS was used to determine the total areal density (atoms/cm²) of Hf in HfO₂/Si and HfO₂/AlPO/Si films, to approximate the film thickness and depth profile, and to see if there is significant interdiffusion at the HfO₂/AlPO interface. In brief, we find films with the expected areal density (Y), thickness (Z) and depth profile in the HfO₂ region. The low energy edge of the ion spectra yields information about the uniformity of the film. If the film is rough at the outer surface or inner interface, or if there is interdiffusion across the interface, then the low energy tail will broaden, sometimes significantly. Because the HfO₂/SiO₂ and HfO₂/Si interface is rather sharp (based on ALD HfO₂ on SiO₂), we used the solution HfO₂ on silicon to compare with our HfO₂/AlPO/Si heterostructure.

Shown in Figure 5.3(b), because there is no noticeable broadening of the tail of the Hf peak in the HfO_2/AlPO structure relative to that in the $\text{HfO}_2/\text{SiO}_2/\text{Si}$ structure, we can say with reasonable confidence that we have no evidence for interdiffusion between HfO_2 and AlPO (beyond perhaps a few Å).

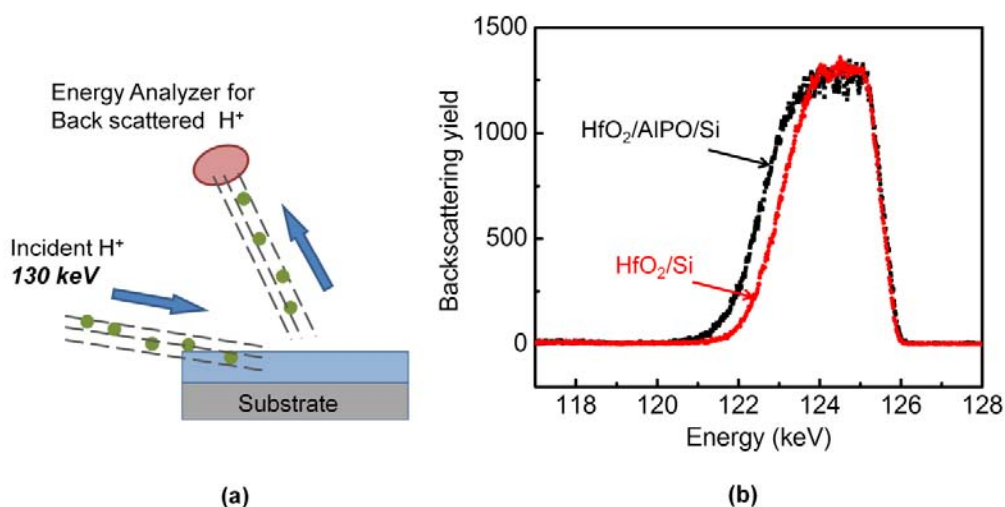


Figure 5.3 (a) Typical MEIS geometry (b) MEIS spectra of HfO_2 thin film on silicon and HfO_2 -AlPO stack on silicon substrate.

Finally, to quantify the hydrogen level in the AlPO layer, hydrogen forward scattering (HFS) measurements were performed on both AlPO and HfO_2 -AlPO samples. Figure 5.4(a) shows the typical HFS geometry and the resulted hydrogen atomic percentage in AlPO and HfO_2 -AlPO after different annealing treatments. In HFS measurements, a He^{2+} ion beam is directed onto a material at a shallow angle and interacts with the atoms in the film. Because hydrogen is the only element lighter than helium, some fraction of the hydrogen atoms will be forward scattered and can be analyzed via modeling (He^+ cannot backscatter as in “normal” RBS). Shown in Figure 5.4(b), without the HfO_2 surface layer, the AlPO thin film contains 22.7 at. % hydrogen after a one-hour anneal at 350 °C. Annealing at 600 °C for one hour decreases the hydrogen content to 4.0 at. %. On the other hand, when HfO_2 surface layer is present, the hydrogen content in the AlPO layer

dropped significantly to 4.8 at. % after a 350 °C anneal, which is almost comparable to the 600 °C annealed bare AlPO layer. Although there is still hydrogen in the HfO₂-AlPO stack, they are likely bonded tightly within the amorphous network, electronically inactive and thus not detected by the C–V measurement.

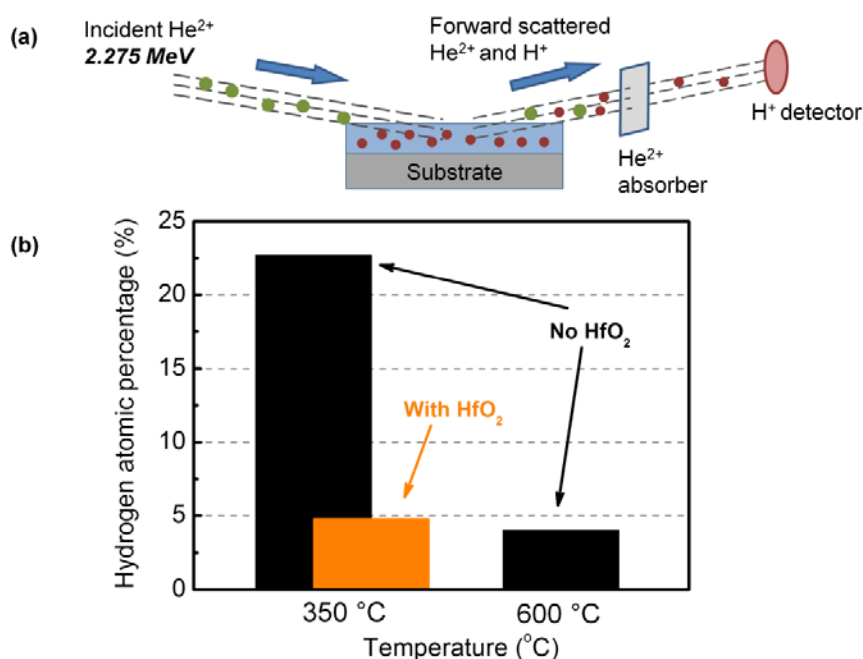


Figure 5.4 (a) typically HFS geometry; (b) hydrogen atomic percentages in AlPO layer annealed at 350 °C and 600 °C for one hour without HfO₂ (black), and annealed at 350 °C for one hour with HfO₂ (orange).

Both C–V measurement and HFS results indicate the dehydration of AlPO at 350 °C is enhanced significantly by the application of a thin HfO₂ surface layer. Based on our previous study, bare AlPO thin films lose most of the residual water after annealing at 500 – 600 °C for one hour (consistent with the HFS result), while the HfO₂ overlayer allows similar dehydration after annealing at 350 °C (certainly complete dehydration of the electrically deleterious hydrogen).^{12,14} It is clear that a reduced dehydration temperature can be achieved by replacing the surface of a hard-to-dehydrate material (AlPO) with a chemically complementary material

(HfO₂) that readily dehydrates at mild temperature.¹⁴ The temperature reduction (to obtain a similar level of dehydration) is as much as 250 °C for the material system studied here. Using X-ray reflectivity method (Figure S3 and S4), we detected a highly dense surface “crust” on top of the AlPO layer after 350 °C anneal, potentially blocking the hydrogen migration through the AlPO-air interface. Therefore, the change in AlPO dehydration behavior in HfO₂-AlPO stacks is likely caused by the interesting HfO₂ interface chemistries. Our previous study¹⁴ showed that annealing the HfO₂ layer at 350 °C allows hydrogen to transfer across the interface with achievement of ~82% density (compared to crystalline HfO₂). The HfO₂ interface region leads to a good connection between HfO₂ and AlPO film layers while creating a continuous path for hydrogen to transfer across this interface. The top porous region, on the other hand, may contribute to migration by drawing water from the denser interface. Or the porosity may be unnecessary for water transport, occurring as a consequence of rapid water expulsion.

A daily-life example provides us with an analogy on how surface and bulk materials properties, and their response to water, can differ and change with temperature. Developed 10,000 years ago, bread-baking is an essential food production activity for humanity – almost symbolic of a healthy life. Originating from the same dough, the bread crust is dry and crisp while the center can remain moist and soft. In spite of all the complex chemical changes that occur during bread baking, it is well known that crust formation and properties significantly affect the overall bread quality, including the water loss during baking.^{16,17} Methods, such as the introduction of steam while baking, have been used to control the crust characteristics in order to improve bread quality.¹⁶⁻¹⁹ Interestingly, this “steam baking” method has also been explored for the dehydration of oxide semiconductors²⁰. Here, instead of tuning the intrinsic oxide “crust”, we substitute the surface material and therefore alter the dehydration speed and properties of the underlying material.

In conclusion, we study the dehydration of AlPO thin films with and without a thin HfO₂ surface layer. On the basis of chemical compatibility and water mobility, the HfO₂ layer prevents the formation of a surface barrier that would otherwise form at the AlPO/air interface. Consequently, a mild 350 °C anneal causes dehydration comparable to nearly 600 °C for singular AlPO films. The HfO₂-coated AlPO structure is also a more ideal dielectric. These observations inform a possible new strategy to the design and exploration of low temperature material dehydration. Also, it suggests that more consideration needs to be given to the surface properties of solid materials during the study of their hydration/dehydration.

Methods

Solution Precursor Synthesis and Thin-film Deposition

AlPO (nitrate based) solution at 0.9 M, and peroxide-containing HfO₂ precursor at 0.2 M, were synthesized following the same procedure described in Ref. 12 and Ref. 14, respectively. The aluminum to phosphorus ratio in the AlPO solution is 1:0.6.

Prior to thin film deposition, all substrates were treated with a thorough Millipore water rinse followed by a low energy O₂ plasma ash to create a clean and hydrophilic surface. Films were deposited via spin-coating the aqueous precursors at 3000 rpm for 30 seconds and cured immediately on a hot plate at 230 °C for 1 min. This step was repeated until the desired layer or stack structure was obtained. Typically, a 0.9 M AlPO solution precursor resulted in a about 90-nm of baked film, while a 0.2 M HfO₂ solution precursor leads to about 8 nm. Films were further annealed in air at 350–600 °C for 5–60 minutes.

Metal-insulator-metal (MIM) Capacitor Characterization

Corning 1737 glass with 200 nm sputtered Mo was used as the substrate for fabricating MIM capacitors. AlPO films (~180 nm) were deposited with and

without the HfO₂ (~24 nm) top layer, followed by the annealing step. Circular Al top contacts (~200 nm thick, 0.011 cm² in area) were thermally evaporated via shadow mask. Capacitance voltage (*C-V*) measurements (100 kHz) were performed on an Agilent E4980A *LCR* meter, where the DC voltage range was selected according to the oxide thickness in order to obtain similar electrical field strength (1.5 MV/cm) across the oxide layer. The change of capacitance under applied DC bias, and the resulting hysteresis after returning to 0 V were monitored. *C-V* measurement results could be repeated after a suitable settling time, so were not a product of labile fabrication defects. Also beginning the field sweep cycles in the negative direction produced approximate mirror image responses.

Thin-film Characterizations

A HfO₂-AlPO stack containing ~24 nm HfO₂ and ~180 nm AlPO were also studied by TEM and STEM. Sample preparation was done using a FEI Helios Dual-Beam FIB. A platinum layer was deposited during the preparation to protect the thin film from electron-beam damage and a carbon layer was thermally evaporated onto films before the deposition of Pt layer to provide contrast between layers. p-Si was used as the substrate for all TEM studies. High resolution transmission electron microscopy (HRTEM) images, and selected area electron diffraction (SAED) images were taken on a FEI Titan 80-300 transmission electron microscope at Camcor, Oregon. 300 kV electron beam was used during TEM imaging. Scanning tunneling electron microscopy (STEM) and ChemiSTEM elemental analysis was done on a FEI Titan 80-200 transmission electron microscope at the Electron Microscopy Facility at Oregon State University. 200 kV electron beam was used during STEM imaging.

Medium energy ions scattering (MEIS) was performed at the Rutgers ion scattering facility using 130 keV protons. Additional details about MEIS methods can be found in reference 15.

Hydrogen forwards scattering measurements (Elastic Recoil Detection Analysis for hydrogen) were done by Evans Analytical Group on both AlPO thin film and HfO₂-AlPO stack. Hydrogen content at the AlPO layer was analyzed by modeling the scattering spectra. All films were deposited on p-Si substrates for the HFS measurements. The results were modeled in order to obtain hydrogen level of the AlPO layer in each sample, which is a direct indication of the residual water level in AlPO.

References

- 1 Ip, K. *et al.* Hydrogen incorporation and diffusivity in plasma-exposed bulk ZnO. *Appl. Phys. Lett.* **82**, 385-387, doi:10.1063/1.1539927 (2003).
- 2 Fleetwood, D. M. *et al.* Effects of interface traps and border traps on MOS postirradiation annealing response. *IEEE Trans. Nucl. Sci.* **42**, 1698-1707, doi:10.1109/23.488768 (1995).
- 3 Onishi, K. *et al.* Bias-temperature instabilities of polysilicon gate HfO₂ MOSFETs. *IEEE Trans. Electron Devices* **50**, 1517-1524, doi:10.1109/ted.2003.813522 (2003).
- 4 Harlov, D. E., Johansson, L., Van Den Kerkhof, A. & Forster, H. J. The role of advective fluid flow and diffusion during localized, solid-state dehydration: Sondrum Stenhuggeriet, Halmstad, SW Sweden. *J. Petrol.* **47**, 3-33 (2006).
- 5 Bray, H. J. & Redfern, S. A. T. Kinetics of dehydration of Camontmorillonite. *Phys. Chem. Miner.* **26**, 591-600, doi:10.1007/s002690050223 (1999).
- 6 Cheng, H. F. *et al.* Mechanism of dehydroxylation temperature decrease and high temperature phase transition of coal-bearing strata kaolinite intercalated by potassium acetate. *J. Colloid Interface Sci.* **376**, 47-56, doi:10.1016/j.jcis.2012.02.065 (2012).
- 7 Wright, K. Atomistic models of OH defects in nominally anhydrous minerals. *Water in Nominally Anhydrous Minerals* **62**, 67-83, doi:10.2138/rmg.2006.62.4 (2006).

- 8 Madejová, J. FTIR techniques in clay mineral studies. *Vibrational Spectroscopy* **31**, 1-10, doi:[http://dx.doi.org/10.1016/S0924-2031\(02\)00065-6](http://dx.doi.org/10.1016/S0924-2031(02)00065-6) (2003).
- 9 Alizadehhesari, K., Golding, S. D. & Bhatia, S. K. Kinetics of the Dehydroxylation of Serpentine. *Energy Fuels* **26**, 783-790, doi:10.1021/ef201360b (2012).
- 10 Zhang, M., Redfern, S. A. T., Salje, E. K. H., Carpenter, M. A. & Wang, L. H₂O and the dehydroxylation of phyllosilicates: An infrared spectroscopic study. *Am. Miner.* **95**, 1686-1693, doi:10.2138/am.2010.3561 (2010).
- 11 Kristof, J., Vassanyi, I., Nemezc, E. & Inczedy, J. Study of the dehydroxylation of clay-minerals using continuous selective water detector. *Thermochim. Acta* **93**, 625-628, doi:10.1016/0040-6031(85)85157-1 (1985).
- 12 Meyers, S. T. *et al.* Solution-Processed Aluminum Oxide Phosphate Thin-Film Dielectrics. *Chem. Mater.* **19**, 4023-4029 (2007).
- 13 Jiang, K., Meyers, S. T., Anderson, M. D., Johnson, D. C. & Keszler, D. A. Functional Ultrathin Films and Nanolaminates from Aqueous Solutions. *Chem. Mat.* **25**, 210-214, doi:10.1021/cm303268p (2013).
- 14 Jiang, K. *et al.* Low-Energy Path to Dense HfO₂ Thin Films with Aqueous Precursor. *Chem. Mat.* **23**, 945-952, doi:10.1021/cm102082j (2011).
- 15 Lee, H. D. *et al.* Reduction of native oxides on GaAs during atomic layer growth of Al₂O₃. *Appl. Phys. Lett.* **94**, doi:22210810.1063/1.3148723 (2009).
- 16 Vanin, F. M., Lucas, T. & Trystram, G. Crust formation and its role during bread baking. *Trends Food Sci. Technol.* **20**, 333-343, doi:10.1016/j.tifs.2009.04.001 (2009).
- 17 Mondal, A. & Datta, A. K. Bread baking - A review. *J. Food Eng.* **86**, 465-474, doi:10.1016/j.jfoodeng.2007.11.014 (2008).
- 18 Altamirano-Fortoul, R., Le-Bail, A., Chevallier, S. & Rosell, C. M. Effect of the amount of steam during baking on bread crust features and water diffusion. *J. Food Eng.* **108**, 128-134, doi:<http://dx.doi.org/10.1016/j.jfoodeng.2011.07.015> (2012).
- 19 Le-bail, A. *et al.* Influence of the amount of steaming during baking on the kinetic of heating and on selected quality attributes of bread. *J. Food Eng.*

- 105**, 379-385, doi:<http://dx.doi.org/10.1016/j.jfoodeng.2011.03.001> (2011).
- 20 Banger, K. K. *et al.* Low-temperature, high-performance solution-processed metal oxide thin-film transistors formed by a 'sol-gel on chip' process. *Nat. Mater.* **10**, 45-50, doi:10.1038/nmat2914 (2011).

Conclusion

The dissertation focuses on synthesis and characterization of aqueous solution and solid state materials containing aluminum. By carefully designed and control the chemical reaction pathway, unique products (eg. rare aluminum aqueous cluster, dense and defect-free aluminum oxide thin film, and low temperature dehydratable aluminum phosphate oxide thin films) can be synthesized.

Conventionally, base titration has been used to provide excess -OH to react with (in another word, consume) the proton and raise the solution pH. The highly basic environment near the base droplet changes the aluminum coordination and leads to the more commonly seen products. In chapter 2, zinc metal powder reacts with the proton and increases the solution pH. This avoids the formation of highly basic local environment and therefore changes the condensation pathway of aluminum aqueous species, making the synthesis of rare “flat” Al_{13} clusters easily achievable in aqueous environment without the need of organic stabilizing agent. The pure inorganic synthesis exhibits a yield of 55% without optimization.

In Chapter 3, the aqueous aluminum condensation pathway designed in Chapter 2 is further exploited to create a reagent-less electrolytic synthesis of “flat” Al_{13} cluster. Electrons are used to consume the proton and increase the solution pH instead of a chemical reagent. The electrolytic synthesis also enables the precise solution pH control, which allows the speciation study of aluminum aqueous solution via Femtosecond Stimulated Raman Spectroscopy (FSRS). Based on the spectroscopic data, a three-stage formation mechanism of “flat” Al_{13} has been proposed.

In chapter 4, an aqueous solution precursor was developed by utilizing a polycrystalline nitrate salt containing the “flat” Al_{13} cluster. This change from the conventional sol-gel solution precursor leads to a different solution to solid conversion pathway, resulting in defect-free and atomically smooth amorphous aluminum oxide films. The films are characterized chemically, morphologically,

and electrically. The produced aluminum oxide thin films exhibit decent dielectric properties and thus are suitable for gate dielectrics in thin film transistors.

Finally, in chapter 5, we study the dehydration of AlPO thin films with and without a thin HfO₂ surface layer. A surface limited dehydration pathway has been proposed. It can be altered by applying a HfO₂ surface layer, which decreases the dehydration temperature of AlPO effectively by as much as 250 °C, achieving a dehydration level analogous to a 600 °C annealed thin film (of pure AlPO) after a mild 350 °C anneal. These observations provide a possible new strategy to the design and exploration of low temperature material dehydration. Also, it suggests that more consideration needs to be put on the surface properties of a solid material during the study of the solid dehydration properties.

Above are just some examples on how we can produce materials that are either hard to make or with distinct properties through carefully design and control the chemical reaction pathway. The research shown here is merely a start. With all these knowledge, what is done now everyday in expensive research facilities may become achievable with the kitchen gears mentioned in Introduction. Certainly, there will be lots of challenges on the way. However, if there are enough people like you who are interested (I assume you are since you've made it all the way here to the end☺) and willing to devote to this field, I believe things can be different. After all, it is just another “distinct product” waiting for us to discover its pathway, right?

Bibliography

- Aguilar-Frutis, M.; Garcia, M.; Falcony, C. *Appl. Phys. Lett.* 1998, 72, 1700.
- Aguilar-Frutis, M.; Garcia, M.; Falcony, C.; Plesch, G.; Jimenez-Sandoval, S. *Thin Solid Films* 2001, 389, 200.
- Akitt, J. W.; Farthing, A. J. *Chem. Soc. Dalton*, 1981, 1615-1616.
- Akitt, J. W.; Farthing, A. J. *Chem. Soc. Dalton Trans.* 1981, 1617-1623.
- Alizadehhesari, K., Golding, S. D. & Bhatia, S. K. *Energy Fuels* 26, 783-790, (2012).
- Allouche, L.; Gerardin, C.; Loiseau, T.; Ferey, G.; Taulelle, F. *Angew. Chem. Int. Ed.* 2000, 39, 511.
- Altamirano-Fortoul, R., Le-Bail, A., Chevallier, S. & Rosell, C. M. *J. Food Eng.* 108, 128-134, (2012).
- Alvarez, N. T.; Hamilton, C. E.; Pint, C. L.; Orbaek, A.; Yao, J.; Frosinini, A. L.; Barron, A. R.; Tour, J. M.; Hauge, R. H. *Acs Appl. Mater. & Interfaces* 2010, 2, 1851.
- Anderson, J. T.; Munsee, C. L.; Hung, C. M.; Phung, T. M.; Herman, G. S.; Johnson, D. C.; Wager, J. F.; Keszler, D. A. *Adv. Funct. Mater.* 2007, 17, 2117.
- Baes, C. F.; Mesmer, R. E. *The Hydrolysis of Cations*, 1976.
- Banger, K. K. et al. *Nat. Mater.* 10, 45-50, (2011).
- Bartzsch, H.; Gloss, D.; Bocher, B.; Frach, P.; Goedicke, K. *Surf. Coat. Technol.* 2003, 174, 774.
- Bobzin, K.; Bagcivan, N.; Immich, P.; Ewering, M. *Adv. Eng. Mater.* 2009, 11, 590.
- Bohn, H.; McNeal, B.; O'Connor, G. *Soil Chemistry*, 3rd edition; John Wiley & Sons: New York, 2001.
- Bray, H. J. & Redfern, S. A. T. *Phys. Chem. Miner.* 26, 591-600, (1999).

- Carmona-Tellez, S.; Guzman-Mendoza, J.; Aguilar-Frutis, M.; Alarcon-Flores, G.; Garcia-Hipolito, M.; Canseco, M. A.; Falcony, C. J. *Appl. Phys.* 2008, 103, 034105.
- Casey, W. H. *Chem. Rev.* 2006, 106, 1-16.
- Casey, W. H.; Olmstead, M. M.; Phillips, B. L. *Inorg. Chem.* 2005, 44, 4888.
- Casey, W. H.; Phillips, B. L.; Furrer, G. *Rev. Mineral. Geochem.* 2001, 44, 167.
- Cheng, H. F. et al. *J. Colloid Interface Sci.* 376, 47-56, (2012).
- Cibert, C.; Hidalgo, H.; Champeaux, C.; Tristant, P.; Tixier, C.; Desmaison, J.; Catherinot, A. *Thin Solid Films* 2008, 516, 1290.
- Delhaize, E.; Ryan, P. R.; *Plant Physiol.* 1995, 107, 315.
- Di Fonzo, F.; Tonini, D.; Bassi, A. L.; Casari, C. S.; Beghi, M. G.; Bottani, C. E.; Gastaldi, D.; Vena, P.; Contro, R. *Appl. Phys. A-Mater. Sci. Process.* 2008, 93, 765.
- Donovan, J. J.; Tingle, T. N. *Microscopy and Microanalysis* 1996, 2, 1.
- Duan, X. F.; Tran, N. H.; Roberts, N. K.; Lamb, R. N. *Thin Solid Films* 2009, 517, 6726.
- Fitzgerald, J. J.; Kohl, S. D.; Piedra, G.; Dec, S. F.; Maciel, G. E. *Chem. Mater.* 1994, 6, 1915-1917.
- Fleetwood, D. M. et al. *IEEE Trans. Nucl. Sci.* 42, 1698-1707, (1995).
- Frach, P.; Bartzsch, H.; Gloss, D.; Fahland, M.; Handel, F. *Surf. Coat. Technol.* 2008, 202, 5680.
- Francel, M. M.; Pietro, W. J.; Hehre, W. J.; Binkley, J. S.; De-Frees, D. J.; Pople, J. A.; Gordon, M. S. *J. Chem. Phys.* 1982, 77, 3654.
- Fricke, S.; Friedberger, A.; Schmid, U. *Surf. Coat. Technol.* 2009, 203, 2830.
- Frydman, L.; Harwood, J. S. *J. Amer. Chem. Soc.* 1995, 117, 5367-5368.
- Gatlin, J. T., Mensinger, Z. L., Zakharov, L. N., MacInnes, D. & Johnson, D. W. *Inorg. Chem.* 47, 1267-1269, (2008).
- Gaussian 09, Revision B.01, Frisch, M. J. et al. Gaussian, Inc., Wallingford, CT, 2009.

- Gensemer, R. W.; Playle, R. C. *Crit. Rev. Environ. Sci. Technol.* 1999, 29, 315.
- George, S. M. *Chem. Rev.* 2010, 110, 111.
- Ghiraldelli, E.; Pelosi, C.; Gombia, E.; Frigeri, C.; Vanzetti, L.; Abdullayeva, S. *Jpn. JI of Appl. Phys.* 2008, 47, 8174.
- Gorz, H.; Schonherr, S.; Pertlik, F. *Monatsh. Chem.* 1991, 122, 759-764.
- Groner, M. D.; Elam, J. W.; Fabreguette, F. H.; George, S. M. *Thin Solid Films* 2002, 413, 186.
- Guidelines for Drinking Water Quality, 4th edition; World Health Organization: Geneva, 2011.
- Gutmann, E.; Meyer, D. C.; Levin, A. A.; Paufler, P. *Appl.Phys. A: Mater. Sci. & Proc.* 2005, 81, 249.
- Harlov, D. E., Johansson, L., Van Den Kerkhof, A. & Forster, H. J. *J. Petrol.* 47, 3-33 (2006).
- Heyrovsky, III, J. J. *Chem. Soc.* 1920, 117, 11.
- Hibberd, C. J. et al. *Prog. Photovoltaics* 18, 434-452, (2010).
- Hoex, B. et al. *Appl. Phys. Lett.* 2007, 91, 112107.
- Hoex, B.; Schmidt, J.; Bock, R.; Altermatt, P. P.; van de Sanden, M. C. M.; Kessels, W. M. M. *Applied Physics Letters* 2007, 91.
- Hoex, B.; Schmidt, J.; Pohl, P.; van de Sanden, M. C. M.; Kessels, W. M. M. *Journal of Applied Physics* 2008, 104.
- Hu, C. Z.; Liu, H. J.; Qu, J. H. *Colloid Surface A* 2005, 260, 109.
- Ip, K. et al. *Appl. Phys. Lett.* 82, 385-387, (2003).
- Jiang, K., Meyers, S. T., Anderson, M. D., Johnson, D. C. & Keszler, D. A. *Chem. Mat.* 25, 210-214, (2013).
- Jiang, K.; Anderson, J. T.; Hoshino, K.; Li, D.; Wager, J. F.; Keszler, D. A. *Chem. Mat.* 2010, 23, 945.

- Jiang, K.; Zakutayev, A.; Stowers, J.; Anderson, M. D.; Tate, J.; McIntyre, D. H.; Johnson, D. C.; Keszler, D. A. *Solid State Sci.* 2009, 11, 1692.
- Johansson, G. *Acta Chem. Scan.* 1962, 16, 403-420.
- Johansson, G. *Acta Chem. Scand.* 1960, 14, 771- 773.
- Johansson, G.; Lundgren, G.; Sillen, L. G.; Soderquist, R. *Acta Chem. Scand.* 1960, 14, 769- 771.
- Kablukov, I.; Sachanov, A. *Z. Physik. Chem.* 1910, 69, 419.
- Kelly, P. J.; Arnell, R. D. *J. Vac. Sci. Technol. A-Vac. Surf. Films* 1999, 17, 945.
- Kim, H.; Lee, H. B. R.; Maeng, W. J. *Thin Solid Films* 2009, 517, 2563.
- Kobayashi, T.; Itoh, Y.; Nakano, Y.; Hirai, E.; Hashimoto, R.; Kamikawa, S. *J. Vac. Sci. Technol. A* 2006, 24, 939.
- Kristof, J., Vassanyi, I., Nemezc, E. & Inczedy, J. *Thermochim. Acta* 93, 625-628, (1985).
- Kumar, L., Saha, D., Khan, S. A., Sengupta, K. & Islam, T. *IEEE Sens. J.* 12, 1625-1632, (2012).
- Le-bail, A. et al. *J. Food Eng.* 105, 379-385, (2011).
- Lee, H. D. et al. *Appl. Phys. Lett.* 94, (2009).
- Leskela, M.; Ritala, M. *Thin Solid Films* 2002, 409, 138.
- Li, Q.; Yu, Y. H.; Bhatia, C. S.; Marks, L. D.; Lee, S. C.; Chung, Y. W. *J. Vac. Sci. Technol. A* 2000, 18, 2333.
- Lim, J. W.; Yun, S. J. *Electrochem. Solid State Lett.* 2004, 7, F45.
- Liu, W. M.; Zhu, L. D.; Fang, C. *Opt. Lett.* 2012, 37, 3783.
- Madejová, J. *Vibrational Spectroscopy* 31, 1-10, (2003).
- Massiot, D.; Touzo, B.; Trumeau, D.; Coutures, J. P.; Virlet, J.; Florian, P.; Grandinetti, P. *J. Solid State Nucl. Mag.* 1996, 6, 73-83.
- Meyerhofer, D. *J. Appl. Phys.* 1978, 49, 3993.

- Meyers, S. T.; Anderson, J. T.; Hong, D.; Hung, C. M.; Wager, J. F.; Keszler, D. A. *Chem. Mater.* 2007, 19, 4023.
- Meyers, S. T.; Anderson, J. T.; Hung, C. M.; Thompson, J.; Wager, J. F.; Keszler, D. A., *J. Amer. Chem. Soc.* 2008, 130, 17603.
- Mondal, A. & Datta, A. K. *J. Food Eng.* 86, 465-474, (2008).
- Onishi, K. et al. *IEEE Trans. Electron Devices* 50, 1517-1524, (2003).
- Ozer, N.; Cronin, J. P.; Yao, Y. J.; Tomsia, A. P. *Sol. Energy Mater. Sol. Cells* 1999, 59, 355.
- Pacewska, B.; Keshr, M. *Thermochimica Acta* 2002, 385, 73.
- Pasquarelli, R. M., Ginley, D. S. & O'Hayre, R. *Chem. Soc. Rev.* 40, 5406-5441, (2011).
- Phani, A. R.; Santucci, S. *J. of Non-Cryst. Solids* 2006, 352, 4093.
- Pulker, H. K. *Coatings on Glass*; Elsevier: Amsterdam, 1984.
- RIAZ, S.; SHAMAILA, S.; KHAN, B.; NASEEM, S. *Surf. Rev. and Lett.* 2008, 15, 681.
- Robertson, J. *Rep. Prog. Phys.* 2006, 69, 327.
- Roothaan, C. C. J. *Rev. Mod. Phys.* 1951, 23, 69.
- Rowell, J.; Nazar, L. F. *J. Amer. Chem. Soc.* 2000, 122, 3777-3778.
- Rudolph, W. W.; Mason, R.; Pye, C. C. *Phys. Chem. Chem. Phys.* 2000, 2, 5030.
- Schmidt, J. et al. *Prog. Photovoltaics* 2008, 16, 461.
- Schonherr, S.; Gorz, H. Z. *Anorg. Allg. Chem.* 1983, 503, 37-42.
- Schweitzer, G. K.; Pesterfield, L. L. *The Aqueous Chemistry of the Elements*; Oxford University Press: USA, 2010.
- Segda, B. G.; Jacquet, M.; Besse, J. P. *Besse Vacuum* 2001, 62, 27.
- Segda, B. G.; Jacquet, M.; Caopera, C.; Baud, G.; Besse, J. P. *Nucl. Instrum. Methods Phys. Res. Sect. B-Beam Interact. Mater. Atoms* 2000, 170, 105.

- Seichter, W., Mogel, H. J., Brand, P. & Salah, D. *Eur. J. Inorg. Chem.*, 795-797 (1998).
- Shamala, K. S.; Murthy, L. C. S.; Rao, K. N. *Mater. Sci. Eng. B-Solid State Mater. Adv. Technol.* 2004, 106, 269.
- Shih, W. C.; Wang, T. L.; Hsu, L. L. *Thin Solid Films* 2010, 518, 7143.
- Tomasi, J.; Mennucci, B.; Cammi, R. *Chem. Rev.* 2005, 105, 2999.
- Udomkana, N.; Limusuwan, P. *Int. J. Mod. Phys. B* 2008, 22, 4217.
- van Hemmen, J. L.; Heil, S. B. S.; Klootwijk, J. H.; Roozeboom, F.; Hodson, C. J.; van de Sanden, M. C. M.; Kessels, W. M. M. *Journal of The Electrochemical Society* 2007, 154, G165.
- Vanbesien, K.; Visschere, P. D.; Smet, P. F.; Poelman, D. *Thin Solid Films* 2006, 514, 323.
- Vanin, F. M., Lucas, T. & Trystram, G. *Trends Food Sci. Technol.* 20, 333-343, (2009).
- Vitanov, P.; Harizanova, A.; Ivanova, T.; Dimitrova, T. *Thin Solid Films* 2009, 517, 6327.
- Voigt, M.; Sokolowski, M. *Mater. Sci. Eng. B-Solid State Mater. Adv. Technol.* 2004, 109, 99.
- Wang, J. L.; Yu, Y. H.; Lee, S. C.; Chung, Y. W. *Surf. Coat. Technol.* 2001, 146, 189.
- Wang, W.; Chang, I.-Y.; Zakharov, L.; Cheong, P. H.-Y.; Keszler, D. A. *Inorg. Chem.* 2013, 52, 1807.
- Wang, W.; Wentz, K. M.; Hayes, S. E.; Johnson, D. W.; Keszler, D. A. *Inorg. Chem.* 2011, 50, 4683.
- Wefers, K.; Chanakya, M. *Oxides and Hydroxides of Aluminum*, 1987.
- Wilk, G. D., Wallace, R. M. & Anthony, J. M. *J. Appl. Phys.* 89, 5243-5275, (2001).
- Wright, K. *Water in Nominally Anhydrous Minerals* 62, 67-83, (2006).

Yamaguchi, N., Tadanaga, K., Matsuda, A., Minami, T. & Tatsumisago, M. *Thin Solid Films* 515, 3914-3917, (2007).

Zhang, M., Redfern, S. A. T., Salje, E. K. H., Carpenter, M. A. & Wang, L. *Am. Miner.* 95, 1686-1693, (2010).

Zhang, W., Liu, W. & Xue, Q. *Mater. Res. Bull.* 36, 1903-1914 (2001).

Zhang, X.-H.; Domercq, B.; Wang, X.; Yoo, S.; Kondo, T.; Wang, Z. L.; Kippelen, B. *Org. Electronics* 2007, 8, 718.

Zhou, R. S.; Snyder, R. L. *Acta Crystallogr. Sect. B-Struct. Commun.* 1991, 47, 617.

Appendix A: Supporting information for Chapter 3

Expanded Discussion of the Electrochemical Synthesis Method:

The mechanism for the observed pH rise in the cathode compartment is explained as follows.

1. In the anode counter-electrode compartment H_2O is oxidized to generate $\text{O}_2(\text{g})$ and H^+ . The ionic species, Al^{3+} and NO_3^- , are oxidatively stable.
2. In the cathode working-electrode compartment, two possible reactions could occur:
 - (a) NO_3^- reduction¹ to form NO_2^- , NO_2 , NH_3 , or N_2
 - (b) H^+ reduction to form H_2 .

Both cathode reduction reactions lead to a net consumption of H^+ from the solution and would thus raise the pH. On Pt, however, NO_3^- reduction has slow kinetics compared with H^+ reduction. Under hydrogen evolution conditions, i.e., negative of the reversible hydrogen potential, adsorbed Pt-H is known to block adsorbed NO_3^- and therefore lead to preferential reduction of H^+ over NO_3^- . H_2 is therefore the primary product at the Pt cathode, which is consistent with the lack of noticeable color change in the solution that might indicate the formation of reduced NO_3^- products such as NO_2 , and the observation of significant bubble generation. The electrode potentials are not sufficiently negative to reduce Al^{3+} .

The faradaic current at the electrodes is balanced by ionic current through the solution between the anode and cathode compartments. In the initial solution the $\text{Al}(\text{H}_2\text{O})_6^{3+}$ and NO_3^- are present in large concentrations (e.g. 1 and 3 M, respectively) relative to H^+ (< 0.1 M). The bulk of the charge-balancing ionic current across the frit is therefore carried by $\text{Al}(\text{H}_2\text{O})_6^{3+}$ migration into the cathode compartment and NO_3^- migration into the anode compartment. As the electrolysis reaction proceeds, the pH of the cathode compartment increases and that of the anode compartment decreases. At the end of the electrolysis the anode compartment pH was measured to be ~ -0.5 (i.e. $[\text{H}^+] \sim 3 \text{ M}$, consistent with the

proposed reaction scheme). The resulting pH gradient drives a diffusion flux of H^+ and NO_3^- from the anode compartment into the cathode compartment that tends to slow the rise in pH toward the end of the electrolysis experiment as is observed in Figure. 3.1.

The electrolysis method is a reagent-less aqueous synthesis route for metal-hydroxide clusters. It eliminates the need for isolation and purification steps that are required with basic titrations or when metallic chemical reduction agents such as Zn are used². It also provides a convenient method to precisely tune the pH in solution-speciation studies without affecting the solution volume or adding reagents/impurities that could influence the cluster formation. The pH change rate can be easily controlled by the current passed and the final solution pH can be adjusted by setting the total charge passed into the system (and therefore the electrolysis time). Solutions from the cathode compartment are useful to study the formation of aqueous polycations, e.g., Al_{13} clusters, that form upon transition from acidic to more-neutral pHs. The use of large-area electrode, small current, and rapid stirring minimizes local pH gradients and ensures that the pH remains homogenous in the cathode solution. Since no other reagents besides the precursor solution are added during the reaction, the solution volume remains constant and the impurity content in the final product is minimized. The electrolysis method therefore prevents the formation of unwanted species and reduces complexity in the purification of the product.

An ^{27}Al NMR spectrum (Figure A.1) confirms a low concentration of tetrahedral species. The integration of the peak area indicates there is only 0.05% of Al present in the highly symmetric tetrahedral site in the Keggin Al_{13} , which indicates the Keggin Al_{13} ion is not a dominate species in the final cathode solution. This could be caused by the constant current electrolysis. Change in pH introduced by the current becomes relatively significant near the electrodes at the end of the reaction even though the overall cathode pH change appears to slow down. A gradually decreased current might be considered in the future to minimize this effect. Some

recent studies also suggest the conversion from *flat* Al_{13} to Keggin Al_{13} ions³. Our forthcoming experiment at a more neutral pH range will help provide more information into this interesting area.

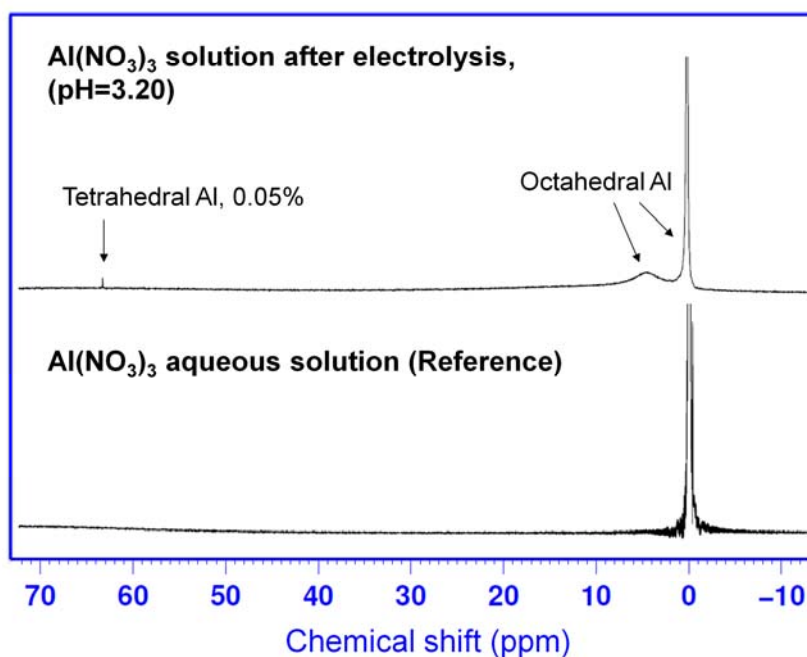


Figure A.1. ^{27}Al solution NMR spectra of cathode solution (pH = 3.20) using 1.0 M $\text{Al}(\text{NO}_3)_3(\text{aq.})$ solution as reference.

X-ray Diffraction Analysis of Single Crystals from Cathode Solutions:

Cathode solutions at different pHs were allowed to evaporate under ambient conditions for crystallization. The crystals were analyzed by single-crystal X-ray diffraction methods (Bruker Apex CCD diffractometer, Mo $\text{K}\alpha$ radiation, $\lambda = 0.07073\text{\AA}$, $T = 173\text{ K}$). The unit-cell parameters of crystals obtained from different cathode solutions are listed in Table A.1. They are consistent with the values of the flat Al_{13} nitrate single crystals reported by Gatlin⁴ and Wang².

Table A.1. Unit cell parameters of crystals obtained from cathode solutions with different pH values

pH	Space group	Unit cell parameters
2.70	$P\bar{1}$	$a = 12.9020(11) \text{ \AA}$, $b = 13.1720(10) \text{ \AA}$, $c = 13.3826(8) \text{ \AA}$ $\alpha = 80.033(5)^\circ$, $\beta = 73.276(7)^\circ$, $\gamma = 89.187(7)^\circ$ $V = 2143.7(3) \text{ \AA}^3$
2.76	$P\bar{1}$	$a = 12.9001(9) \text{ \AA}$, $b = 13.1450(13) \text{ \AA}$, $c = 13.3668(12) \text{ \AA}$ $\alpha = 80.070(8)^\circ$, $\beta = 73.373(8)^\circ$, $\gamma = 89.154(7)^\circ$ $V = 2137.9(4) \text{ \AA}^3$
2.80	$P\bar{1}$	$a = 12.8829(16) \text{ \AA}$, $b = 13.1351(17) \text{ \AA}$, $c = 13.3618(13) \text{ \AA}$ $\alpha = 80.225(13)^\circ$, $\beta = 73.076(10)^\circ$, $\gamma = 89.146(11)^\circ$ $V = 2130.3(6) \text{ \AA}^3$
2.85	$P\bar{1}$	$a = 12.8821(15) \text{ \AA}$, $b = 13.1438(14) \text{ \AA}$, $c = 13.3649(23) \text{ \AA}$ $\alpha = 80.245(15)^\circ$, $\beta = 73.179(8)^\circ$, $\gamma = 89.115(10)^\circ$ $V = 2133.4(5) \text{ \AA}^3$
2.95	$P\bar{1}$	$a = 12.8891(11) \text{ \AA}$, $b = 13.1475(11) \text{ \AA}$, $c = 13.3693(12) \text{ \AA}$ $\alpha = 80.145(6)^\circ$, $\beta = 73.275(7)^\circ$, $\gamma = 89.179(6)^\circ$ $V = 2136.2(3) \text{ \AA}^3$
3.00	$P\bar{1}$	$a = 12.8973(17) \text{ \AA}$, $b = 13.1567(16) \text{ \AA}$, $c = 13.3770(12) \text{ \AA}$ $\alpha = 80.015(8)^\circ$, $\beta = 73.306(7)^\circ$, $\gamma = 89.252(8)^\circ$ $V = 2139.7(5) \text{ \AA}^3$
3.10	$P\bar{1}$	$a = 12.8976(9) \text{ \AA}$, $b = 13.1411(15) \text{ \AA}$, $c = 13.3738(10) \text{ \AA}$ $\alpha = 79.979(6)^\circ$, $\beta = 73.289(6)^\circ$, $\gamma = 89.154(11)^\circ$ $V = 2136.4(4) \text{ \AA}^3$

Newly Improved Femtosecond Stimulated Raman (FSR) Method:

Cathode solutions at different pH values, corresponding to different time points in the electrolysis reaction, were directed into a 1-mm pathlength flow cell for in situ FSR spectroscopy measurements. FSR studies were performed by using a new ultrafast laser system consisting of a mode-locked Ti:sapphire oscillator (Mantis-5, Coherent) and regenerative amplifier (Legend Elite-USP-1K-HE, Coherent Inc.), which provides 35 femtosecond (fs) pulses centered at 800 nm with ~ 4.1 mJ/pulse energy at 1 kHz repetition rate. For the ground-state Raman spectrum, about half of the output laser beam is split into two beams to generate a narrow-bandwidth picosecond (ps) Raman pump pulse and a broadband fs Raman probe pulse (Figure A.2). The fundamental laser beam with pulse energy of ~ 1.6 mJ/pulse is dispersed by a reflective ruled grating (1200 grooves/mm, wavelength first order at 750 nm, blaze angle $\theta = 26.7^\circ$), and then passed through an adjustable slit with the width of ~ 90 μm corresponding to the Raman pump pulse bandwidth of ~ 10 cm^{-1} and pulse duration of ~ 3.5 ps. The FSR methodology provides much higher signal-to-noise ratio (SNR) than conventional continuous-wave (cw) Raman spectroscopy because of the synchronization with the 1 kHz laser repetition rate. This enables fast data acquisition and therefore makes in situ speciation studies possible in conjunction with a solution sample flow cell. Other benefits include much higher excitation peak density as well as fluorescence and scattering rejection. The broad spectral window spanning over ~ 1500 cm^{-1} is an added bonus to simultaneously observe a range of molecular vibrational modes, FSR detection, however, is typically limited to >600 cm^{-1} based on the conventional super-continuum white light (SCWL) pulse generation in a sapphire plate⁵.

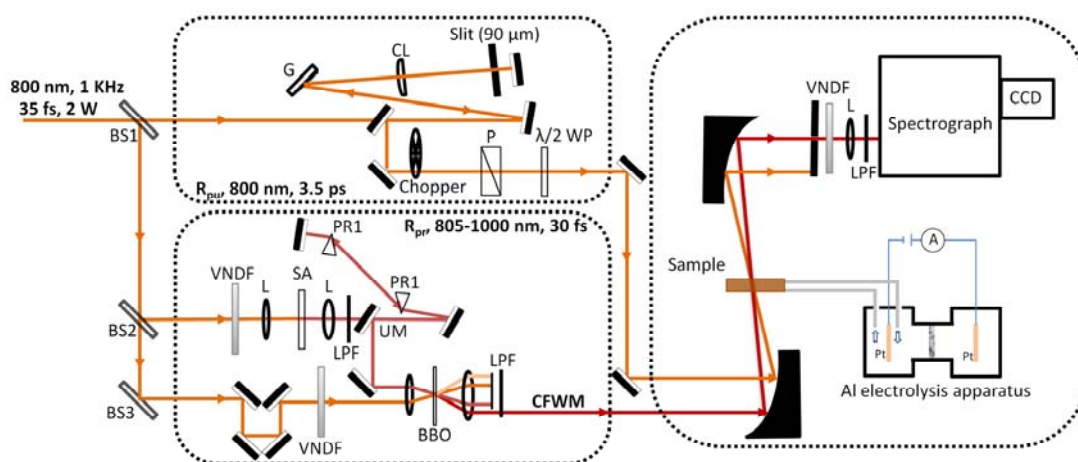


Figure A.2. Schematic of the newly improved non-resonant FSR spectroscopy. The output laser beam from a Coherent fs regenerative amplifier is split to generate two ultrafast laser pulses for ground state FSR spectra: Raman pump beam at 800 nm (~ 3.5 ps, 6 mW) and Raman probe beam with the wavelength range of 805–1000 nm (~ 30 fs, 100 nW). The Al electrolysis apparatus for precise pH control to study the aqueous Al cluster speciation is described in the text. BS: beamsplitter, G: reflective ruled diffraction grating (1200 grooves/mm, blazed at 750 nm), CL: cylindrical lens, UM: pick-up mirror, VNDf: variable neutral density filter, L: bi-convex lens ($f = 10$ or 5 cm), SA: sapphire plate, BBO: 0.1-mm-thick β -barium borate crystal (type I, $\theta = 27.8^\circ$), LPF: long-wavelength pass filter, PR1: fused silica prism pair, P: polarizer, $\lambda/2$ WP: half-wavelength waveplate at 800 nm, and CFWM: cascaded four-wave-mixing spatially-separated self-compressed sideband signal used as the new Raman probe beam to stimulate the Stokes Raman signal collected in this experiment.

To extend the FSR detection window to <300 cm^{-1} and to observe reactant consumption as well as intermediate and product formation, the newly developed Raman probe beam is a cascaded four-wave-mixing (CFWM) signal generated by crossing two laser pulses in a 0.1-mm-thick BBO crystal⁶ (Type-I, phase matching angle $\theta = 27.8^\circ$). About 15 $\mu\text{J}/\text{pulse}$ of the laser output is focused by an $f = 10$ cm BK7 lens on a 2-mm-thick Z-cut single crystal sapphire plate to generate SCWL, which is then collimated by an $f = 5$ cm lens. The IR component of the SCWL pulse with wavelength centered at ~ 824 nm is selected by using a long-wavelength pass filter (LPF-RG830, Newport) followed by temporal compression with a fused silica prism pair to produce the ~ 45 fs broadband IR pulse (used as the Raman

probe in conventional FSR spectroscopy^{5,7,8}. A small portion of the fundamental laser (FL) beam ($\sim 30 \mu\text{J}/\text{pulse}$) passes through a delay stage and is attenuated by a variable neutral density filter (VNDF). The two beams with the same p polarization are then loosely focused onto the 0.1-mm-thick BBO crystal using an $f = 10 \text{ cm}$ lens with a crossing angle of $\sim 6^\circ$. Both incident beam diameters on the crystal are $\sim 0.2 \text{ mm}$ with energy of $\sim 3 \mu\text{J}/\text{pulse}$ for the 800-nm FL beam and $\sim 100 \text{ nJ}/\text{pulse}$ for the SCWL beam. When we temporally and spatially overlap the two crossing laser beams with the BBO crystal rotated to the sum-frequency-generation phase-matching angular condition, two independent spatially-separated self-compressed multicolor sidebands (spanning the broad wavelength range from UV/Visible to near-Infrared regions) associated with CFWM signals simultaneously appear on both sides of the FL beam⁶. One of the CFWM signals with center wavelength at $\sim 900 \text{ nm}$ is selected (by using an iris diaphragm) as the Raman probe beam here, which corresponds to the Stokes frequency range from $100\text{--}3000 \text{ cm}^{-1}$ (Raman pump at $\sim 800 \text{ nm}$) and pulse duration of $\sim 30 \text{ fs}$. Raman pump and probe beams are then focused onto the sample cell by an off-axis parabolic reflective mirror to minimize chirp. After the sample, the Raman pump beam is blocked by an iris while the Raman probe beam carrying the stimulated Raman signal is re-collimated and focused into the spectrograph. An LPF and a circular VNDF (OD = 0.05–1, Newport) are put in front of the spectrograph to further block the scattering of the much stronger Raman pump beam and avoid signal saturation of the detector. Inside the spectrograph, the probe beam is dispersed by a 600 grooves/mm reflective ruled grating (wavelength first order at 1000 nm, blaze angle $\theta = 17.5^\circ$) and imaged on a CCD camera (Princeton Instruments, PIXIS 100F) consisting of 1340×100 pixel array and being synchronized at the 1 kHz laser repetition rate.

All of the FSR spectra are calibrated using a 1:1 carbon tetrachloride (CCl_4) and ethanol ($\text{CH}_3\text{CH}_2\text{OH}$) mixed solution that covers the Stokes Raman frequency region from $\sim 100\text{--}1800 \text{ cm}^{-1}$. The ground state Raman signal of the standard solution is maximized via fine-tuning of the spatial and temporal overlap between

the Raman pump and probe beams. A comprehensive LabVIEW program has been developed on a PC to control the entire apparatus, collect data clocked at the 1 kHz repetition rate, perform averages, and store the final data for analysis. The sample is measured in a short-pathlength (thickness = 1 mm) flow cell (48-Q-1, Starna Cells) sandwiched by two 1-mm-thick quartz glass windows. A phase-locked optical chopper (New Focus 3501) is synchronized with the main laser output at 1 kHz and used to chop the Raman pump beam at 500 Hz, so we collect one FSR spectrum in 2 ms according to the formula:

Stimulated-Raman-Gain

$$= \text{Raman-probe-Intensity}_{\text{pump-on}} / \text{Raman-probe-spectrum}_{\text{pump-off}}$$

Expanded Discussion of FSR Data Collection and Analysis:

Typically, we collected 120 sets of spectra, each consisting of 3000 laser shots (~3 s), so 180,000 spectra (~6 min) are efficiently averaged to obtain one ground state FSR spectrum of the sample solution. The precursor solution (1.0 M $\text{Al}(\text{NO}_3)_3(\text{aq.})$) spectrum is collected in exactly the same manner right before each sample solution measurement. The sum of integrated peak areas of NO_3^- vibrations, i.e., 718 and 1048 cm^{-1} , in each precursor solution is used as the factor to normalize across the whole pH-dependent sample solution measurement range. Thus, the effects of both short-term and long-term laser fluctuations are minimized on each differential Raman spectrum, i.e., sample spectrum minus precursor spectrum. A broad, featureless spline baseline is subtracted from each pH-dependent differential FSR spectrum to obtain Figure 3.2. The spectral range is consistently defined by detectable vibrational features. We then apply a 5-point binomial smoothing to remove the short-term spectral noise likely from the fast electronics. Besides the strong negative dips, we focus on the broad positive peaks that are intimately probing the solvated Al species with vibrational sensitivity and specificity, aided by systematic computations. The SNR at these positive peak locations is consistently above 4. The SNR further improves with pH and the

generation of new Al species, validating the differential FSR method, which traces both reactant consumption and product emergence within one broad detection window of ca. 350—1400 cm^{-1} .

After the multiple-Gaussian peak fitting, stimulated Raman peak intensities (Figure 3.4) are derived as integrated peak areas to account for the broad nature of the spectral features and the mode inhomogeneity in the solution phase. The strong negative peaks at 525, 718 and 1048 cm^{-1} , corresponding to the Al–O stretching and two NO_3^- vibrations, respectively, are used to infer the reaction dynamics by their integrated peak areas (Figure 3.4) in correlation with the positive signal evolution at other key spectral locations. The multi-staged signal evolution for both the spectral dips and peaks excludes the possibility of simple noise or laser fluctuations. The adding back of the strong dips by a scaled precursor solution spectrum, e.g., commonly used in excited state differential FSR spectral analysis⁸, is not attempted because of the large inhomogeneity inherent to those collective vibrational modes as well as the pH-specific Al speciation in solution. The positive peaks at 585, 611, 675, 777, 937, 1151 and 1275 cm^{-1} (Figure 3.2) are thus primarily used to compare with computational results and draw conclusions (Figure 3.3). Notably, the control FSR experiments on a series of concentration-dependent, i.e., 1-3 M, solution samples consisting of $\text{Al}(\text{NO}_3)_3$, HNO_3 , and NaNO_3 , respectively (data not shown), further corroborate the existence of positive peaks at ~ 1006 , 1151, and 1275 cm^{-1} , which are associated with Al aqueous clusters. The dispersive lineshape or the small sidebands discussed previously⁹ do not apply to our spectral analysis here due to (i) the Raman pump and probe pulse time delay is fixed at maximal spatial and temporal overlap in our experiment, and (ii) the observed peak evolution is pH-dependent not time-resolved. Therefore, the delineation of multiple sequential reaction stages via precise pH control is firmly supported by experimental data and computational analyses discussed in the main text.

In addition, computations reveal that Raman peaks from 350—900 cm^{-1} primarily arise from terminal $\text{-H}_2\text{O}$ and skeletal Al–O vibrations, e.g., the prominent 386 cm^{-1} mode in Figure 3.2. The condensation of $\text{Al}^{3+}(\text{aq.})$ likely involves the formation of polynuclear species exhibiting different Al–O stretching. These terminal $\text{-H}_2\text{O}$ and skeletal Al–O vibrations, however, are strongly coupled, so it is difficult to determine their individual contributions. Moreover, possible rapid exchanges between $\text{-H}_2\text{O}$ and surrounding solvent water molecules lead to large uncertainty of spectral assignment in this region. In contrast, Raman peaks from 900—1300 cm^{-1} can be attributed almost explicitly to the vibration of hydroxo groups, which are highly specific to aqueous Al cluster structures, so the appearance and quantity of different types of hydroxo groups are directly related to the evolution of Al polycation structures. Therefore, a close examination of the differential FSR spectra in this region can provide essential insight into the $\text{Al}^{3+}(\text{aq.})$ aqueous behavior as discussed in the main text. Indeed, characteristic vibrational modes along the speciation pathway are found to match well between experiments and computations over a broad spectral range.

The same experiment described in the text was also repeated multiple times to ensure reproducibility. The pH-dependent evolution of selected vibrational mode intensities (measured from the integrated peak areas) from an independently collected dataset for comparison to the data reported in the main text are summarized in Figure A.3. The three distinct reaction stages for Al_{13} cluster formation are effectively reproduced.

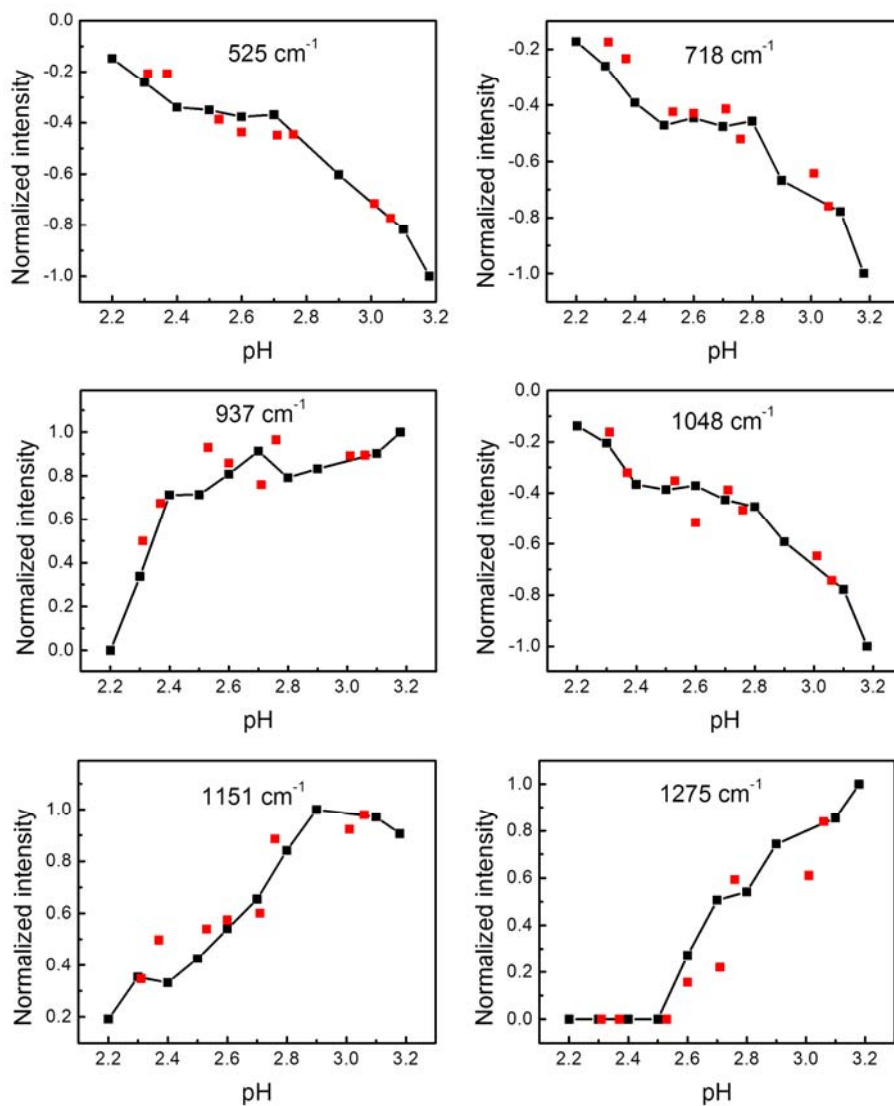


Figure A.3. An independently collected dataset is shown in red in comparison to the data from the main text (in black), exhibiting the same trend within experimental uncertainty in signal evolution discussed therein.

Computational Methods for FSR Raman Spectral Analysis

To ensure accurate predictions of the intermediates present in solution, multiple Least-Squares Fitted Computed (LSFC) Raman spectra were computed and juxtaposed with the positive signal of the differential FSR (pH = 3.18), which reflects the emerging species during the electrolysis process.

- The LSFC Raman spectra for each Al clusters listed in Figure A.4 are shown in Figure A.9-A.15. These clusters include:
 - The *flat* Al₁₃, harvested from the cathode solution at pH = 2.70-3.10 range
 - Two possible intermediates, Al₇ and Al₇₊₁, similar to the Al₇ core of the *flat* Al₁₃
 - The Al₆ structure, a six member ring of Al-O octahedral, is another possible intermediate structure. It is the building unit of the basal plane in Gibbsite Al(OH)₃
 - Al₂ and Al₈, whose crystal structure been reported^{10,11} and may exist in the solution
 - Al₁ cluster (the Al(H₂O)₆³⁺ ion)
 - Note: The Keggin Al₁₃ is excluded here since solution ²⁷Al NMR studies (Fig. S1) of the final cathode solution (pH = 3.18) indicate that only ~0.05% of the Al atoms occupy a highly symmetric tetrahedral site.
- The root mean squared deviation (RMSD) values of the single-component LSFC Raman spectra show that *flat* Al₁₃, Al₇ and Al₇₊₁ (Figure A.9-A.11) are the most likely species in the cathode solution because they have the smallest RMSD values (6.6%, 6.6% and 6.2%, respectively) and best peak alignment with experimental Raman spectrum at 900-1300 cm⁻¹ region. The single-component LSFC Raman RMSD of Al₈, Al₆ and Al₂ and Al₁ (Figure

A.12-A.15) are suggestively worse, 7.1%, 7.9%, 8.8% and 16.3%, respectively.

- The multi-component LSFC Raman spectra computed from varying combinations of *flat* Al₁₃, Al₇ and Al₇₊₁ are shown in Figure A.5 to A.8. The LSFC Raman spectrum composing of vibrational modes of *flat* Al₁₃, Al₇ and Al₇₊₁ has the best peak alignment with the experimental Raman spectrum as well as the smallest RMSD value for the entire spectrum (350-1300 cm⁻¹) and for the region corresponding to hydroxide vibrations (900-1300 cm⁻¹). We therefore used this LSFC Raman spectrum for further analysis. The computed parameters for this three-component LSFC Raman spectrum are listed in Table A.2.

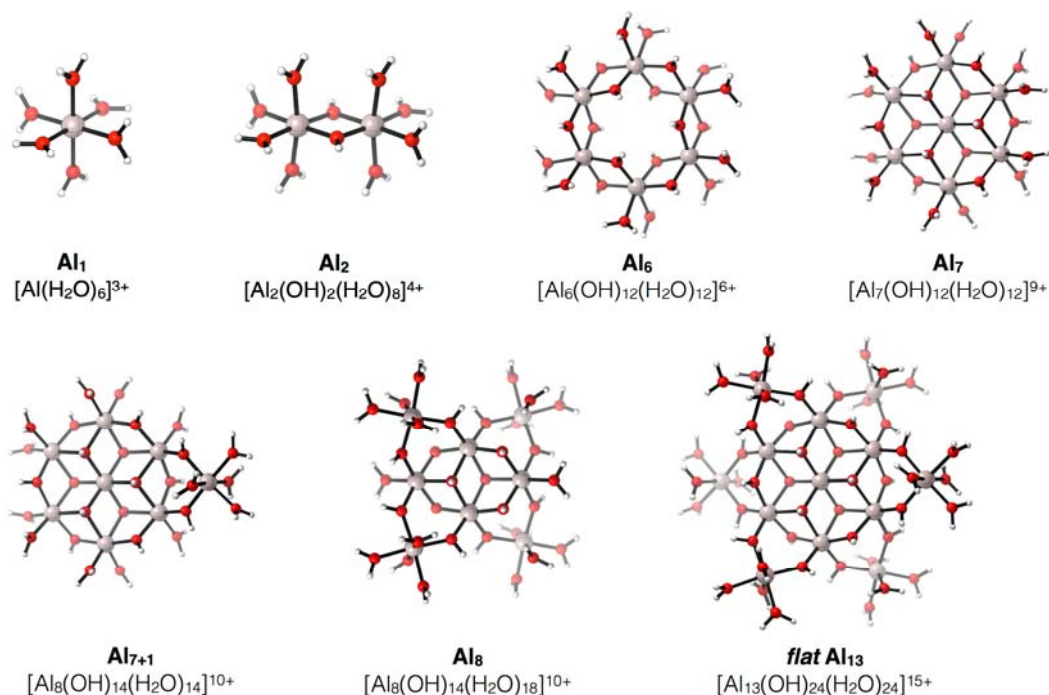


Figure A.4. The geometries of clusters whose LSFC Raman spectra were computed and used as reference for assignment of experimental spectra.

The Least-Squares Fitted Computed (LSFC) Raman spectrum, which is composed by Gaussian functions generated from the computed vibrational frequencies, Raman intensities and additional three scaling factors, is formulized as followed:

$$\sum_n (i_n) \exp \left[-\frac{(x - v_n)^2}{2 \left(\frac{w_n}{6} \right)^2} \right]$$

v_n = the computed Raman vibrational frequencies.

i_n = the normalized computed Raman vibrational intensities.

w_n = the widths of the constituent Gaussian functions.

Table A.2. The coefficients of the component Gaussian functions of the LSFC-Raman.

	v_n	i_n	w_n		v_n	i_n	w_n
1	317.7531306	0.049181621	49.6051	34	505.8136201	0.028887075	8.14626
2	318.6882579	0.043146738	49.4841	35	508.7334676	0.01163299	14.6835
3	321.0503272	0.047549331	48.6126	36	509.5696498	0.015903416	16.5205
4	329.5237052	0.068964787	36.916	37	511.1178481	0.010253571	23.6918
5	331.8052605	0.027007614	37.3731	38	515.9525723	0.022196933	29.8551
6	341.5435824	0.128112161	12.6221	39	521.8786016	0.025823626	41.0469
7	343.5738949	0.010489216	15.8673	40	525.1263257	0.008006298	48.1646
8	349.4436614	0.081471393	-0.0194797	41	533.6976786	0.002189809	48.1271
9	357.1225693	0.113128895	-0.0575216	42	534.9645626	0.004856664	44.9604
10	367.3730771	0.110352334	0.0194669	43	543.3031038	0.004960117	28.9631
11	374.5630803	0.03196775	24.9144	44	546.3995002	0.026340955	18.5121
12	378.4946889	0.01140887	29.8266	45	553.2596868	0.025915641	8.05312
13	381.5416128	0.048290718	27.1434	46	555.1280011	0.020938279	1.15064
14	388.573498	0.054992385	39.2441	47	561.3877273	0.015110228	-0.208638
15	390.869604	0.067171579	6.64363	48	577.536133	0.005908461	4.50579
16	401.3616539	0.199875816	-0.017121	49	583.513575	0.006730356	9.25098
17	404.4464098	0.026139761	3.98496	50	586.2335924	0.00039658	44.9027
18	406.3477058	0.058590327	0.502959	51	590.1021478	0.008707532	82.52
19	412.805322	0.002494431	35.2321	52	596.9060715	0.02108191	90.5388
20	416.9794428	0.008437374	-4.42088	53	600.3157937	0.000206911	53.2259
21	446.1701574	0.033174727	44.1794	54	605.3745992	0.018472587	69.8249
22	447.5767284	0.034985223	0.0372487	55	607.4611746	0.003149646	64.286
23	456.4555869	0.005856734	19.8485	56	609.4711162	0.019587611	58.0563
24	458.8360871	0.004011774	35.3192	57	632.2682377	0.619629714	-0.475607
25	467.3560275	0.047578082	0.0597022	58	632.70961	7.4718E-05	49.7292
26	473.3674212	0.000620733	49.1229	59	644.7149364	0.000505783	44.1984
27	476.6277559	0.017547232	16.242	60	648.1838317	8.62128E-05	49.4128
28	483.1755866	0.022857954	-0.0797976	61	669.6578064	0.001149506	57.7365
29	490.4014816	0.010690409	14.4348	62	674.8611492	0.001396652	67.9249
30	496.3158704	0.010420251	33.7313	63	676.7556549	0.002908251	80.2134
31	498.5217618	0.005253246	46.411	64	682.954268	0.004029018	106.94
32	502.821989	0.016368944	38.5498	65	686.4619652	0.000620733	68.6916
33	504.1800576	0.019627825	-5.58623	66	689.9648121	5.17277E-05	51.2166

Table A.2. The coefficients of all the component Gaussian functions of the LSFC-Raman (continued)

	V_n	i_n	W_n		V_n	i_n	W_n
67	734.1864359	0.004333641	49.6755	110	367.8590716	0.011943827	-1.94758
68	749.5665628	0.000293124	49.894	111	369.9572876	0.026373122	-15.4663
69	756.3287744	0.001143756	55.2862	112	373.2816455	0.026195262	9.72938
70	761.5369675	0.00183921	66.7863	113	378.6469866	0.012308473	26.6418
71	766.5530908	0.004247425	78.5112	114	379.5792037	0.015435716	27.3652
72	767.4920983	0.00574753	81.4823	115	382.9413935	0.002890822	39.569
73	773.148454	0.002528913	53.5223	116	386.7575663	0.05129637	33.1361
74	778.9609876	0.0119376	44.1538	117	389.661893	0.062281016	-0.0173109
75	786.4992384	0.047899917	79.0687	118	395.4142835	0.059315958	-8.60329
76	799.3155258	0.063515763	20.078	119	397.4736976	0.015834214	-3.32851
77	802.3925212	0.066205576	0.0740324	120	403.2678002	0.022298018	0.459694
78	833.3351442	0.000218406	50.3612	121	408.6535123	0.021012506	0.38971
79	934.7042946	0.040824676	78.2642	122	410.4287019	0.038578079	-0.0772119
80	939.7737707	0.030783762	97.024	123	415.6475656	0.017457485	0.000254718
81	994.5330368	0.009523647	68.0391	124	419.3162909	0.024106006	-0.602511
82	997.4043818	0.044284688	47.5041	125	426.4946535	0.005284083	-5.23898
83	999.0534651	0.04158335	45.9693	126	435.1203292	0.013749421	-0.0200782
84	1006.290031	0.188542169	46.5165	127	444.8431303	0.014075861	50.5109
85	1078.655686	0.084747376	41.6954	128	449.6613637	0.002330215	31.1688
86	1100.12287	0.036169212	-0.837736	129	455.9715325	0.014636435	22.6279
87	1125.732164	0.01008119	48.3053	130	462.0362788	0.012713719	48.639
88	1131.358448	0.017110393	-12.7126	131	468.9187765	0.006004536	24.4761
89	1148.01419	0.027605371	55.8276	132	474.1182391	0.013918247	10.4716
90	1149.488664	0.090811072	121.038	133	479.0897402	0.00265217	43.4907
91	1154.600822	0.013414735	29.3047	134	486.2739231	0.005684834	26.0784
92	1157.966892	0.060280119	44.8991	135	490.9097873	0.007735884	13.2183
93	1166.736135	0.052618646	92.621	136	494.6609668	0.013907035	7.49035
94	1176.456026	0.050767935	22.0927	137	498.9670143	0.003996275	46.8993
95	1281.163115	0.01033406	15.3789	138	500.110702	0.003255555	48.0745
96	1292.638795	0.010132867	53.7258	139	502.011028	0.004187643	47.0232
97	320.8223657	0.016637958	49.3461	140	504.6447111	0.004322725	40.4018
98	322.3579532	0.007276593	49.4722	141	507.3860695	0.000497564	48.5309
99	324.2485787	0.015818431	47.9926	142	509.4697348	0.00423717	31.9123
100	327.9017833	0.050276451	39.8964	143	517.9091611	0.008717498	39.2362
101	331.0010898	0.021654174	38.5162	144	529.3547693	0.004351995	48.7727
102	332.9508883	0.011502552	38.6317	145	536.0500474	0.00142965	47.1209
103	335.5845714	0.029898863	27.6714	146	537.2364174	0.009505492	37.4944
104	338.1173693	0.011155758	27.8824	147	545.6855442	0.002287438	28.0614
105	344.9639751	0.010813568	10.9759	148	548.2707248	0.003514464	18.7012
106	349.1022042	0.016412857	1.73954	149	556.9390826	0.003690082	-3.5269
107	356.5191988	0.026773905	-0.867621	150	564.7586476	0.010766294	-0.875908
108	358.6426361	0.020807652	-0.430398	151	570.1841317	0.015278102	-0.2994
109	365.9771766	0.043805898	-0.150228	152	572.1804925	0.001544475	10.8622

Table A.2. The coefficients of all the component Gaussian functions of the LSFC-Raman (continued)

	V_n	i_n	W_n		V_n	i_n	W_n
153	583.0925737	0.007670585	6.89343	194	983.0670576	0.000231896	52.0567
154	589.1223983	0.004372263	48.3424	195	996.279125	0.090394531	95.2189
155	592.7368009	0.009892734	99.2223	196	1012.779658	0.049889164	70.8919
156	593.8572075	0.029869582	96.0045	197	1027.485601	0.010041336	126.439
157	601.3440456	0.000990624	67.268	198	1100.675798	0.00327357	55.4543
158	607.9578397	0.009831953	61.2659	199	1124.888221	0.011378681	47.5242
159	614.6453575	0.003352366	51.8519	200	1129.02063	0.021645139	37.8347
160	624.9589185	0.073540398	273.845	201	1132.047183	0.033471844	0.0100581
161	632.3953141	0.003525719	14.6368	202	1140.360503	0.010554659	68.977
162	638.0827114	0.108849403	0.30183	203	1143.173645	0.019272113	75.5075
163	648.2740462	0.002208641	5.41634	204	1145.870381	0.030873718	82.36
164	651.8574072	0.021406541	258.26	205	1195.439885	0.009305122	91.3088
165	655.693951	0.006234186	105.86	206	1198.185124	0.002255926	54.042
166	660.6363507	0.006436809	54.7303	207	1219.623207	0.022728082	114.893
167	663.1235563	0.002442787	56.4731	208	1256.853687	0.012538145	94.2841
168	667.1725408	0.002812026	55.8045	209	1343.110444	0.010203434	50.0122
169	672.5068403	0.004944114	63.9215	210	1351.33646	0.001344094	50
170	678.559946	0.002132099	85.1029	211	318.2788972	0.06832678	49.0097
171	680.340956	0.001123456	79.9952	212	319.1480611	0.071516812	48.5671
172	682.7912998	0.004818034	108.049	213	321.1104702	0.021021071	48.9915
173	686.3707806	0.005862694	124.682	214	321.6866793	0.042580589	47.7604
174	696.8065677	0.001765113	79.2878	215	322.6324771	0.016089807	48.6499
175	700.3666476	0.004052561	95.2255	216	325.2079572	0.052715518	43.4095
176	708.670267	0.003210524	51.1338	217	327.2964727	0.047039957	40.6689
177	724.7430089	0.005804166	49.9891	218	328.192798	0.022928467	42.3344
178	728.3622617	0.001749351	49.9825	219	330.7255959	0.024490261	37.7416
179	739.790409	0.000184616	49.9309	220	331.4764138	0.072646743	31.3815
180	744.938459	0.002336975	48.2981	221	334.9821709	0.023034784	29.6088
181	755.4780414	0.00099963	55.1074	222	337.1948527	0.022051202	25.1528
182	757.6509512	0.00250358	72.2682	223	337.9602214	0.122677239	7.16632
183	763.4402036	0.003233034	82.3848	224	340.3397516	0.032857466	16.9752
184	764.9903419	0.002165864	72.6246	225	340.4192956	0.119792991	-5.07586
185	777.7406659	0.004730236	43.7547	226	342.784275	0.032923964	11.4387
186	782.5113669	0.006312982	56.3912	227	344.3033718	0.047611466	6.11604
187	794.6049678	0.031695531	155.641	228	345.7235235	0.004213513	19.6796
188	799.3388069	0.028000965	-0.0256598	229	348.8761828	0.071244411	-2.62248
189	810.8261272	0.004320472	-1.26627	230	349.6299108	0.006493084	-1.01231
190	825.5844527	0.00329608	39.5314	231	351.2072105	0.005296816	12.9894
191	870.0311278	0.004903589	49.9038	232	351.6010504	0.037489623	-0.449817
192	906.8464275	0.00160751	58.0688	233	352.6787748	0.065189893	0.0955639
193	958.2726051	0.026017402	47.1513	234	354.7905715	0.125734276	0.133988

Table A.2. The coefficients of all the component Gaussian functions of the LSFC-Raman (continued)

	v_n	i_n	w_n		v_n	i_n	w_n
235	356.3533204	0.010666726	4.11612	276	465.0055988	0.020456186	-0.0428331
236	358.9433513	0.054489865	-0.340867	277	468.9827997	0.014607758	13.6335
237	361.2268466	0.050907788	0.0455184	278	472.8843368	0.068160669	0.0593148
238	363.1262026	0.040088117	0.0797467	279	473.6312745	0.029953188	-2.73557
239	365.9936674	0.043205242	0.213774	280	476.9459319	0.017744645	0.489291
240	368.8135998	0.008872322	11.2702	281	478.985945	0.04295928	-0.190928
241	369.2578823	0.00853337	16.7246	282	482.9941874	0.069908577	0.260014
242	370.4112706	0.063634802	0.497872	283	486.9093052	0.075690427	-16.2953
243	372.8373631	0.083213775	0.508112	284	490.7904713	0.060756963	12.2882
244	374.5291286	0.033714729	-24.5804	285	492.6966175	0.095276077	-0.148574
245	376.9717119	0.072241346	-19.7965	286	495.6310158	0.060079164	-0.0846453
246	380.7209513	0.004446123	32.4706	287	497.4537378	0.014335276	37.5631
247	381.2108261	0.033568647	27.4211	288	499.4617393	0.034459025	-0.592939
248	383.8988318	0.07864785	-23.0602	289	504.4089892	0.068386601	1.41099
249	387.7596269	0.135749829	-38.0644	290	506.6527125	0.121733449	8.16367
250	388.3125548	0.087407152	-38.6507	291	508.621912	0.040819328	14.0959
251	392.0889556	0.05991973	0.0648294	292	511.9530602	0.03780876	19.8163
252	392.850444	0.184138706	-45.3919	293	513.4003733	0.011783224	26.3422
253	393.5052271	0.028757026	-4.63374	294	517.09529	0.059461187	27.53
254	395.879907	0.03844009	0.147202	295	520.3701754	0.030484905	35.9994
255	399.9415022	0.03093677	3.05876	296	521.0957721	0.109531475	32.5373
256	403.0398387	0.017963955	0.174297	297	523.7604967	0.027846352	42.2872
257	405.0148585	0.081419399	-0.0400162	298	525.4813636	0.01515272	46.2669
258	406.4612015	0.029541115	0.661831	299	527.0305318	0.014388448	47.0401
259	407.6359309	0.049651805	0.608922	300	531.7410898	0.020024189	43.1396
260	409.0871242	0.21140714	0.0293623	301	532.2484254	0.011224988	44.4618
261	412.0283128	0.090424397	-0.31229	302	536.8028055	0.016601521	35.5673
262	416.6903682	0.034904482	0.258849	303	540.910963	0.083453061	24.7042
263	423.1916366	0.030245619	0.0495917	304	543.1139443	0.020044112	24.0488
264	423.575776	0.048262825	0.112991	305	545.4614628	0.014747323	20.7489
265	427.2027893	0.046308747	-0.0305327	306	546.59351	0.028597324	17.78
266	431.8929762	0.024742793	0.249696	307	548.9080469	0.020834984	14.6044
267	433.8146432	0.139444872	0.0318339	308	552.2430754	0.008367232	10.3201
268	434.027084	0.032372218	-0.257296	309	554.7584125	0.004186941	-1.31898
269	434.206543	0.013883357	-0.740546	310	556.8702091	0.049884414	0.936362
270	437.4047946	0.049246408	-0.204362	311	561.4168288	0.005795257	0.206295
271	439.8046958	0.067728565	-0.25903	312	564.252282	0.051665437	-0.0787971
272	441.491611	0.017698123	0.147679	313	565.4454423	0.057533815	0.0774078
273	449.0259816	0.105258247	-0.200861	314	569.7631304	0.006081037	-0.0744467
274	458.5314918	0.058298141	0.173001	315	571.3530407	0.015617939	0.313432
275	459.9691044	0.010806291	41.9531	316	576.4962405	0.012839927	0.093404

Table A.2. The coefficients of all the component Gaussian functions of the LSFC-Raman (continued)

	V_n	i_n	W_n		V_n	i_n	W_n
317	580.2338393	0.049425872	-3.83456	360	748.4713775	0.016076508	105.516
318	585.3974101	0.057075273	11.3331	361	759.4562123	0.009503679	120.32
319	586.7671193	0.082994252	111.225	362	766.1107485	0.004326506	85.5787
320	588.9031672	0.158126523	103.793	363	766.4366849	0.024530133	112.486
321	597.0409083	0.012992792	90.3396	364	776.4475906	0.013192179	39.7155
322	601.0394503	0.026889475	82.3466	365	779.6720335	0.010832864	47.6548
323	606.8733249	0.0073637	64.3783	366	787.2141645	0.00440625	64.3673
324	618.7709759	0.017492086	48.2889	367	793.8551199	0.022549643	109.445
325	619.4635909	0.008480198	47.0697	368	794.7378645	0.016216073	92.1433
326	621.7490264	0.006951653	43.2409	369	800.9151366	0.02347343	1.5574
327	629.3590608	0.012707011	0.0961634	370	805.6916578	0.000844033	42.4703
328	632.0043844	0.018555439	-0.0765687	371	817.5699078	0.004127119	35.2307
329	632.6669278	0.037961518	0.105796	372	846.7189102	0.007170963	77.6706
330	634.4372673	0.049904176	-0.195224	373	870.2086468	0.00246564	49.961
331	636.8798507	0.021167286	0.0556218	374	890.2993316	0.000525029	49.0639
332	638.6967524	0.024769392	0.279931	375	921.2312841	0.11779912	69.6282
333	640.053851	0.013790313	0.565263	376	949.3035321	0.166115091	85.9556
334	640.5650668	0.027640448	-0.0475146	377	971.4361701	0.022091074	22.7592
335	644.5859199	0.029979894	-0.305354	378	977.5474788	0.25687171	-0.509682
336	647.1439391	0.128492472	0.0993015	379	1029.289892	0.012447829	137.659
337	647.7735009	0.233265471	0.384292	380	1049.389308	0.032585065	49.782
338	652.842007	0.033754788	-0.00161887	381	1054.714877	0.034133479	49.9742
339	656.6513894	0.015857198	220.936	382	1069.517824	0.038194127	49.703
340	660.9254253	0.037130694	56.5491	383	1071.157207	0.11948053	48.3591
341	671.2001843	0.003322975	61.3468	384	1074.241963	0.051931429	47.5786
342	676.7847564	0.001395645	75.7454	385	1086.939905	0.18633848	24.1592
343	688.576672	0.008334009	136.896	386	1090.034361	0.003582157	41.0141
344	690.4954289	0.006021216	142.76	387	1104.914912	0.079285856	0.12898
345	692.3433723	0.005230344	146.562	388	1126.84772	0.076873503	53.3795
346	696.9084229	0.008606491	173.689	389	1176.873147	0.100725704	71.9091
347	697.939585	0.00368185	125.094	390	1193.858705	0.063196022	52.4655
348	698.6438405	0.0044129	135.325	391	1200.028217	0.065415825	-11.0473
349	704.0926058	0.004771776	65.8236	392	1204.286732	0.081459191	0.123424
350	706.0705357	0.011643658	87.2223	393	1220.457449	0.001674774	53.1016
351	709.4278753	0.013205452	55.2221	394	1251.702727	0.079478674	108.605
352	713.955094	0.018183264	50.7722	395	1262.014348	0.092332007	92.2636
353	717.0000778	0.017232904	50.1576	396	1265.331916	0.026211543	74.21
354	727.6715868	0.022616087	49.821	397	1266.040051	0.071483697	66.637
355	730.6282962	0.009669817	49.7477	398	1270.288866	0.092883486	0.0900421
356	731.4518678	0.018940914	49.3471	399	1290.184571	0.074999275	0.00236825
357	736.1507851	0.008387154	48.6932	400	1291.736649	0.03938388	53.0961
358	743.4067516	0.032000204	34.1044	401	1293.385733	0.104288018	69.4383
359	743.6647847	0.025061796	36.2792	402	1300.234279	0.09579444	0.366179

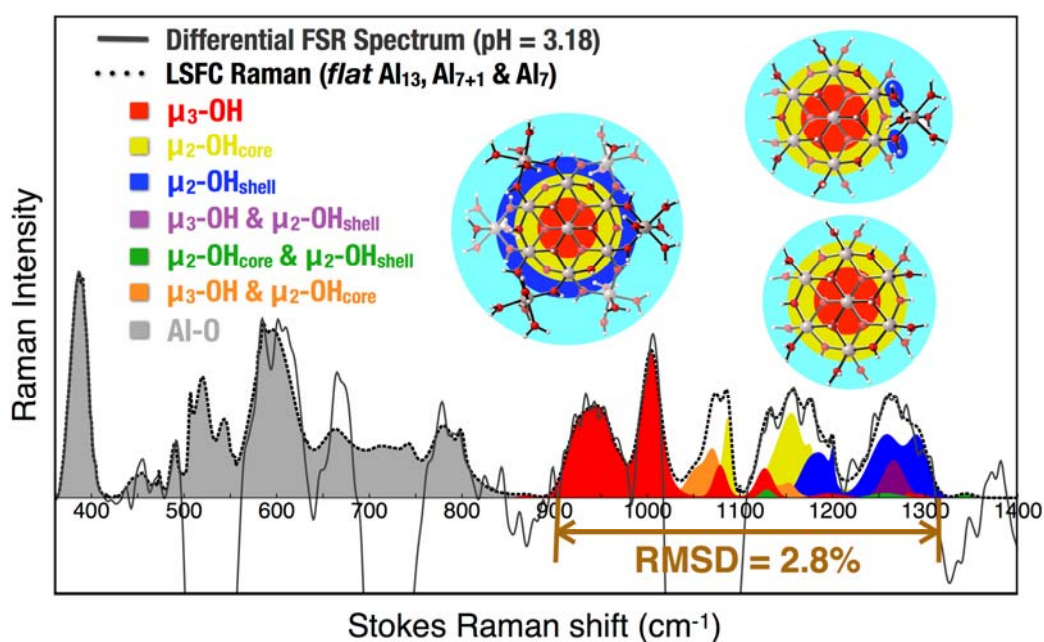


Figure A.5. The experimental differential FSR spectrum (pH = 3.18) and the LSFC Raman spectrum, composing 402 Raman vibrational modes, generated from the computed Raman vibrational frequencies and intensities of *flat* Al₁₃ (192 vibrational modes), Al₇₊₁ (114 vibrational modes) and Al₇ (96 vibrational modes). In addition, the Raman contributions of each hydroxyl ligands in each polycation are also shown. The RMSD between the LSFC Raman and differential FSR spectrum (positive peaks) spectra are 4.5% for 350~1305 cm⁻¹ and 2.8% for 907~1300 cm⁻¹. In the LSFC Raman spectrum, a universal scaling factor (0.9700) is used to modulate the frequencies of all the species and three intensity scaling factors are used for *flat* Al₁₃ (0.066459), Al₇₊₁ (0.022514) and Al₇ (0.057475), respectively. The normalized factor for the experimental differential FSR spectrum is 0.000235.

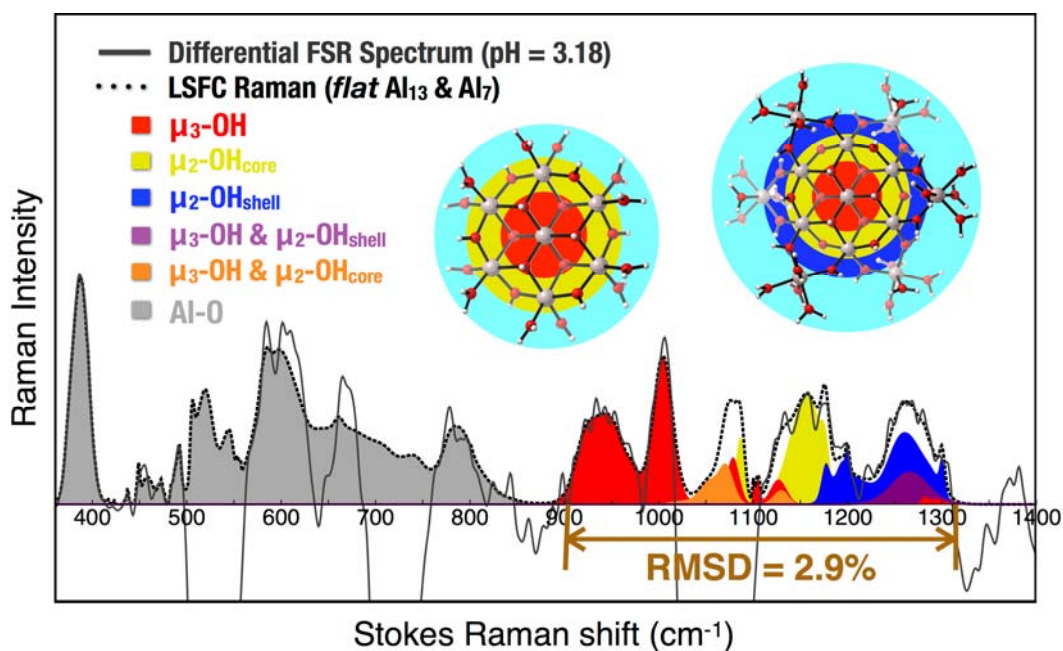


Figure A.6. The experimental differential FSR spectrum (pH = 3.18) and the LSFC Raman spectrum, composing 288 Raman vibrational modes, generated from the computed Raman vibrational frequencies and intensities of *flat* Al_{13} (192 vibrational modes) and Al_7 (96 vibrational modes). In addition, the Raman contributions of each hydroxyl ligands in each polycation are also shown. The RMSD between the LSFC Raman and differential FSR spectrum (positive peaks) spectra are 4.9% for 350~1305 cm^{-1} and 2.9% for 907~1300 cm^{-1} . In the LSFC Raman spectrum, a universal scaling factor (0.9700) is used to modulate the frequencies of all the species and two intensity scaling factors are used for *flat* Al_{13} (0.054674) and Al_7 (0.081381), respectively. The normalized factor for the experimental differential FSR spectrum is 0.000235.

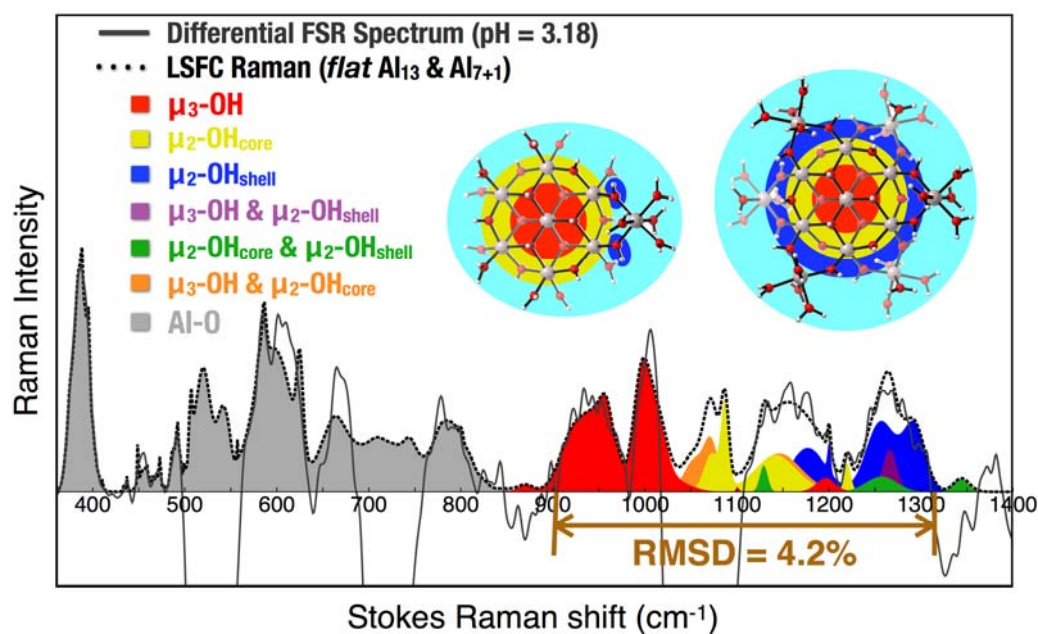


Figure A.7. The experimental differential FSR spectrum (pH = 3.18) and the LSFC Raman spectrum, composing 306 Raman vibrational modes, generated from the computed Raman vibrational frequencies and intensities of *flat* Al₁₃ (192 vibrational modes) and Al₇₊₁ (114 vibrational modes). In addition, the Raman contributions of each hydroxyl ligands in each polycation are also shown. The RMSD between the LSFC Raman and differential FSR spectrum (positive peaks) spectra are 4.9% for 350~1305 cm⁻¹ and 4.2% for 907~1300 cm⁻¹. In the LSFC Raman spectrum, a universal scaling factor (0.9702) is used to modulate the frequencies of all the species and two intensity scaling factors are used for *flat* Al₁₃ (0.074789) and Al₇₊₁ (0.072037), respectively. The normalized factor for the experimental differential FSR spectrum is 0.000235.

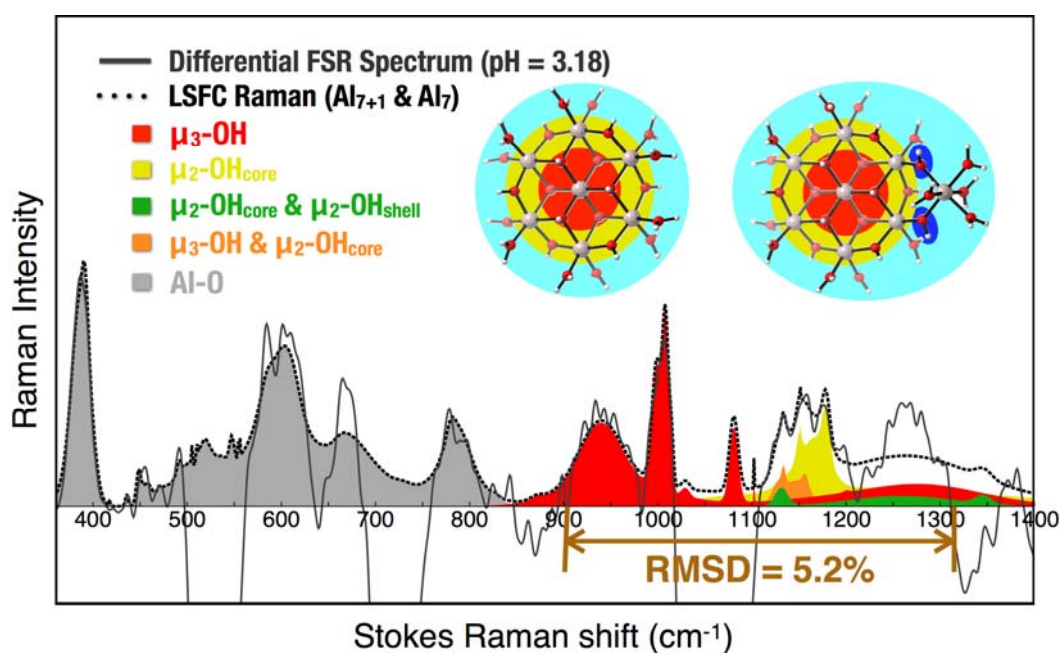


Figure A.8. The experimental differential FSR spectrum (pH = 3.18) and the LSFC Raman spectrum, composing 210 Raman vibrational modes, generated from the computed Raman vibrational frequencies and intensities of Al_{7+1} (114 vibrational modes) and Al_7 (96 vibrational modes). In addition, the Raman contributions of each hydroxyl ligands in the polycation are also shown. The RMSD between the LSFC Raman and differential FSR spectrum (positive peaks) spectra are 5.7% for 350~1305 cm^{-1} and 5.2% for 907~1300 cm^{-1} . In the LSFC Raman spectrum, a universal scaling factor (0.9719) is used to modulate the frequencies of all the species and two intensity scaling factors are used for Al_{7+1} (0.047637) and Al_7 (0.128482), respectively. The normalized factor for the experimental differential FSR spectrum is 0.000235.

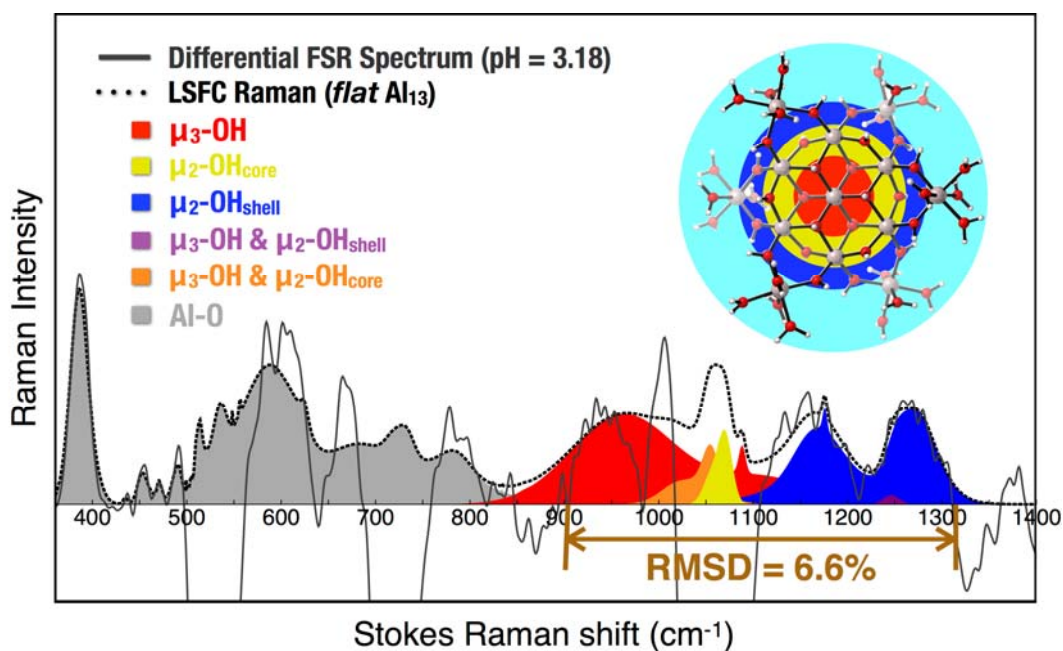


Figure A.9. The experimental differential FSR spectrum (pH = 3.18) and the LSFC Raman spectrum generated from the computed Raman vibrational frequencies and intensities of *flat* Al_{13} (192 Raman vibrational modes). In addition, the Raman contributions of each hydroxyl ligands in the polycation are also shown. The RMSD between the LSFC Raman and differential FSR spectrum (positive peaks) spectra are 7.3% for 350~1305 cm^{-1} and 6.6% for 907~1300 cm^{-1} . In the LSFC Raman spectrum, two universal scaling factors are used to modulate the computed Raman frequencies (0.9555) and intensities (0.059155) of *flat* Al_{13} . The normalized factor for the experimental differential FSR spectrum is 0.000235.

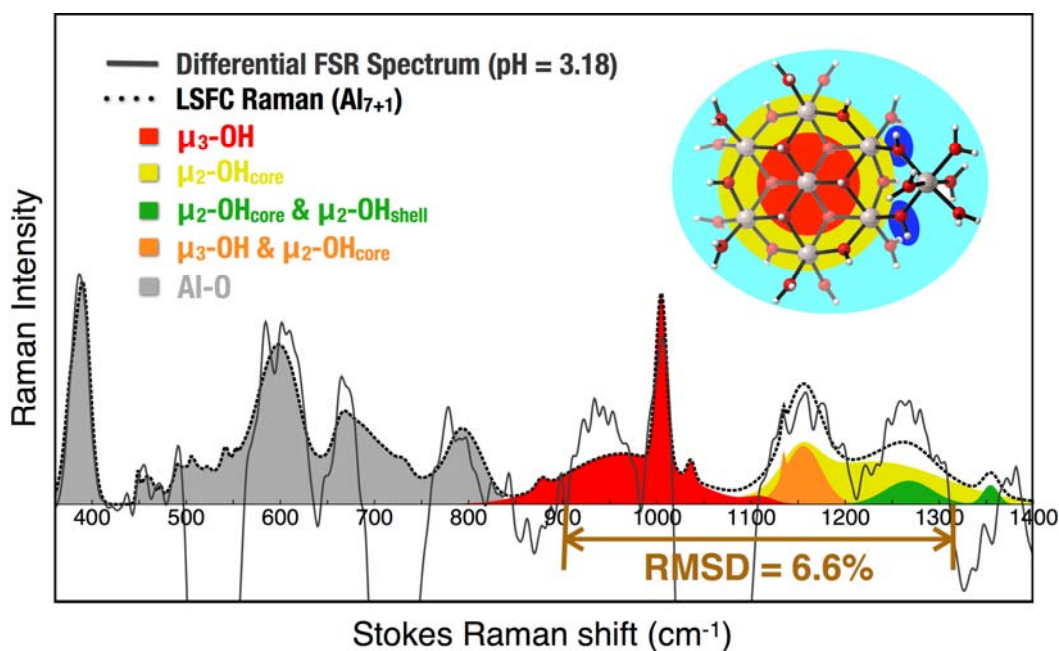


Figure A.10. The experimental differential FSR spectrum (pH = 3.18) and the LSFC Raman spectrum generated from the computed Raman vibrational frequencies and intensities of Al_{7+1} (114 Raman vibrational modes). In addition, the Raman contributions of each hydroxyl ligands in the polycation are also shown. The RMSD between the LSFC Raman and differential FSR spectrum (positive peaks) spectra are 6.3% for 350~1305 cm^{-1} and 6.6% for 907~1300 cm^{-1} . In the LSFC Raman spectrum, two universal scaling factors are used to modulate the computed Raman frequencies (0.9783) and intensities (0.108066) of Al_{7+1} . The normalized factor for the experimental differential FSR spectrum is 0.000235.

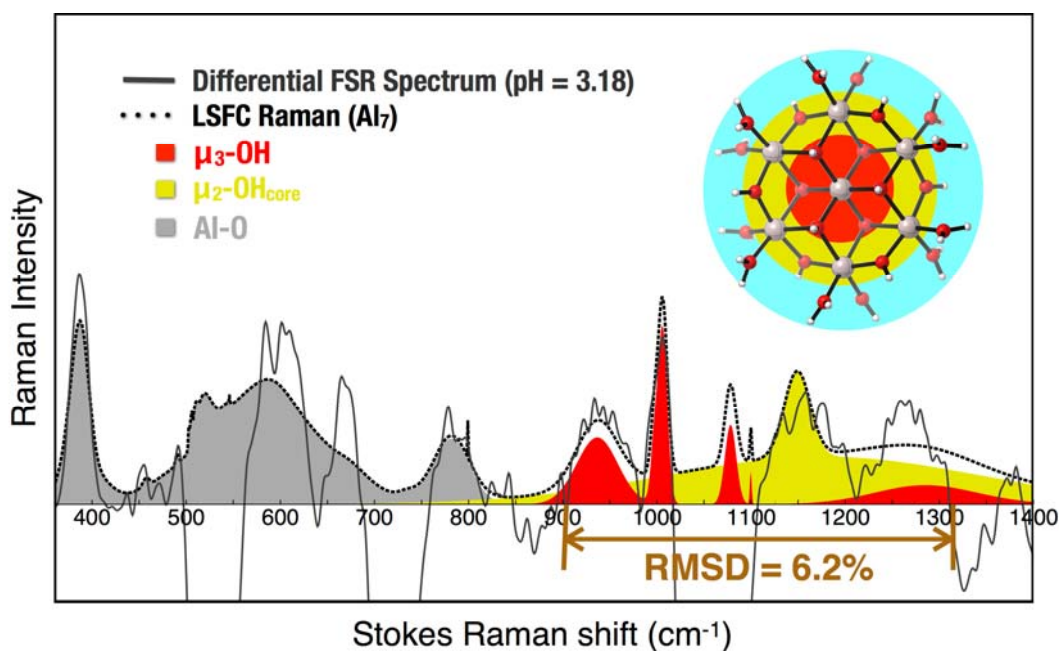


Figure A.11. The experimental differential FSR spectrum (pH = 3.18) and the LSFC Raman spectrum generated from the computed Raman vibrational frequencies and intensities of Al_7 (96 Raman vibrational modes). In addition, the Raman contributions of each hydroxyl ligands in the polycation are also shown. The RMSD between the LSFC Raman and differential FSR spectrum (positive peaks) spectra are 7.9% for 350~1305 cm^{-1} and 6.2% for 907~1300 cm^{-1} . In the LSFC Raman spectrum, two universal scaling factors are used to modulate the computed Raman frequencies (0.9697) and intensities (0.137532) of Al_7 . The normalized factor for the experimental differential FSR spectrum is 0.000235.

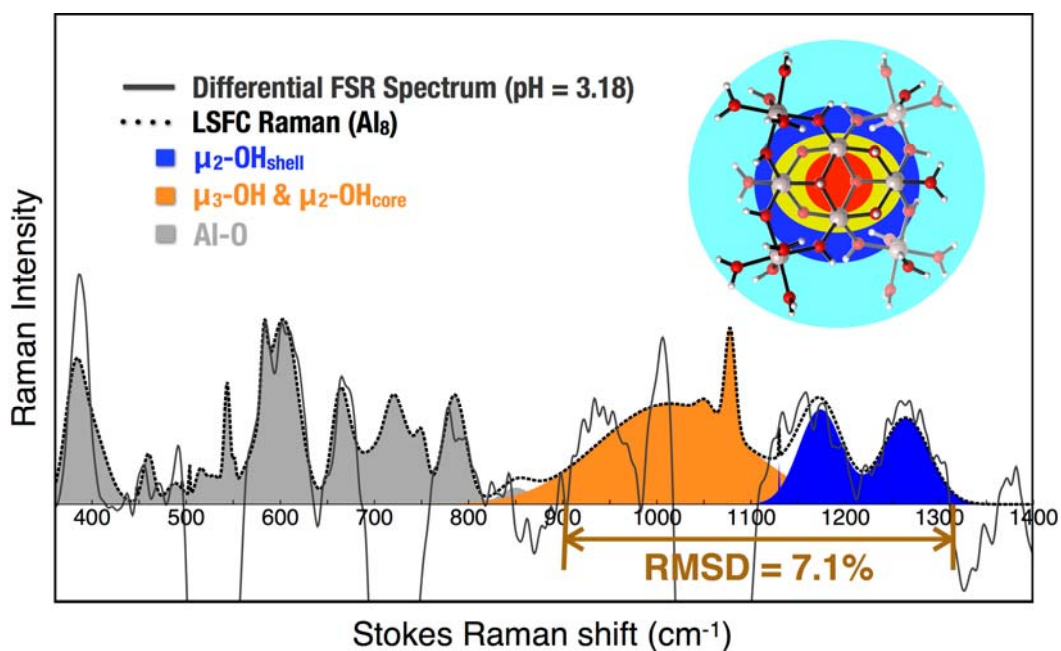


Figure A.12. The experimental differential FSR spectrum (pH = 3.18) and the LSFC Raman spectrum generated from the computed Raman vibrational frequencies and intensities of Al_8 (67 Raman vibrational modes). In addition, the Raman contributions of each hydroxyl ligands in the polycation are also shown. The RMSD between the LSFC Raman and differential FSR spectrum (positive peaks) spectra are 6.8% for 350~1305 cm^{-1} and 7.1% for 907~1300 cm^{-1} . In the LSFC Raman spectrum, two universal scaling factors are used to modulate the computed Raman frequencies (0.9538) and intensities (0.095485) of Al_8 . The normalized factor for the experimental differential FSR spectrum is 0.000235.

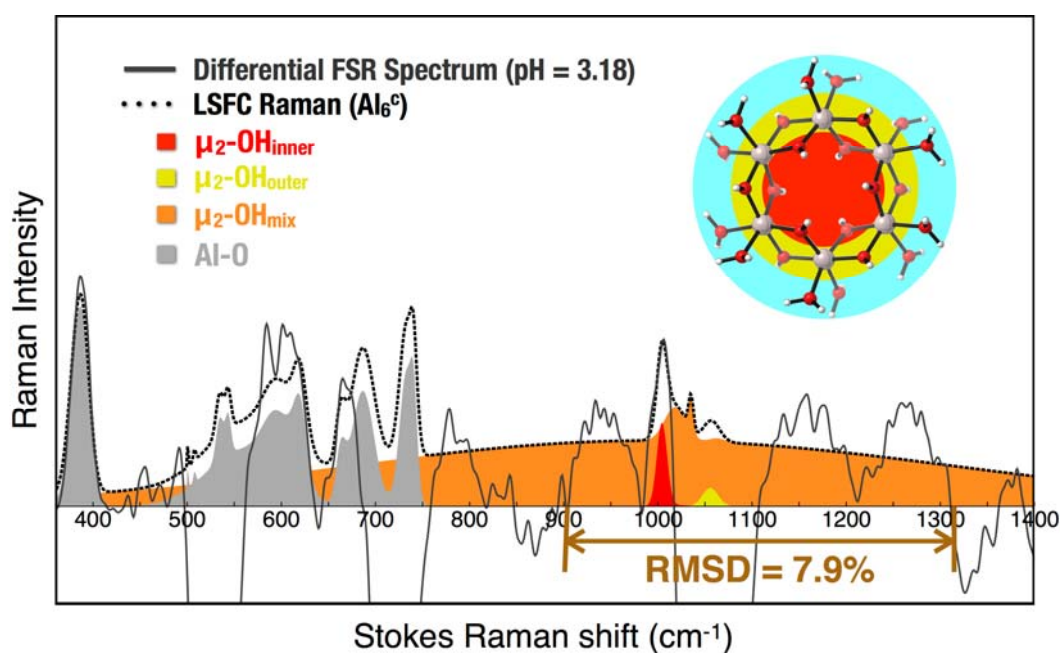


Figure A.13. The experimental differential FSR spectrum (pH = 3.18) and the LSFC Raman spectrum generated from the computed Raman vibrational frequencies and intensities of Al_6^c (73 Raman vibrational modes). In addition, the Raman contributions of each hydroxyl ligands in the polycation are also shown. The RMSD between the LSFC Raman and differential FSR spectrum (positive peaks) spectra are 8.0% for 350~1305 cm^{-1} and 7.9% for 907~1300 cm^{-1} . In the LSFC Raman spectrum, two universal scaling factors are used to modulate the computed Raman frequencies (0.9809) and intensities (0.072053) of Al_6^c . The normalized factor for the experimental differential FSR spectrum is 0.000235.

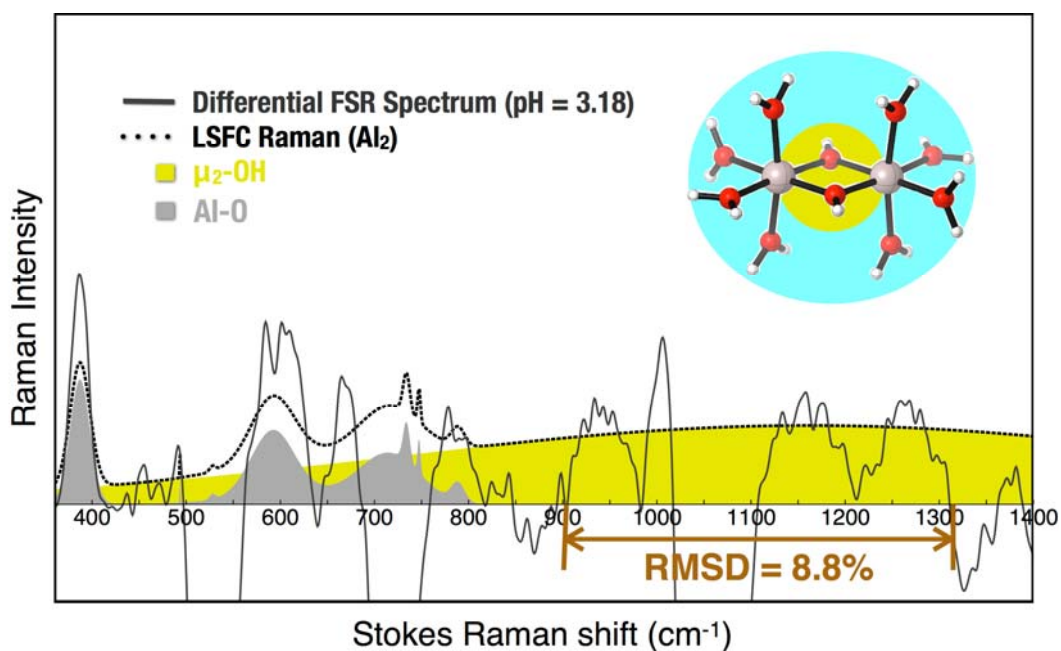


Figure A.14. The experimental differential FSR spectrum (pH = 3.18) and the LSFC Raman spectrum generated from the computed Raman vibrational frequencies and intensities of Al₂ (17 Raman vibrational modes). The RMSD between the LSFC Raman and differential FSR spectrum (positive peaks) spectra are 9.7% for 350~1305 cm⁻¹ and 8.8% for 907~1300 cm⁻¹. In the LSFC Raman spectrum, two universal scaling factors are used to modulate the computed Raman frequencies (1.0347) and intensities (0.115939) of Al₂. The normalized factor for the experimental differential FSR spectrum is 0.000235.

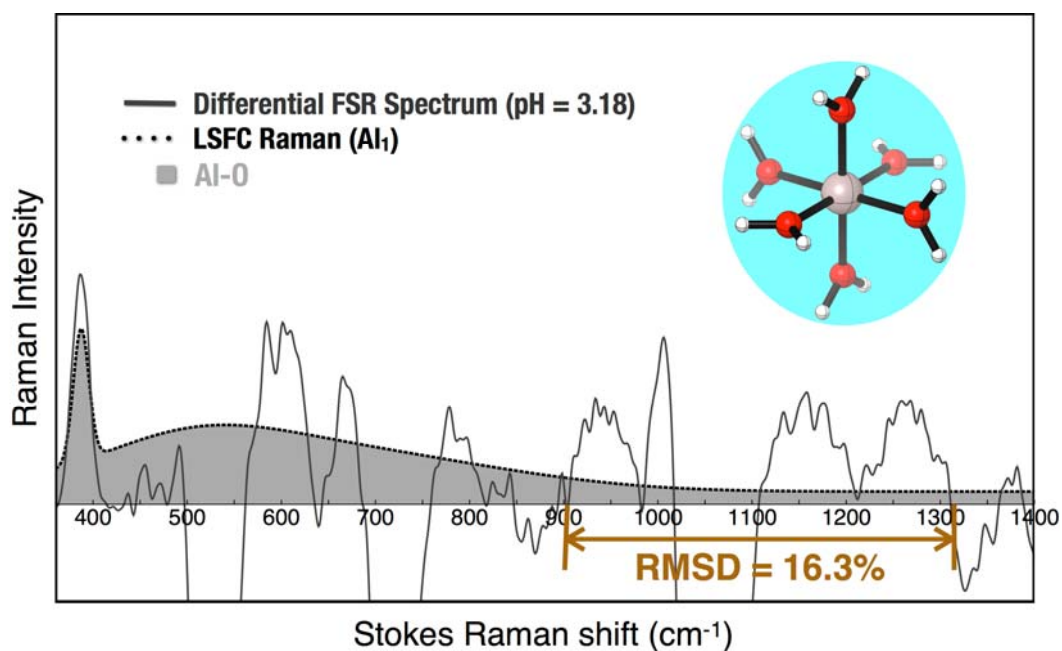


Figure A.15. The experimental differential FSR spectrum (pH = 3.18) and the LSFC Raman spectrum generated from the computed Raman vibrational frequencies and intensities of Al₁ (9 Raman vibrational modes). The RMSD between the LSFC Raman and differential FSR spectrum (positive peaks) spectra are 14.4% for 350~1305 cm⁻¹ and 16.3% for 907~1300 cm⁻¹. In the LSFC Raman spectrum, two universal scaling factors are used to modulate the computed Raman frequencies (1.0325) and intensities (0.086834) of Al₁. The normalized factor for the experimental differential FSR spectrum is 0.000235.

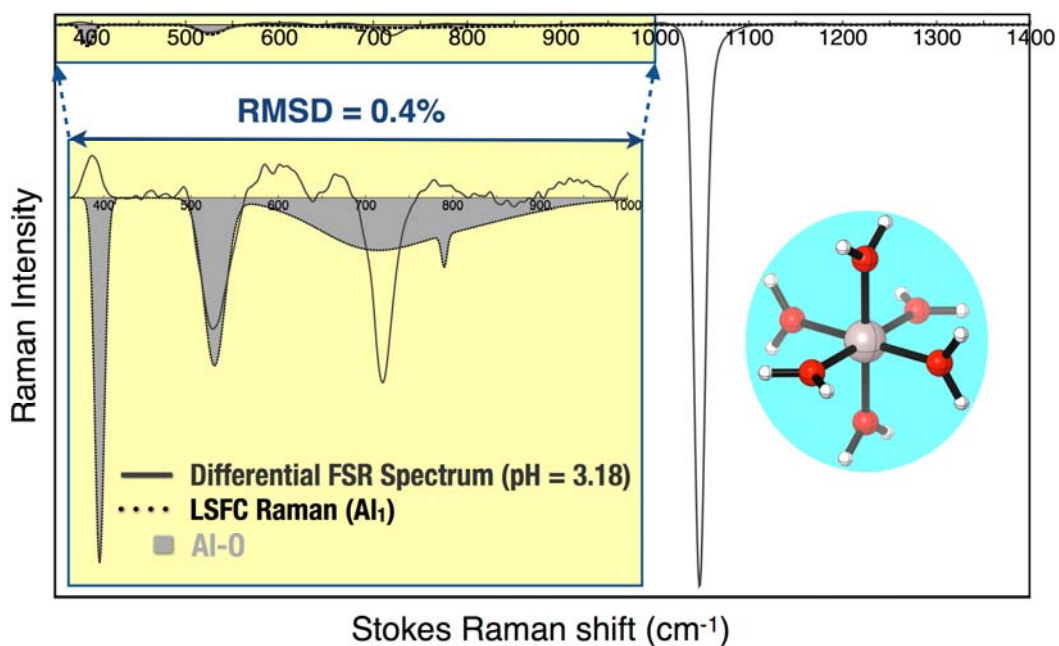


Figure A.16. The experimental differential FSR spectrum (pH = 3.18) and the LSFC Raman spectrum generated from the computed Raman vibrational frequencies and intensities of Al₁ (9 Raman vibrational modes). The RMSD between the LSFC Raman and differential FSR spectrum (negative peaks) spectra are 18.9% for 350~1107 cm⁻¹ and 0.4% for 350~820 cm⁻¹. This figure together with Fig. S15 show that Al₁ is not an emerging species but a consuming species in the electrolysis process. In the LSFC Raman spectrum, two universal scaling factors are used to modulate the computed Raman frequencies (1.0539) and intensities (-0.009743) of Al₁. The normalized factor for the experimental differential FSR spectrum is 0.031701.

Effect of Water Coordination on Raman Spectra:

$[\text{Al}_1 \cdot 12\text{H}_2\text{O}]^{3+}$ and Al_1 structures were both optimized, and the LSFC spectra were computed. The raw computed Raman spectra of $[\text{Al}_1 \cdot 12\text{H}_2\text{O}]^{3+}$ and Al_1 structure (Figure A.17(c)) appear different, i.e. the computed Raman spectra of $[\text{Al}_1 \cdot 12\text{H}_2\text{O}]^{3+}$ have more vibration modes than that of Al_1 . These additional modes are introduced by the vibrations of exogenous waters in $[\text{Al}_1 \cdot 12\text{H}_2\text{O}]^{3+}$ as well as the coherent vibrations of exogenous waters and η -water molecules.

Due to the water exchange between the Al clusters and solvent, the vibration modes corresponding to the exogenous water vibrations cannot be resolved experimentally and therefore they are eliminated by the Least-Square Fitted algorithm in computing LSFC Raman spectrum.

For both of the LSFC Raman spectra generated from $[\text{Al}_1 \cdot 12\text{H}_2\text{O}]^{3+}$ & NO_3^- and from Al_1 & NO_3^- , only the strong Al-O stretching mode at 525 cm^{-1} was preserved. Both of these LSFC Raman spectra reproduced the experimental FSR Raman of 1.0 M precursor $\text{Al}(\text{NO}_3)_3(aq.)$ (pH = 1.90) with insignificant RMSD difference (RMSD = 0.0014 % vs 0.0017%, respectively compared to experiments, Figure A.17).

The vibrational modes corresponding to the skeleton Al-O with exogenous waters and η -water molecules appear at $350\text{-}900 \text{ cm}^{-1}$. Thus, their vibrations do not affect the identification of Al clusters discussed in this work, which primarily focused on $900\text{--}1300 \text{ cm}^{-1}$. Hence, the computed spectral data from isolated Al clusters, without the monomer, is adequate for creating the LSFC spectrum for further spectral analysis.

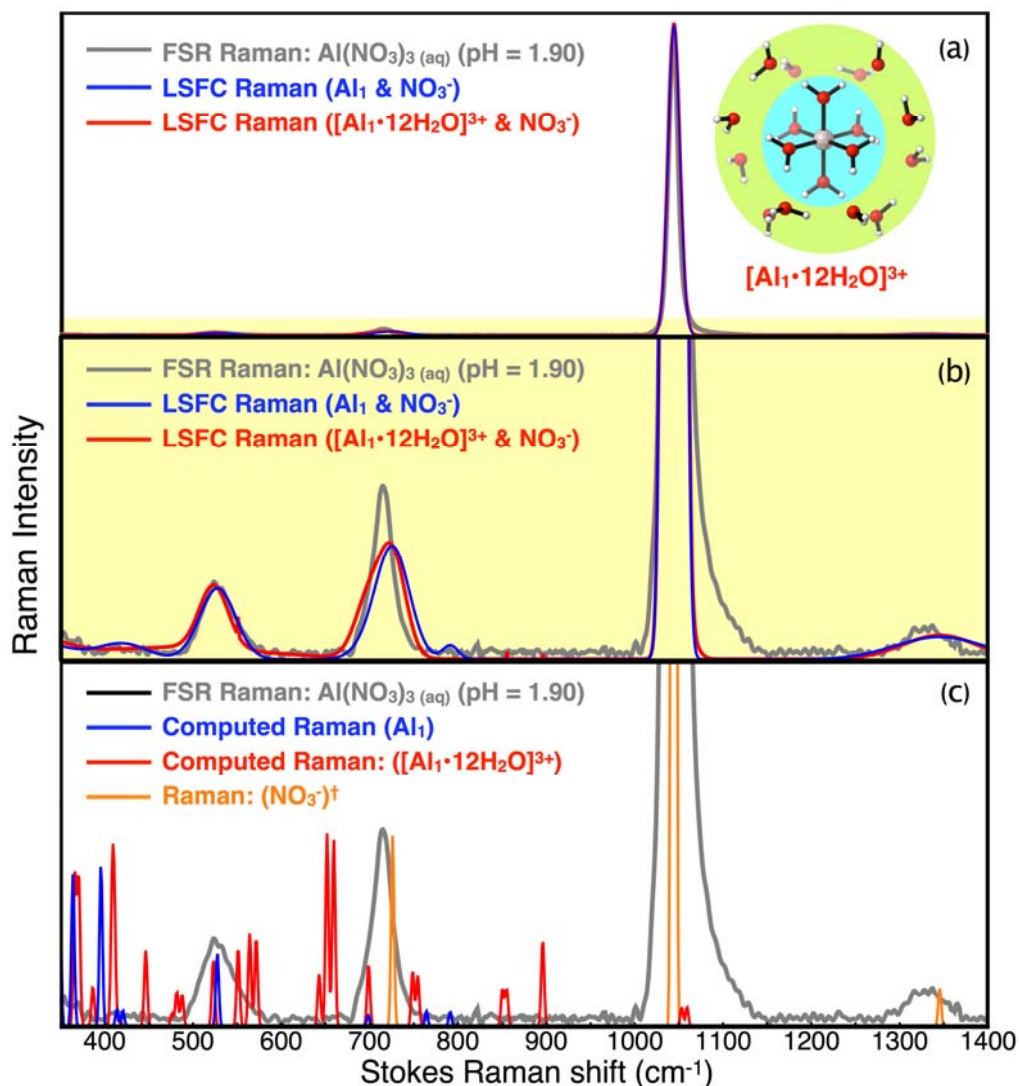


Figure A.17. The FSR spectrum (pH = 1.90) with (a) the computed LSFC Raman spectra, (b) The zooming in of the light yellow region in (a), and (c) the raw computed Raman spectra. The frequency scaling factors for LSFC Raman Spectra of Al₁ & NO₃⁻ and [Al₁·12H₂O]³⁺ & NO₃⁻ are 1.055 and 1.0, respectively. The same frequency scaling factors are used for the computed Raman spectra of Al₁ (1.055) and [Al₁·12H₂O]³⁺ (1.0) in (c). The RMSD for the LSFC Raman spectra generated from the computed spectra of Al₁ & NO₃⁻ and [Al₁·12H₂O]³⁺ & NO₃⁻ are 0.0017% and 0.0014%, respectively. The RMSD is computed by excluding the large nitrate peak at 1000-1150 cm⁻¹.

†The NO₃⁻ Raman spectrum in (c) is obtained by using the fundamental Raman vibrational modes reported by Waterland et al.¹² with the frequency scaling factor of 1.004. The intensities of these nitrate peaks are fitted to reflect the intensity difference caused by the detecting light source.

Full authorship of Gaussian 09

Gaussian 09, Revision B.01, M. J. Frisch, G. W. Trucks, H. B. Schlegel, G. E. Scuseria, M. A. Robb, J. R. Cheeseman, G. Scalmani, V. Barone, B. Mennucci, G. A. Petersson, H. Nakatsuji, M. Caricato, X. Li, H. P. Hratchian, A. F. Izmaylov, J. Bloino, G. Zheng, J. L. Sonnenberg, M. Hada, M. Ehara, K. Toyota, R. Fukuda, J. Hasegawa, M. Ishida, T. Nakajima, Y. Honda, O. Kitao, H. Nakai, T. Vreven, J. A. Montgomery, Jr., J. E. Peralta, F. Ogliaro, M. Bearpark, J. J. Heyd, E. Brothers, K. N. Kudin, V. N. Staroverov, R. Kobayashi, J. Normand, K. Raghavachari, A. Rendell, J. C. Burant, S. S. Iyengar, J. Tomasi, M. Cossi, N. Rega, J. M. Millam, M. Klene, J. E. Knox, J. B. Cross, V. Bakken, C. Adamo, J. Jaramillo, R. Gomperts, R. E. Stratmann, O. Yazyev, A. J. Austin, R. Cammi, C. Pomelli, J. W. Ochterski, R. L. Martin, K. Morokuma, V. G. Zakrzewski, G. A. Voth, P. Salvador, J. J. Dannenberg, S. Dapprich, A. D. Daniels, Ö. Farkas, J. B. Foresman, J. V. Ortiz, J. Cioslowski, and D. J. Fox, Gaussian, Inc., Wallingford CT, 2009.

Reference

- 1 Duca, M. & Koper, M. T. M. Powering denitrification: the perspectives of electrocatalytic nitrate reduction. *Energy Environ. Sci.* **5**, 9726-9742, doi:10.1039/c2ee23062c (2012).
- 2 Wang, W., Wentz, K. M., Hayes, S. E., Johnson, D. W. & Keszler, D. A. Synthesis of the Hydroxide Cluster $[\text{Al}_{13}(\mu_3\text{-OH})_6(\mu\text{-OH})_{18}(\text{H}_2\text{O})_{24}]^{15+}$ from an Aqueous Solution. *Inorg. Chem.* **50**, 4683-4685, doi:10.1021/ic200483q (2011).
- 3 Bi, Z., Feng, C. H., Wang, D. S., Ge, X. P. & Tang, H. X. Transformation of planar Mogel Al-13 to epsilon Keggin Al-13 in dissolution process. *Colloid Surf. A-Physicochem. Eng. Asp.* **407**, 91-98, doi:10.1016/j.colsurfa.2012.05.013 (2012).
- 4 Gatlin, J. T., Mensinger, Z. L., Zakharov, L. N., MacInnes, D. & Johnson, D. W. Facile Synthesis of the Tridecameric Al₁₃ Nanocluster $\text{Al}_{13}(\mu_3\text{-OH})_6(\mu_2\text{-OH})_{18}(\text{H}_2\text{O})_{24}(\text{NO}_3)^{15+}$. *Inorg. Chem.* **47**, 1267-1269 (2008).
- 5 Frontiera, R. R., Fang, C., Dasgupta, J. & Mathies, R. A. Probing structural evolution along multidimensional reaction coordinates with femtosecond

- stimulated Raman spectroscopy. *Phys. Chem. Chem. Phys.* **14**, 405-414, doi:10.1039/c1cp22767j (2012).
- 6 Liu, W., Zhu, L. & Fang, C. Observation of sum-frequency generation induced cascaded four-wave mixing using two crossing femtosecond laser pulses in a 0.1 mm BBO crystal. *Opt. Lett.* **37**, 3783-3785 (2012).
 - 7 McCamant, D. W., Kukura, P., Yoon, S. & Mathies, R. A. Femtosecond broadband stimulated Raman spectroscopy: Apparatus and methods. *Rev. Sci. Instrum.* **75**, 4971-4980, doi:10.1063/1.1807566 (2004).
 - 8 Liu, W., Han, F., Smith, C. & Fang, C. Ultrafast Conformational Dynamics of Pyranine during Excited State Proton Transfer in Aqueous Solution Revealed by Femtosecond Stimulated Raman Spectroscopy. *J. Phys. Chem. B* **116**, 10535-10550, doi:10.1021/jp3020707 (2012).
 - 9 Yoon, S., McCamant, D. W., Kukura, P., Mathies, R. A., Zhang, D. & Lee, S.-Y Dependence of line shapes in femtosecond broadband stimulated Raman spectroscopy on pump-probe time delay. *J. Chem. Phys.* **122**, 024505 doi: 10.1063/1.1828044 (2005).
 - 10 Johansson, G. The Crystal Structures of $[\text{Al}_2(\text{OH})_2(\text{H}_2\text{O})_8](\text{SO}_4)_2 \cdot 2\text{H}_2\text{O}$ and $[\text{Al}_2(\text{OH})_2(\text{H}_2\text{O})_8](\text{SeO}_4)_2 \cdot 2\text{H}_2\text{O}$. *Acta Chemica Scandinavica* **16**, 403-420 (1962).
 - 11 Casey, W. H., Olmstead, M. M., Phillips, B. L. & Phillips, L. A new aluminum hydroxide octamer, $[\text{Al}_8(\text{OH})_{14}(\text{H}_2\text{O})_{18}](\text{SO}_4)_5 \cdot 16\text{H}_2\text{O}$. *Inorganic Chemistry* **44**, 4888-4890 (2005).
 - 12 Waterland, M. R. & Kelley, A. M. Far-ultraviolet resonance Raman spectroscopy of nitrate ion in solution. *J. Chem. Phys.* **113**, 6760-6773, doi:10.1063/1.1310615 (2000).

Appendix B

Some discussion about the synthesis of “flat” Al_{13} compound $[\text{Al}_{13}(\mu_3\text{-OH})_6(\mu\text{-OH})_{18}(\text{H}_2\text{O})_{24}](\text{NO}_3)_{15}\cdot n\text{H}_2\text{O}$ from aqueous solution was made in chapter 2. Here are some more detailed discussions.

The Frost Diagrams for zinc, aluminum, hydrogen, and nitrogen under acidic environment ($\text{pH} = 0$) are shown in Figure B.1.

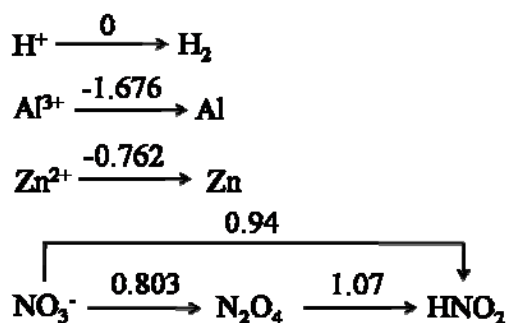
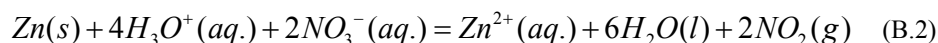
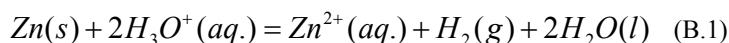


Figure B.1. Frost diagrams for Zn, Al, H, and N at $\text{pH} = 0$

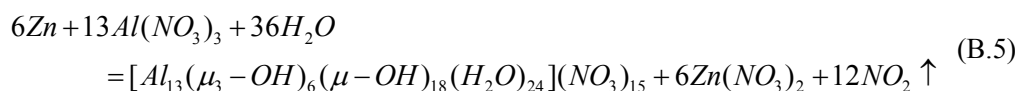
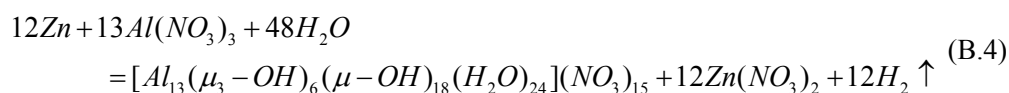
The starting solution (1.6 M $\text{Al}(\text{NO}_3)_3$) has a pH lower than 2 because of the hydrolysis of aluminum cation in aqueous solution, which generates hydroniums and aluminum-aquo/hydroxo species $(\text{Al}(\text{OH})_x(\text{H}_2\text{O})_{6-x}, 0 \leq x \leq 2)$. Aquo ligands are good leaving groups and hydroxo ligands can act as nucleophilic groups, providing prerequisites for further condensation. In this acidic environment, zinc is active enough to reduce both hydronium and nitrate ions. Meanwhile, Al has a more negative reduction potential and therefore Al(III) will not participate in the redox reactions under acidic condition. Depending on what is oxidizing zinc metal, two possible half reaction can be written as (B.1) and (B.2).



Although the kinetic considerations and the inter-conversion of various species renders nitrate reduction systems notoriously complex, it is important to note that all probable Zn oxidation schemes in the present solutions consume at least 2 hydroniums per Zn atom. The net result is a slow increase in solution pH as the Zn is oxidized. When compared to the base titration method, this represents a more controlled and continuous change in pH without introducing locally high hydroxide concentration and severe pH gradients. Increasing solution pH, drives further hydrolysis of Al-bound aquo ligands, increasing the concentration of $\text{Al}(\text{OH})(\text{H}_2\text{O})_5^{2+}$ and $\text{Al}(\text{OH})_2(\text{H}_2\text{O})_4^+$ species. The aluminum aquo-hydroxo species are highly reactive with respect to classical condensation processes such as those described by Jovlivet². According to the Partial Charge Model², the hydroxo groups with partial negative charges attack partially positively charged metal centers forming hydroxo bridges between metal centers and elimination of partial positive charged aquo ligands as shown in (B.3).



This condensation of the mono-aluminum species via oligation results in formation of different aluminum oligomers, which further combine into larger structures such as the “flat” Al_{13} . Combining with (B.1) or (B.2), the balanced overall reaction of producing “flat” Al_{13} cluster, for example, can be written as (B.4) or (B.5).



Although the only crystalline product we have been able to isolate contains the “flat” Al_{13} clusters, various aluminum other oligomers are probably generated along the reaction path of forming the “flat” Al_{13} cluster and equilibrium with each other in the same Zn-Al-nitrate system (some more discussions are made in Chapter 3).

Exploring the solvent and counter ion choices is necessary for potential crystallization and analysis of these other structures.

References

- 1 Wang, W., Wentz, K. M., Hayes, S. E., Johnson, D. W. & Keszler, D. A. Synthesis of the Hydroxide Cluster $\text{Al}_{13}(\mu_3\text{-OH})_6(\mu\text{-OH})_{18}(\text{H}_2\text{O})_{24}^{15+}$ from an Aqueous Solution. *Inorganic Chemistry* **50**, 4683-4685, doi:10.1021/ic200483q (2011).
- 2 Jolivet, J.-P. *Metal oxide chemistry & synthesis: from solution to oxide*. (Wiley, 2000).

Appendix C

It is extremely important to carefully **control the reaction pathway** in chemical synthesis, not only to produce a targeted cluster structure on the molecular level but also for solid thin-film formation on a much larger scale. As mentioned previously, conventional sol-gel based thin-film deposition relies on precursor sols, which are often suspensions of metal oxide/hydroxide particles that are stabilized and dispersed with bulky organic ligands. During sol-gel precursor synthesis, solvent, ligands, and experimental procedures need to be carefully chosen and designed to prevent aggregation of suspended particles and thus kinetically stabilize the sol precursor. Since the species formed are likely to be in a metastable state, the solid-state conversion requires high temperature annealing to overcome the activation energy barrier for expelling the organic ligands and minimizing the residual carbon content. Moreover, high water content is usually employed in some systems, eg. Al(OR)_3 , to promote hydrolysis, which leads to the irreversible formation of oxide/hydroxide particles irreversible.¹ Although a high-temperature post-deposition anneal might assist in sintering the particles, thin films made from these sol precursors are normally porous and exhibit rough surfaces (RMS roughness \gg 1 nm).

In previous contributions,²⁻⁶ directed at production of high quality oxide thin films, we employed a **Prompt Inorganic Condensation (PIC)** approach in which a low-activation energy condensation pathway was tailored for precursor-to-solid conversion. Different from a classic metal-organic colloidal precursor, aqueous solutions containing stable or metastable metal-hydroxo species were generated by (1) hydrolysis and sequential low level condensation due to the careful pH adjustment and (2) coordination with simple, easily decomposed inorganic ligands. Discrete, molecular cluster precursors can be produced through application of these principles. The simple aqueous acid-base chemistry of metal cations, can be manipulated to form a reactive precursor without organic solvents or additives.

These molecular species have a degree of condensation in solution, but not as high as metal oxide colloids. Therefore, they can further condense with each other under proper conditions. In the solution, the counter-ion concentration is intentionally minimized to reduce non functional chemical and also control the ionicity of the solution. Simple techniques, like spin coating, can be used to form a liquid thin film. By curing this thin film at relatively low temperature, cross linking and further condensation of the precursor species will occur because of the decomposition of counter-ion/inorganic-ligand. Coupling with the large surface tension water provides, formation of dense, defect-free, and atomically smooth thin films can be realized. (The thermally induced condensation can be an analog to the solvent induced condensation in sol-gel route. Instead of generating lots of ill controlled nano-particles, our approach only generates one hydroxide/oxide “particle” - in the shape of a continuous thin layer.)

Some **key advantages** of the aqueous PIC approach are summarized here:

First, it is environmentally benign. Comparing to conventional sol-gel precursors, the PIC precursor is an aqueous solution containing simple non-toxic inorganic compounds, which reduce the use harmful organic reagent and solvents. By minimizing non functional chemicals in the system, atom efficiency is significantly improved relative to conventional sol-gel or vapor deposition.

Second, it is suitable for high quality thin-film production. The inorganic aqueous precursor provides an oxygen rich and organic free environment, which prevents the formation of oxygen vacancies and residual carbon. The homogeneous condensation of molecular species in the precursor not only inhibits the formation of voids but also produces atomically smooth surfaces.

Finally, it provides reduced deposition complexity and a highly scalable process. Thin film deposition can be realized by non-vacuum techniques, such as spin coating, mist coating, or printing, which makes large scale production possible.

Reference

- 1 Brinker, C. J. & Scherer, G. W. *Sol-Gel Sci.* 59-78 (Academic Press, 1990).
- 2 Meyers, S. T. *et al.* Aqueous Inorganic Inks for Low-Temperature Fabrication of ZnO TFTs. *J. Am. Chem. Soc.* **130**, 17603-17609, doi:10.1021/ja808243k (2008).
- 3 Meyers, S. T. *et al.* Solution-Processed Aluminum Oxide Phosphate Thin-Film Dielectrics. *Chem. Mater.* **19**, 4023-4029 (2007).
- 4 Anderson, J. T. *et al.* Solution-processed HafSO_x and ZircSO_x inorganic thin-film dielectrics and nanolaminates. *Adv. Funct. Mater.* **17**, 2117-2124, doi:10.1002/adfm.200601135 (2007).
- 5 Jiang, K. *et al.* Low-Energy Path to Dense HfO₂ Thin Films with Aqueous Precursor. *Chem. Mat.* **23**, 945-952, doi:10.1021/cm102082j (2010).
- 6 Jiang, K. *et al.* Low-temperature, solution processing of TiO₂ thin films and fabrication of multilayer dielectric optical elements. *Solid State Sci.* **11**, 1692-1699, doi:10.1016/j.solidstatesciences.2009.05.026 (2009).

Appendix D: Supporting information for Chapter 5

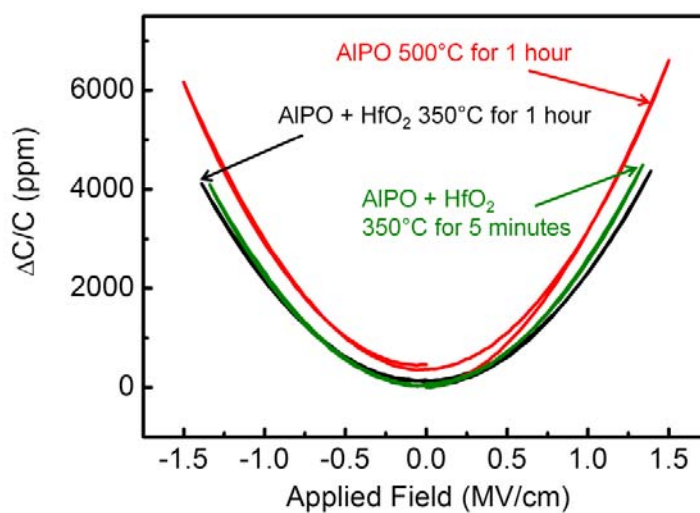


Figure D.1. C-V measurement for AlPO layer with different treatments, indicating the chemically enhanced dehydration effect by adding HfO₂ layer occurs after 5 minutes anneal at 350 °C. The C-V curve for a bare AlPO layer annealed at 500 °C for one hour is shown for comparison.

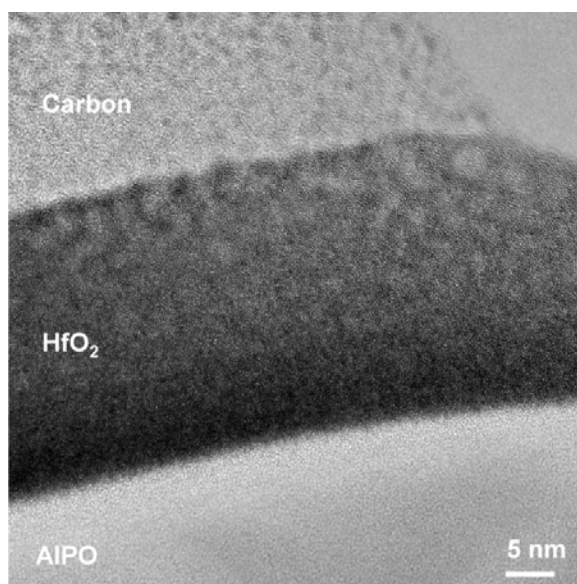


Figure D.2. High resolution TEM image of the cross section of an AlPO-HfO₂ stack annealed at 350 °C for 5 minutes.

Table D.1. Thickness data (from spectroscopic ellipsometry) of AlPO and HfO₂ layer in both individual layer and the AlPO-HfO₂ stack after one hour anneal at 350 °C. This shows the HfO₂ does not necessarily facilitate the densification of AlPO layer at low temperature even as it promotes the dehydration of AlPO.

	AlPO	HfO ₂
Layer thickness of individual material (nm)	267.75	26.16
Layer thickness in AlPO-HfO ₂ stack (nm)	265.05	27.46

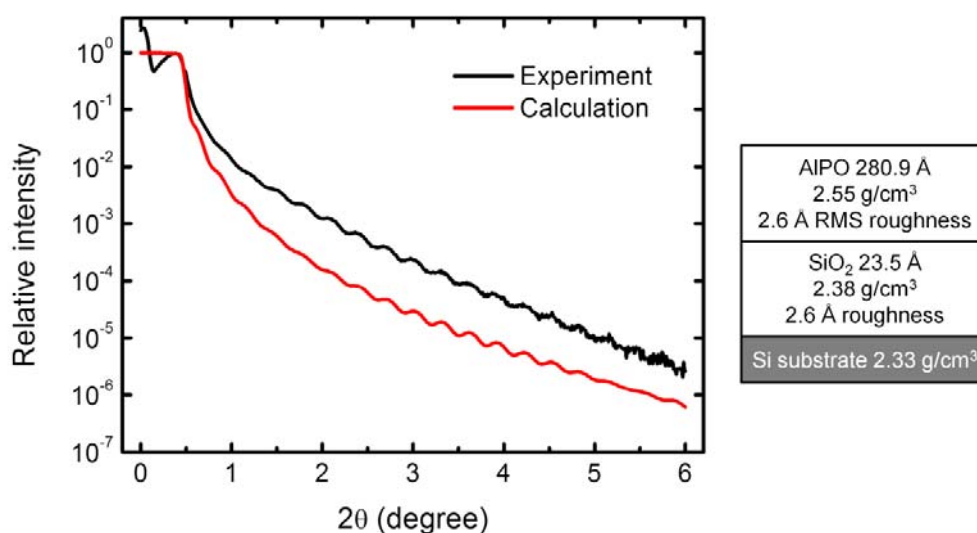


Figure D.3. X-ray reflectivity (XRR) spectrum of a ~30 nm AlPO layer on silicon wafer after one hour anneal 350 °C. The calculated spectrum was generated by assuming a homogeneous AlPO layer. Although the critical angle and the amplitude of Kiessig fringes are consistent between the experimental and calculated spectra, the overall fit is not good. This indicates a possible missing component in the sample.

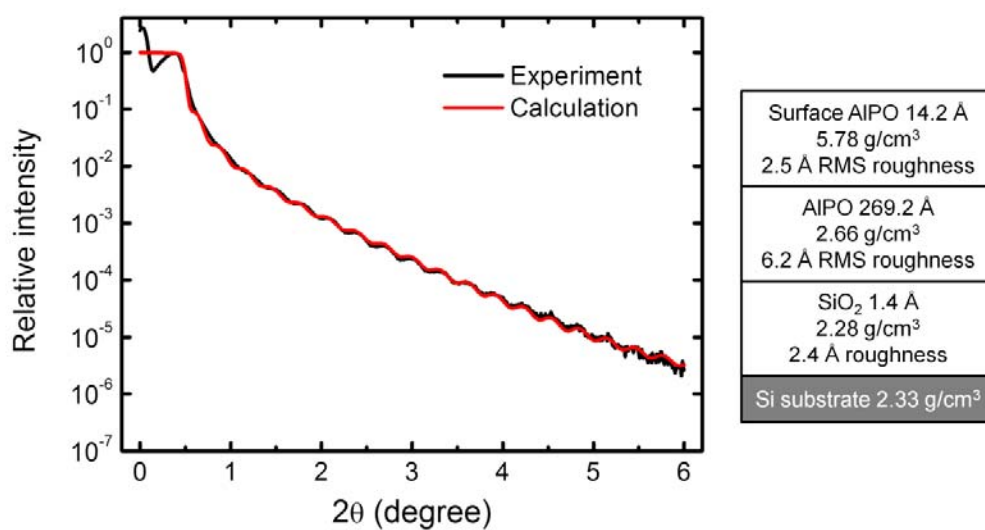


Figure D.4. The same experimental XRR spectrum in Figure D.3 with a different calculated spectrum. Here, the calculated spectrum was generated by assuming a thin but highly dense AlPO surface layer. By adding the surface “crust”, the over fitting improves significantly from Figure D.3.